BRNO UNIVERSITY OF TECHNOLOGY

VYSOKÉ UČENÍ TECHNICKÉ V BRNĚ

CENTRAL EUROPEAN INSTITUTE OF TECHNOLOGY BUT

STŘEDOEVROPSKÝ TECHNOLOGICKÝ INSTITUT VUT

FATIGUE RESISTANCE AND MECHANISMS OF THE FATIGUE DAMAGE IN MATERIALS FOR HIGH TEMPERATURES

ÚNAVOVÁ ODOLNOST A MECHANIZMY ÚNAVOVÉHO POŠKOZENÍ V MATERIÁLECH PRO VYSOKÉ TEPLOTY

DOCTORAL THESIS
DIZERTAČNÍ PRÁCE

AUTHOR — **Mgr. Roman Petráš**
AUTOR PRÁCE

SUPERVISOR — **prof. RNDr. Jaroslav Polák, DrSc.**
ŠKOLITEL

CO-SUPERVISOR — **Ing. Ivo Kuběna, Ph.D.**
ŠKOLITEL SPECIALISTA

BRNO 2020

Abstract:

Superaustenitic stainless 22Cr25NiWCoCu steel designed for high temperature applications in power generation industry was investigated in terms of low cycle fatigue at room and elevated temperature. Individual specimens were subjected to different loading procedures in order to study the material response along with the mechanism of fatigue damage. Cyclic hardening/softening curves, Coffin-Manson and cyclic stress-strain curves were evaluated. Life-time behavior for various types of loading procedures was discussed with respect to the effective damage mechanisms developed under specific loading conditions.

Standard isothermal low cycle fatigue tests at room and elevated temperature were conducted. Hysteresis loops recorded during cycling were analyzed by means of generalized statistical theory of hysteresis loop. The probability density distribution function of the internal critical stresses and its evolution during cycling straining was derived for different strain amplitudes. Evolution of the surface relief along with the internal dislocation arrangement for both temperatures was assessed in relation to the development of the probability density function of internal critical stresses. Surface relief evolution using SEM equipped with FIB revealed the early fatigue crack formation. Cyclic loading at room temperature resulted in the localization of the cyclic plastic strain into persistent slip bands and formation of surface persistent slip marking consisting of extrusions and intrusions. Deepening of an intrusion leads to the initiation of the fatigue crack from the tip of the deepest intrusion. Distinctive mechanism of the early crack formation was found in test at elevated temperature where the effect of environment is crucial. Rapid oxidation of the grain boundaries and subsequent cracking of the oxidized grain boundaries represent effective mechanisms of the nucleation of I-stage fatigue crack. Additional 10 minute tensile dwells implemented into the loading cycle led to the internal damage evolution. To reveal internal damage the longitudinal cross-sections parallel to the stress axis of the tested specimen were produced. The crack paths and their relation to the grain and twin boundaries were studied using electron back-scattered diffraction (EBSD) technique. The influence of dwells introduced in the loading cycle on fatigue life is assessed in relation to the evolution of the surface relief and internal damage.

Specimens were also exposed to more complex loading procedures where the load along with the temperature varies with time simultaneously. In-phase and out-of-phase type thermomechanical fatigue (TMF) tests with or without dwells were conducted. Rapid cyclic hardening was observed in all tests regardless of the strain amplitude applied while tendency to saturation was found primarily in out-of-phase loading with/without dwells. Investigation of the surface relief by means of SEM along with FIB cutting revealed the preferential oxidization and cracking of the grain boundaries perpendicular to the loading axis. Dwells implemented in maximum tension resulted in the enlargement of the plastic strain amplitude and to the additional creep damage in the form of internal cracks. Intergranular crack propagation was observed for in-phase cycling with/without dwells. Damage evolution in out-of-phase cycling was found to be principally similar for straining with and without dwell. Multiple cracks nucleated in the uniform oxide layer perpendicularly to the stress axis within the grains are the hallmark for out-of-phase

straining. Cracking of the uniform oxide layer and localized repeated oxidation and oxide cracking resulted in transgranular crack growth.

Key words: low cycle fatigue, fatigue resistance, statistical theory, hysteresis loop, damage mechanism, persistent slip bands, fatigue life, cyclic stress-strain response, creep-fatigue interaction, cavity formation, internal damage, thermomechanical fatigue, scanning electron microscopy (SEM) , focused ion beam (FIB), energy dispersive spectroscopy (EDS), electron backscatter diffraction (EBSD)

Abstrakt:

Superaustenitická korozivzdorná ocel typu 22Cr25NiWCoCu určená pro vysokoteplotní aplikace v energetickém průmyslu byla studována za podmínek nízkocyklové únavy při pokojové a zvýšené teplotě. Jednotlivé vzorky byly podrobeny různým zátěžným procedurám, což umožnilo studium materiálové odezvy spolu s mechanismem poškození. Křivky cyklického zpevnění/změkčení, cyklického napětí a Coffin-Mansonovy křivky byly vyhodnoceny. Únavová životnost materiálu byla diskutována s ohledem na uplatňované mechanismy poškození, které se vyvinuly za specifických zátěžných podmínek.

Standardní izotermální únavové experimenty byly provedeny při pokojové a zvýšené teplotě. Hysterezní smyčky zaznamenané během cyklického zatěžování byly analyzovány pomocí zobecněné statistické teorie hysterezní smyčky. Pro různé amplitudy napětí byla určena jak distribuce hustoty pravděpodobnosti interních kritických napětí (dále PDF), tak rovněž zjištěn její vývoj během cyklického namáhání. Zjištěné průběhy PDF byly korelovány s vývojem povrchového reliéfu a vnitřního dislokačního uspořádání zdokumentované pro obě teploty pomocí rastrovací elektronové mikroskopie (SEM) vybavené technikou fokusovaného iontového svazku (FIB), která umožnila rovněž efektivní studium nukleace povrchových únavových trhlin. Při cyklickém zatížení při pokojové teplotě byla pozorována lokalizace cyklické plastické deformace do perzistentních skluzových pásů (PSP). V místech, kde tyto PSP vystupují na povrch materiálu byly pozorovány perzistentní skluzové stopy (PSS) tvořené extruzemi a intruzemi. Postupné prohlubování intruzí, zejména na čele nejhlubší intruze, vede k iniciaci únavové trhliny. Odlišný mechanismus tvorby trhlin byl zjištěn při únavové zkoušce při zvýšené teplotě, kde zásadní roli hrál vliv prostředí. Rychlá oxidace hranic zrn a jejich následné popraskání představuje dominantní mechanismus v I. stádiu nukleace trhlin. Aplikace desetiminutové prodlevy v tahové části zátěžného cyklu vedlo k vývoji vnitřního (kavitačního) poškozování. Mechanismy vnitřního poškozování byly studovány na podélných řezech rovnoběžných s napěťovou osou zkušebních vzorků. Trhliny a jejich vztah k hranicím zrn a dvojčat byly studovány pomocí difrakce zpětně odražených elektronů (EBSD). Vliv prodlevy na únavovou životnost byl korelován s vývojem povrchového reliéfu a vnitřního poškození.

Vzorky z uvedené oceli byly rovněž podrobeny zkouškám termomechanické únavy (TMF), při nichž se v čase mění jak zátěžná síla tak i teplota. Termomechanické únavové zkoušky v režimu soufázném (in-phase) a protifázném (out-of-phase) byly provedeny jak s prodlevou, tak i bez ní. Ve všech případech bylo pozorováno rychlé cyklické zpevnění bez ohledu na použitou amplitudu deformace, u vzorků testovaných v out-of-phase režimu

byla zjištěna tendence k saturaci. Zkoumáním povrchového reliéfu za pomocí technik SEM a FIB byla odhalena přednostní oxidace hranic zrn a následné praskání těchto hranic kolmo k ose zatížení. Prodlevy v cyklech při maximálním napětí vedly ke zvýšení amplitudy plastické deformace a následně ke creepovému poškození ve formě vnitřních kavit a trhlin. Interkrystalické šíření trhlin bylo pozorováno na vzorcích testovaných v režimu in-phase. Vývoj poškození v režimu out-of-phase nebyl principiálně ovlivněn zařazením prodlevy do zátěžného cyklu. Charakteristickým znakem namáhání v režimu out-of-phase je nukleace několika trhlin v homogenní oxidické vrstvě jdoucích napříč zrny kolmo k ose zatěžování. Praskání oxidické vrstvy, opakovaná lokalizovaná oxidace a následné praskání oxidů vedlo k transkrystalickému růstu trhlin.

Klíčová slova: nízkocyklová únava, únavová odolnost, hysterezní smyčka, mechanismus poškození, perzistentní skluzové pásy, únavová životnost, cyklická napěťově deformační odezva, interakce únavy a creepu, tvorba kavit, vnitřní poškození, termomechanická únava (TMF), rastrovací elektronová mikroskopie (REM), fokusovaný iontový svazek (FIB), energiově disperzní spektroskopie (EDS), difrakce zpětně odražených elektronů (EBSD)

Bibliography of the Thesis

PETRÁŠ, R. *Fatigue Resistance and Mechanisms of the Fatigue Damage in Materials for High Temperatures*. Brno: Brno University of Technology, Central European Institute of Technology BUT, 2020. 146 p.

Supervisor: prof. RNDr. Jaroslav Polák, DrSc., dr. h. c.

Declaration

I hereby declare that my dissertation thesis ‘’Fatigue Resistance and Mechanisms of the Fatigue Damage in Materials for High Temperatures’’ was written by myself under supervision of prof. RNDr. Jaroslav Polák, DrSc., dr. h. c.. All sources of information are listed in the Reference section of the thesis.

Brno, 24.02.2020: ……

signature

Acknowledgement

First and foremost, I would like to express a huge gratitude for perpetual support, patience, but mostly for professional guidance to my supervisor, Prof. RNDr. Jaroslav Polák, DrSc. dr.h.c.. I am very thankful for his help and encouragement concerning the internships I participated in. Not to mention the extensive, inspiring discussions on distinctive research issues throughout my doctoral studies. Further thanks belong to my co-supervisor Ing. Ivo Kuběna, Ph.D. for uncovering the secrets of the scanning electron microscopy along with related techniques, to me.

Special thanks go to prof. Mgr. Tomáš Kruml, CSc., the first person I met in the Institute when starting a part-time job, for interesting discussions and chatting not only in terms of research. Further thanks belong to my colleagues from Institute for their help, practical advices and chatting on what-ever-you-think-of. Huge thanks go to Viktor Škorík for collaboration on thermomechanical fatigue research and help with my the first ever paper published as a first author. I would like to thank our technicians, especially Jíři Tobiáš, who has become my travel-mate.

I am very grateful to CEITEC for opportunity to participate in internships in Leoben and Siegen. My huge thanks belong to Univ. Prof. Dr. Reinhard Pippan and Prof. Dr.-Ing. Hans-Juergen Christ for enriching experience in their research groups. Special thanks to Dr.-Ing. Arne Ohrndorf and Sven Brück for assistance with the experiments.

The greatest thanks belong to my closest relatives; my beloved girlfriend Andrea, for infinite support, understanding and … well, long story short for everything; my parents Jarmila and Štefan, for love, support and patience; last but not least my brother Richard, for support, discussions on various stuff and some issues with English.

Thank you all.

Table of Contents

1. Introduction

Electrical energy is currently the most widely used type of energy around the world. Similarly to the other kinds of energy it has multiple advantages and disadvantages, but the benefits usually prevail. Coal has a dominant role in worldwide electricity production. Unfortunately, the world's electrical coal-fired power generation is one of the main sources of carbon dioxide emission. Coal power plants produce approximately 10 billion tons of CO_2 per year. Increase in the efficiency of the conventional coal-fired power plants by one percent results in a 2-3% reduction in CO_2 emissions [1]. The efficiency progress of power generation brings many challenging issues. This improvement can be achieved by increasing the maximum steam temperature and the steam pressure.

Design and construction of novel, more efficient installations require the usage of materials resisting severe loading and environmental conditions. Thermal and mechanical stresses in components during service produce variable strains and result in initiation and propagation of fatigue cracks. These cracks are difficult to detect but can lead to interruption of the installations or even to catastrophic failure of the energy producing systems. Low cycle fatigue and creep strength under severe environmental conditions have to be considered to determine the rate of damage in materials working at elevated temperatures.

The main goal of the component development is to ensure their reliable and safe operation. The assessment of damage and the risk associated with failure has become very important in recent years. In order to meet such an assessment, it is necessary to identify the mechanisms of degradation and the rate of accumulation of damage during the service. The principal deterioration mechanisms of material exposed to elevated temperatures are creep damage, microstructural degradation, high temperature fatigue, creep-fatigue interaction, embrittlement, carburization, hydrogen damage, graphitization, thermal shock, erosion, liquid metal embrittlement and high temperature corrosion [2].

Austenitic stainless-steel grade UNS S31035, Sandvik Sanicro 25, has been developed for the next generation components used in advanced-ultra super critical (A-USC) power plants systems. Material shows very good resistance to steam oxidation; high temperature corrosion and exhibits high creep rupture strength, higher than the other austenitic stainless steels available today. This makes the material an interesting alternative for super-heaters and reheaters in future high-efficient coal fired boilers [3, 4]. It is still in development stage when its properties are measured and verified.

The dissertation thesis is devoted to the study of the cyclic plastic response, evaluation of the cyclic hardening/softening curves, fatigue live curves and to characterization of the mechanisms of the fatigue damage in material Sanicro 25 steel designed for high temperature applications subjected to different loading conditions.

2. Current state of knowledge

2.1 Austenitic stainless steels

Austenitic stainless steels (ASSTs) are generally acknowledged as the most common type of stainless steels. Since the ASSTs are usually easily formable and weldable, they have become a prior material in wide range of daily use regarding large spectra of applications from cryogenic temperatures to the temperatures of furnaces and even jet engines [5].

ASST has a face-centred cubic (FCC) crystallographic structure. The alloy typically contains 16-26 wt.% Cr, 8-25 wt.% Ni and 0-6 wt.% Mo, and is fully austenitic from well below room temperature to the melting temperature [6, 7]. Due to the crystallographic structure, ASSTs are non-ferromagnetic, have higher heat capacity and thermal expansion coefficient, but lower thermal conductivity when compared to other stainless steel grades [6]. The material typically exhibits excellent ductility, formability and toughness along with great creep resistance [8].

2.2 Composition of Austenitic stainless steels (main alloying elements)

Fe-Cr-Ni based ASSTs are regularly used for various applications at elevated temperatures. The structure and mechanical properties of the material chosen have to be provided accordingly. In order to produce material requested the alloying elements need to be involved. Main alloying elements will be briefly introduced.

The corrosion resistance of stainless steels rapidly increases when alloyed by the chromium. Once the amount of chromium is 12 wt.% or higher, the protective oxide layer develops on the material surface. The layer is self-healing if it gets damaged, due to the rapid reaction between chromium and oxygen [6]. The oxide layer prevents further oxidation of the matrix. Since chromium is a ferrite stabilizer, it is balanced by austenite stabilizing elements (e.g. Ni, Mn, …) to keep the FCC lattice sustainable.

Nickel is added to stabilize the austenite structure and moreover it highly increases the general resistance to corrosive environments.

Manganese stabilizes austenite and increases the solubility of nitrogen in austenite. This element has been frequently used in ASSTs as an alternative for nickel mainly due to economic reasons [8].

Molybdenum facilitates the precipitation of the carbides and thus improves the local and the general corrosion resistance along with the creep properties. Since molybdenum is a ferrite stabiliser, ASST structure has to be balanced with austenite stabilisers [8].

Titanium and niobium are known as stabilizing elements. The formation of the Ti-/Nb-carbides brings two essential benefits. Since titanium and niobium are prone to form carbides more willingly than chromium, Ti-/Nb- carbides are formed preferentially in comparison with

chromium carbides. The localized reduction of chromium is thus prevented and results in higher intergranular corrosion resistance. Moreover, the fine intergranular carbides may contribute to creep strength of austenitic steels [8].

Carbon is an austenite stabilizer manifesting by solid solution strengthening in case of non-stabilized ASSTs grades and causes precipitation strengthening in presence of Nb, T, or V in the structure [8].

Nitrogen addition stabilizes the austenitic phase and strengthens the material through solid solution hardening leading to the enhanced creep life of austenitic steels [6]. It is carbon-like element in terms of stabilizing stainless steel by formation of precipitates such as titanium or niobium nitrides. Nitrogen also facilitates the chromium diffusion but impedes the $M_{23}C_6$ nucleation as a consequence of its low solubility in this carbide [8].

Alloying elements have decisive influence on the material microstructure as well as on material properties. Schaeffler-DeLong diagram is the chemical composition related model for the material structure prediction. It has been widely used for heat treatment procedures, even though it was originally developed for welding.

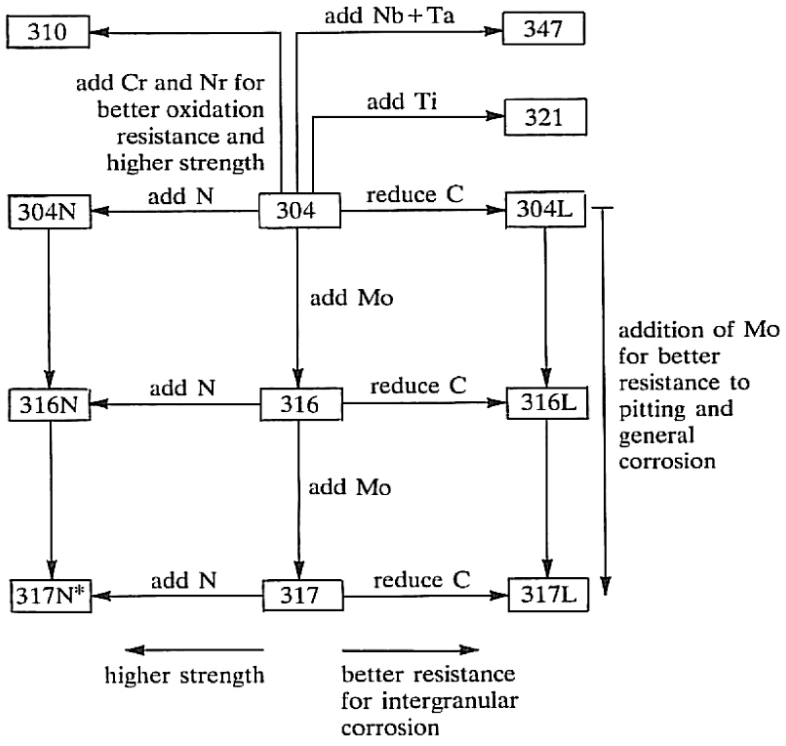

Fig. 1. The family of ASSTs; compositional modifications of 18Cr-8Ni ASST [10].

The elements introduced to the material structure are usually classified as the ferrite-stabilizing elements such as chromium, molybdenum, silicon and niobium, while the austenite-stabilizing elements are nickel, manganese, carbon and nitrogen, for instance.

Chromium and nickel equivalents are calculated in accord to eq. (1) and (2) taking into account the effect of stabilizing elements on the resulting microstructure [8, 9]:

$$Ni_{eq} = [Ni] + [Co] + 0.5[Mn] + 30[C] + 0.3[Cu] + 25[N] \ (wt\%) \quad (1)$$

$$Cr_{eq} = [Cr] + 2.0[Si] + 1.5[Mo] + 5.5[Al] + 1.75[Nb] + 1.5[Ti] + 0.75[W] \ (wt\%) \quad (2)$$

The prediction of the microstructure is not always unequivocal and various modifications have to be taken in account when considering precipitation reactions [8].

The effect of some compositional modifications of 18Cr-8Ni ASST (304 stainless steel in the figure) improving certain properties is shown in Fig.1. The wide spectrum of the alloys introduced in many industrial applications can be recognized [10].

2.3 Precipitates in austenitic stainless steels

Due to excellent mechanical properties and corrosion resistance at elevated temperatures, ASSTs are widely used for the design of components operating at elevated temperatures such as power plants and aero engines. The addition of alloying elements may result in precipitation of secondary phases such as various types of carbides, nitrides and intermetallic phases depending on the chemical composition of the material. Whether their occurrence is desirable or not is a question of the application proposed. Let's consider the most common precipitates in ASSTs.

2.3.1 Carbides and nitrides

$M_{23}C_6$

$M_{23}C_6$ is carbide with FCC structure of lattice parameter varying between 1.057 and 1.068 nm (three times that of the austenite) [8]. It often contains Cr as the main metallic element (M), although Ni, Mo and Fe have been found to partially substitute Cr. The phase frequently precipitates on the nucleation sites such as grain boundaries, incoherent and coherent twin boundaries and intragranular sites [8, 11, 12, 13]. In terms of the corrosion resistance $M_{23}C_6$ is associated with the precipitation on grain boundaries resulting in intergranular corrosion due to depletion of chromium content in the matrix locally below 12 % required for stainless steel to prevent from oxidation and corrosion. On the contrary, precipitation of this phase may have beneficial effect for the creep rupture strength, since the grain boundary sliding and surface cracking is suppressed. The density of $M_{23}C_6$ along the grain boundaries increases when introducing boron in the matrix [8].

MX precipitates

MX commonly precipitates on dislocations within the matrix, stacking faults, and on twin as well as grain boundaries. The MX has a NaCl type FCC structure. The formation of a phase depends on strong nitride/carbide formers involving V, Zr, Ta, Ti, Nb added to the alloy [7]. The main purpose of adding these elements is to stabilize the alloy against intergranular

corrosion and to provide good creep resistance [8]. Currently, nitrogen-rich Nb-based precipitates are of great interest for industrial applications. Nucleation of particles have been observed in the advanced commercial austenitic stainless steels such as HR3C and Sanicro 25. Formation of incoherent NbC nanoparticles has been studied by Heczko et al. [14]. The study by means of scanning transmission electron microscopy (STEM) brought a deeper insight into atomic composition of the nanoclusters. Strain-induced incoherent NbC nanoparticles precipitate mostly on the dislocations and stacking faults and serve as an effective obstacle for dislocation movement at 700 °C resulting in extraordinary cyclic hardening of the material during isothermal cyclic loading.

Z phase

The Z phase is a complex carbonitride frequently observed in Nb stabilised austenitic stainless steels with high nitrogen content. The crystal structure of the Z phase is generally accepted since it was determined by Jack and Jack in 1972 [15]. The particles for the stoichiometry CrNbN have distorted body-centred tetragonal structure consisting of metal atoms with double layer of alternating atoms (unit cell with space group P4/nmm). The lattice parameters are a = 0.304 nm and c = 0.739 nm. It typically forms at high temperature close to grain and twin boundaries and within the matrix having either cuboidal or rod-like morphology [8]. Since the carbonitride usually precipitates as a fine dispersion of particles, it represents an interesting phase in applications where good creep properties are demanded [8, 16, 17].

2.3.2 Intermetallic phases

σ phase

σ phase is an intermetallic phase formed in the Fe-Cr system. Its composition is very variable depending on the alloying elements introduced. Generally, it has tetragonal structure (unit cell space group $P4_2/mnm$ with a = 0.880 nm and c = 0.454 nm (FeCr) [8]. σ phase formation is promoted when alloying by elements such as Cr, Nb, Ti and Mo. The precipitation of the phase reduces ductility and toughness of the steel along with the corrosion resistance. The negative influence of the corrosion resistance is attributed to depletion of chromium and molybdenum from the matrix when forming σ phase [9, 18]. There are two typical nucleation sites; precipitation on the grain boundaries and formation of the phase within the grains, respectively. The dimensions of the precipitates may have significant effect on the creep resistance. While the large precipitates cause embrittlement of the grain boundaries, small and evenly distributed particles may increase the creep resistance by retardation of the grain boundary sliding [19, 20, 21].

Laves phase

Laves phase has been observed in several grades of austenitic stainless steels. It has a hexagonal structure (unit space group $P6_3/mmc$) with a = 0.473 nm and c = 0.772 nm. The phase commonly precipitates within the grains, but it has been found also at the grain boundaries [8, 22]. The effect of the Laves phase on creep properties is still widely discussed.

The precipitation of the Laves phase in austenitic stainless steel is promoted by addition of W. Laves phase increases the strength of steel by solid solution hardening [23].

2.4 Austenitic stainless steels for elevated temperatures (utilized for boilers)

ASSTs applied to the high temperature service have to sustain demanding loading and environmental conditions. These grades exhibit an austenitic microstructure that ensures a high resistance to fire-side corrosion and steam-side oxidation and provides high creep rupture strength. The characteristics of the conventional and advanced austenitic stainless steels makes them highly suitable for design of superheat and reheat tubing working at steam temperatures up to 630 °C and 680 °C. However, the materials are not suitable for water-wall construction due to susceptibility to stress corrosion cracking in wetted parts [10].

Concerning the nuclear reactor technology, the stainless steels are widely used in the primary circuits of advanced cooled reactors. In the primary circuit, the control rod components, thermal insulation and hot box component are typically assembled from AISI types 304, 321 and 316 stainless steels [10]. The upper sections of the boilers are from type 316 stainless steel.

Material	Average composition	Application		
		SC	USC	A-USC
Austenitic stainless steels				
304H	18Cr-8Ni	SH/RH		
347H	18Cr-10Ni-Nb	SH/RH		
Advanced austenitic stainless steels				
347HFG	18Cr-10Ni-Nb (b)	SH/RH	SH/RH	
Super 304H	18Cr-10Ni-Nb-Cu (b)	SH/RH	SH/RH	
NF709	20Cr-25Ni-Mo-Nb-B		SH/RH	SH/RH
HR3C	25Cr-20Ni-Nb		SH/RH	SH/RH

Tab. 1. SH/RH = superheat and reheat tubing.
(b) Fine grained form of 347H obtained by thermo-mechanical processing [24].

There is an effort to construct power plants with main steam temperatures up to 760 °C with efficiency as high as 50%. The technology is divided into three main categories referring to high temperature materials utilized [24]:

1. Conventional supercritical (SC) boilers are made from standard ferritic and austenitic stainless steels and operate below 590 °C (1100 °F). The main steam pressure is around 250 bar (3620 psia, 25 MPa) with a reheat pressure around 45 bar (650 psia, 4.5 MPa).

2. Ultra-supercritical (USC) boilers are made from creep-strength enhanced ferritic and advanced austenitic stainless steels and operate in the temperature range 590–620 °C (1100–

1150 °F). The main steam pressure is around 250 bar (3620 psia, 25 MPa) with a reheat pressure around 50 bar (730 psia, 5 MPa).

3. Advanced ultra-supercritical (A-USC) boilers will be made from nickel-based alloys and operate in the range 700–760 °C (1290–1400 °F). The main steam pressure will be around 345 bar (5000 psia, 34.5 MPa) with a reheat pressure around 76 bar (1100 psia, 7.6 MPa).

Materials for different categories of supercritical boiler are shown in table Tab. 1.

Sanicro 25 steel grade belongs to the group of advanced austenitic stainless steels developed for the next generation components used in A-USC power plants systems.

2.5 Low cycle fatigue

2.5.1 General features of the fatigue process

The term fatigue is widely used when referring to a gradual process of material degradation exposed to cyclic straining under different loading conditions. These circumstances lead to initiation of the fatigue cracks, their subsequent growth until the fracture of the component follows. Low cycle fatigue fractures have been classified as the origin of failures in extensive number of equipment or components such as energy production equipment, in piping, pressure vessels, steam turbines as well as in transport machines and carriers. Initiation of the fatigue cracks after low number of working cycles is associated with the start-up or shut-down operations or the achievement of the service conditions [25, 26]. The basic and decisive factor in the evolution of cumulative damage taking place during cyclic straining is the cyclic plastic deformation. The localization of the cyclic plastic deformation during cyclic loading is the dominant condition for initiation of the fatigue cracks. Furthermore, the fatigue crack propagation is highly influenced by the level and rate of the cyclic plastic deformation in the plastic zone ahead of the crack tip. This holds true particularly when it comes to cyclic straining at room temperature, while during loading at elevated temperature the environmental processes strongly affect the fatigue crack initiation and propagation [25, 26]. The distinctive damage mechanisms under various loading conditions will be covered later. A detailed insight in the laws governing the fatigue processes is crucial factor for improvement of the fatigue resistance and to assess the fatigue life based on the quantitative model of cumulative damage.

Bearing in mind the irreversible changes due to cyclic plastic deformation, the fatigue process is divided into three slightly overlapping stages:

- The internal interaction between microstructural defects such as dislocations in the whole volume of the material reflects the material response on particular parameter of cyclic loading like stress amplitude, strain amplitude, mean stress, temperature, etc. The change of the mechanical properties is clearly visible when plotting stress amplitude vs.

number of cycles, for instance. The behaviour of fatigue hardening/softening depends mainly on the initial state of the material.

- The localization of the cyclic plastic deformation results in formation of the nucleation sites leading to the initiation of the fatigue cracks.

- The perpetual growth of the fatigue cracks is governed by the cyclic plastic deformation localized in the plastic zone ahead of the crack tip [25].

The stages of the fatigue process are depicted schematically in Fig.2.

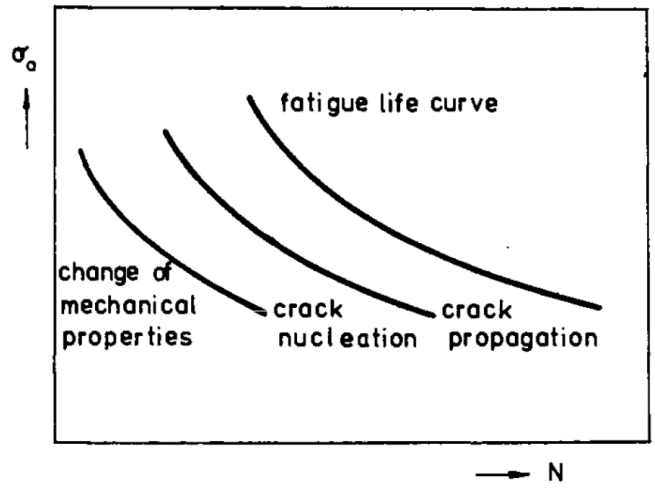

Fig. 2. Stages of the fatigue process [26].

The first two curves denote the end of the hardening/softening process and the end of the stage of fatigue crack nucleation, respectively. It needs to be mentioned that there is no unequivocal defined border between these particular stages. Definition of the border is only the matter of convention, since the initiation of the fatigue crack takes place even during the hardening/softening stage. The last curve represents the fatigue life curve that marks the end of the crack propagation stage, in other words, the end of the whole fatigue process. From the engineering point of view, the fatigue process can be divided into two fundamental sections namely; initiation of the fatigue crack and growth of the fatigue crack until critical length is reached. The value of the critical crack length depends on the material; its crystalline structure, scale of the grain, distribution of the inclusions etc. [25, 26].

2.5.2 Cyclic hardening/softening process

The modification in the material microstructure and related changes of the material properties take place during cyclic loading. Generally, the gradual evolution of a quantity observed (stress amplitude, stress level, plastic strain amplitude etc.) lead to saturation regime. The strongest changes are observed at the onset of a cyclic loading. The hardening/softening process are described in terms of the stress-strain response of the cyclically loaded material [25]. Fig. 3 schematically depicts the hysteresis loop representing

the relation between stress σ and strain ε within one cycle. Stress amplitude is denoted by σ_a , strain amplitude by ε_a , and plastic and elastic strain amplitudes by ε_{ap} and ε_{ae} , respectively.

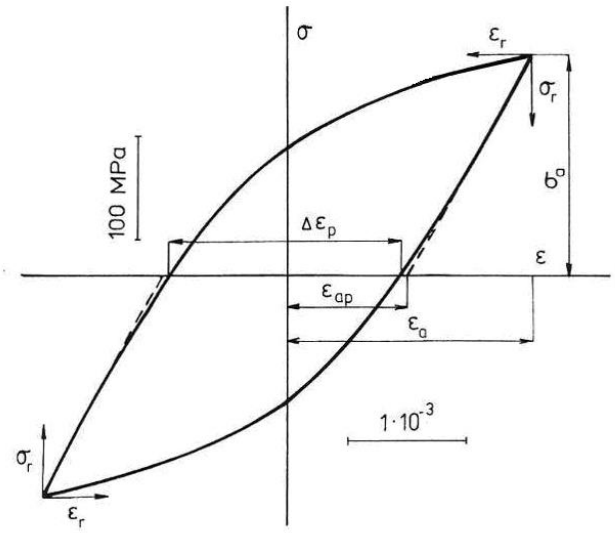

Fig. 3. Scheme of the saturated hysteresis loop [25].

The typical low cycle fatigue test is either stress-, or, strain-, or plastic strain-controlled driven at constant strain rate. Fig. 4 shows the stress-strain relation for constant stress amplitude loading, for constant total strain amplitude loading, and for constant plastic strain amplitude loading. The shape as well as the area of the hysteresis loop undergo changes when subjected to cyclic loading.

If the controlled quantity is stress amplitude, the process of fatigue hardening in a σ_a – controlled test manifests by a decrease of both total strain and plastic strain amplitude. In the case of constant total strain amplitude loading, cyclic hardening is presented as a gradual increase of the stress amplitude and decrease of the plastic strain amplitude. Cyclic hardening in a ε_{ap} - controlled test is characterized by an increase of both stress amplitude and total strain amplitude [25, 26].

Three basic scenarios of material response may occur in relation to prior material treatment. Cyclic hardening typically dominates when annealed materials are subjected to cyclic loading. However, there are plenty of cases of cyclic softening especially when the material was hardened either by solute atoms or precipitates, or by cold working. The first stage of the fatigue process frequently exhibits cyclic hardening followed by cyclic softening, or vice versa [26]. The saturation is presented by the hysteresis loop showing no further changes during cyclic straining. It should be noted that some materials do not reach the saturation during cyclic loading. The different saturated hysteresis loops for various strain amplitudes (or stress amplitudes if chosen) plotted in coordinates stress versus plastic strain are shown in Fig. 5a. The curve connecting the tips of these saturated hysteresis loops represents the relation between the saturated stress amplitude and the saturated strain amplitude. In the case shown in Fig. 5a the plastic strain amplitude is considered. The curve is known as the cyclic stress-

strain curve and determines an essentials characteristic of fatigue loading since it describes the stress-strain relation of the loaded material for a fundamental part of the fatigue life [26].

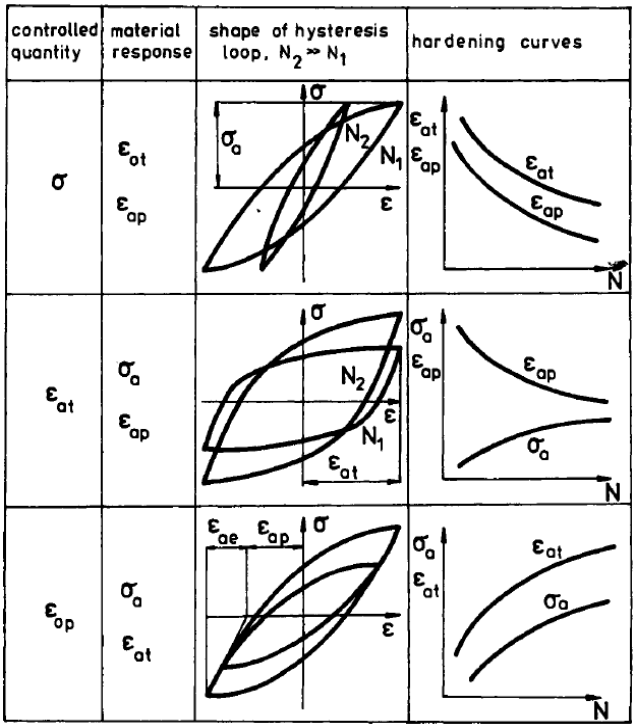

Fig. 4. Manifestation of cyclic hardening in different regimes of cycling [26].

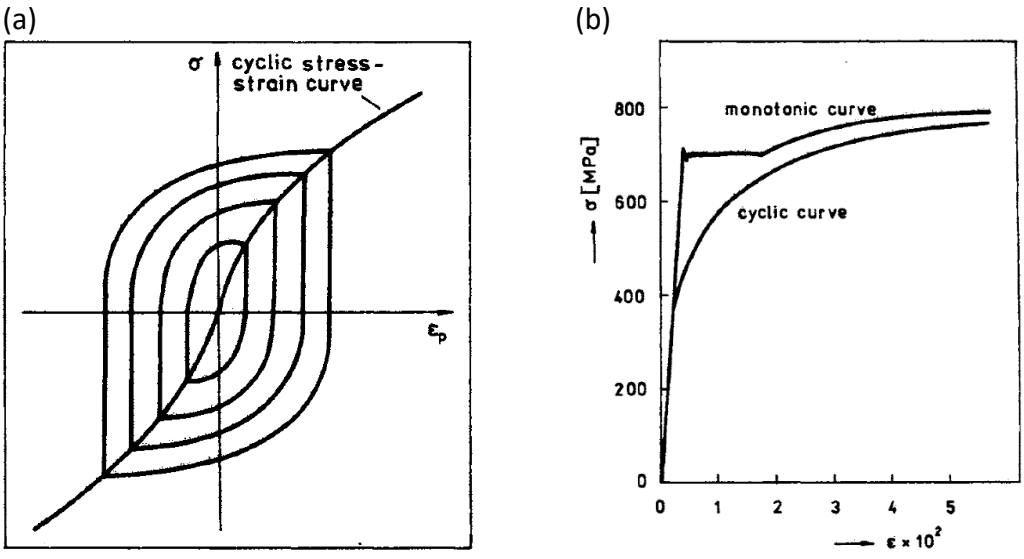

Fig. 5. (a) Definition of cyclic stress-strain curve. (b) Monotonic and cyclic stress-strain curves of alloyed carbon steel [26].

The assessment of whether the cyclic hardening/softening takes place might be estimated when comparing the cyclic stress-strain curve with the monotonic stress-strain curve (i.e. with the tensile diagram). Fig. 5b displays the case of the material cyclic softening since the cyclic

curve lies well below the monotonic curve. In the case of cyclic hardening, the reversed behaviour is observed [26].

2.5.3 Fatigue life curves

The low cycle fatigue resistance is typically studied on the smooth specimens having circular cross-section subjected to symmetric strain-controlled loading (stress or displacement control can be chosen alternatively) with constant strain rate and total strain amplitude. The strain is measured with the extensometer attached to the specimen gauge length. The stress-strain relation is recorded during the cyclic loading and hysteresis loops can be depicted. Strain rate is crucial parameter in elasto-plastic cyclic loading and is commonly held constant in strain-controlled procedure. Constant train rate is accomplished when introducing triangular wave shape where strain rate is positive in the tension half-cycle, negative in the compression half-cycle and gets abruptly changed when reaching extremes [26, 27].

The fatigue life of various of materials can be described by the Coffin-Manson law [28, 29], where the fatigue life depends on the plastic strain amplitude. The relation is determined by a power-law

$$\varepsilon_{ap} = \varepsilon'_f \left(2N_f\right)^c, \tag{3}$$

where ε'_f denotes the fatigue ductility coefficient and *c* the fatigue ductility exponent. Both parameters can be evaluated from the experimental data using regression analysis. The fatigue ductility coefficient ε'_f represents the extrapolated plastic strain in the first half-cycle and could therefore be correlated with the tensile ductility ε_f evaluated from the tensile test [26].

Derived Wöhler curve represents the plot of the saturated stress amplitude versus number of half-cycles to fracture. The data points obtained from the experiment are fitted with the Basquin relation

$$\sigma_a = \sigma'_f \left(2N_f\right)^b. \tag{4}$$

Parameter σ'_f is the fatigue strength coefficient and *b* the fatigue strength exponent, respectively. The fatigue strength coefficient is the extrapolated stress amplitude to the first half-cycle and can be correlated with the true fracture stress σ_f [26].

When adopting eq. (3) and (4) the fatigue life curve in constant total strain amplitude loading can be written as the sum of plastic and elastic strain amplitudes

$$\varepsilon_a = \varepsilon'_f \left(2N_f\right)^c + \frac{\sigma'_f}{E}\left(2N_f\right)^b. \tag{5}$$

Provided the parameters ε'_f, *c*, σ'_f, *b* and Young's modulus *E* are found, it is possible to calculate the strain amplitude ε_a resulting in the fatigue life N_f. Vice versa, from the strain amplitude ε_a it is possible to calculate the number of cycles to fracture N_f. Fig. 6 depicts schematically the number of half-cycles to fracture plotted versus the total strain amplitude, elastic strain amplitude, and plastic strain amplitude in saturation [27].

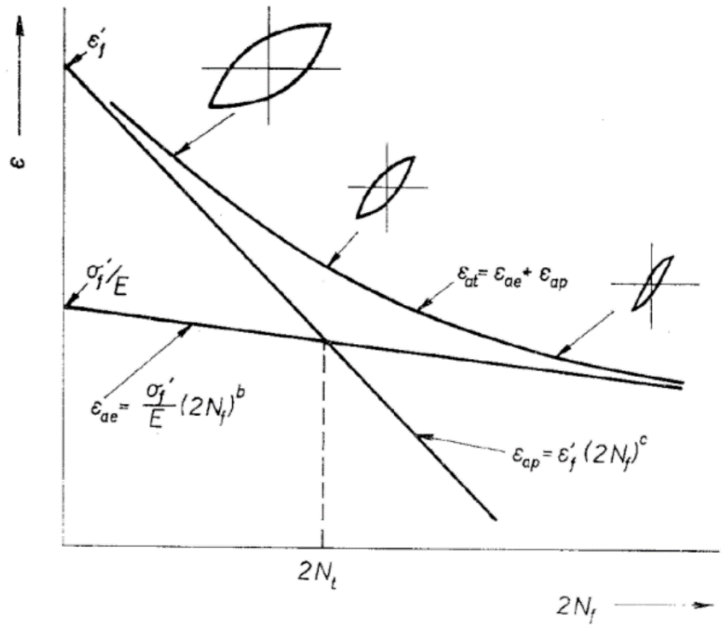

Fig. 6. Total strain amplitude, plastic strain amplitude and elastic strain amplitude versus number of (half-cycles) reversals to fracture in low-carbon steel [27].

2.5.4 Analysis of the cyclic plastic response of materials based on the hysteresis loop shape

> ''When one knows how to look, one finds the spirit of a century and the physiognomy of a king even in the knocker on the door.''
>
> The Hunchback of Notre Dame, Victor Hugo (2012)

The hysteresis loop represents one of the most essential characteristics of the cyclic plastic response of a material. This stress-strain relation is of primary importance for deeper analysis of the microstructural changes driven by the cyclic plastic straining during low cycle fatigue tests. The microstructural changes result in an accumulation of the fatigue damage and nucleation of the fatigue cracks [25, 30, 31].

The cyclic plastic straining is associated with the properties of dislocations and other lattice defects along with the dislocation motion mechanisms forming distinct dislocation arrangement in crystalline structure of the material. In the recent decades numerous efforts have been focused on formation of the statistical approach for cyclic-strain response based on fundamental mechanisms of dislocation motion [25, 32, 33, 34, 35]. The inhomogeneity of

the material and the heterogeneity of the plastic strain represent the basic assumption for modelling of the material behaviour proposed by Masing [36] in 1923. The statistical approach is based on hypothesis concerning the distribution of finite number of elementary volumes having different critical yield stress arranged in parallel in cyclically loaded material. Afanasjev [37] generalized Masing's approach by extension of the number of microvolumes considered into infinity. These microvolumes with different specific critical yield stress are described and characterized by probability density function (PDF). Each volume is deformed elastically, either in tension or compression. Provided the critical yield stress is reached, the microvolume deforms plastically without hardening. The behaviour of a microvolume is similar in this regard to the behaviour of a single crystal oriented for single slip [25, 30, 31].

2.5.4.1 The internal and effective stress components

Scrutiny of the internal dislocation structures of cyclically loaded material revealed characteristic inhomogeneity in the dislocation distribution. When adopting the statistical theory, the microvolumes of various dislocation arrangement and densities are described by the distribution function of microvolumes with characteristic internal critical stresses, equivalent in tension as well as compression. The component of the internal critical stress of a particular microvolume stems from the stress field attributed to combination of the fields from all the adjacent dislocations and other lattice defects acting on a mobile dislocation in a direction opposite to the direction of straining. Provided the applied stress is higher than the internal critical stress of the particular microvolume, the mobile dislocation is subjected to an effective stress. The mobility of the dislocation can be thermally activated; therefore, the effective stress component strongly depends on a temperature along with a strain rate [25, 30, 31, 38].

2.5.4.2 Methods for evaluation of the effective stress

There are numerous experimental techniques adopted for separation of the cyclic stress into two components:

- analysis of the hysteresis loop
- stress and strain relaxation
- the stress-dip method in cyclic straining
- analysis of the change in strain rate

The interpretation of the experimental results obtained strongly depend on the analysis utilized. For the purpose of this thesis, the emphasis is placed on the analysis of the hysteresis loop. Two approaches will be mentioned, namely Kuhlmann-Wilsdorf-Laird method and Polák`s statistical approach, respectively [25, 30, 31].

2.5.4.2.1 Analysis of the hysteresis loop shape – Kuhlmann-Wilsdorf-Laird method

Kuhlmann-Wilsdorf and Laird (KWL) put forward simple method for the evaluation of the component of the effective stress, regardless of the sources of the internal stress. The KWL method is based on Cotrell's analysis of the dislocation motion during reverse straining. For the assessment of the effective stress component, let's consider following procedure. Firstly, the determination of the maximum stress in tension σ_{mT}, in compression σ_{mC} along with the stresses at which plastic strain starts in tension σ_{pT} and compression σ_{pC} as denoted in Fig.7 is required.

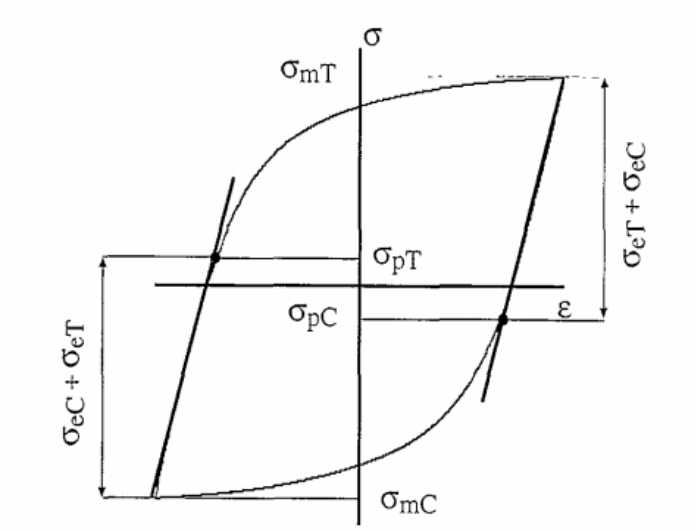

Fig. 7. Schematic diagram of the hysteresis loop showing the quantities used to evaluate the effective stress by the KWL method [30].

The stresses are defined algebraically. Nevertheless, the effective stresses in tension σ_{eT} and compression σ_{eC}, as well as the internal stresses in tension σ_{iT}, and compression σ_{iC} are defined as positive values (e.g. the actual maximum stress in compression is -σ_{eC}).

When considering the KWL approach, the sum of the effective stresses in tension and compression can be evaluated as

$$\sigma_{eT} + \sigma_{eC} = \sigma_{mT} - \sigma_{pC} = \sigma_{pT} - \sigma_{mC} . \tag{8}$$

Is it necessary to estimate the symmetry of the effective stress, since both components cannot be evaluated separately. Hence, we obtain

$$\sigma_e = \sigma_{eT} = \sigma_{eC} = \left(\sigma_{mT} - \sigma_{pC}\right)/2 = \left(\sigma_{pT} - \sigma_{mC}\right)/2 . \tag{9}$$

Finally, the internal stresses are equal to the difference between the maximum stress in tension or compression and the effective stress [30, 39].

2.5.4.2.2 Analysis of the hysteresis loop shape – Statistical approach

The probability density function determining the frequency of microvolumes having internal critical stress $f(\sigma_{ic})$ represents the most essential quantity in this approach. Since the parallel arrangement of microvolumes in a crystal is considered, the macroscopic internal stress is given by integration over all the elements. The total macroscopic stress is divided into two components, the internal stress component σ_i and the effective stress components σ_ε

$$\sigma = \sigma_\varepsilon + \sigma_i \,. \tag{10}$$

The statistical theory is based on a following basic assumptions [25, 27]:

- The whole metal consists of the microvolumes with internal critical stresses, identical in tension and compression.
- The distribution of the microvolumes in crystal is represented by normalized probability density function.
- The probability density function does not exhibit any changes during straining.
- All microvolumes undergo the same strain related to the macroscopic strain under deformation of the crystal. However, each microvolume carries a different stress.

Accordingly, the distribution of microvolumes in a crystal is identified by the probability density function $f(\sigma_{ic})$ of the internal critical stresses. In order to portray the shape of the hysteresis loop in simple form, let's consider the first and the second integral functions of the probability density function. The first and the second integral functions are

$$F(x) = \int_0^x f(x)\,dx \tag{11}$$

and

$$G(x) = \int_0^x F(x)\,dx \,. \tag{12}$$

If the crystal is plastically loaded at a finite strain rate, the component of the effective stress is considered. Considering the quasi-elastic approximation, the shape of the hysteresis loop can be expressed in relative stress σ_r and strain ε_r coordinates [25]

$$\sigma_r = \varepsilon_r E_{eff} \qquad \text{for } \varepsilon_r \le 2\sigma_{es}/E_{eff}\,, \tag{13a}$$

$$= \varepsilon_r E_{eff} - 2G\left(\varepsilon_r E_{eff}/2 - \sigma_{es}\right) \text{ for } 2\sigma_{es}/E_{eff} \le \varepsilon_r \le 2\varepsilon_a \,. \tag{13b}$$

Quantity E_{eff} denotes effective elastic modulus. Relative stress and strain for tensile and compression hysteresis-half-loops are defined as

$$\sigma_r = \sigma + \sigma_a\,,\ \varepsilon_r = \varepsilon + \varepsilon_a \text{ for tensile half-loop,} \tag{14a}$$

$$\sigma_r = \sigma_a - \sigma \,,\ \varepsilon_r = \varepsilon_a - \varepsilon \text{ for compression half-loop.} \tag{14b}$$

σ_a and ε_a represents the stress and strain amplitude, respectively.

Finally, the equation for the probability density function is obtained by double differentiation of the formula (13b)

$$f\left(\frac{\varepsilon_r E_{eff}}{2} - \sigma_{es}\right) = -\frac{2}{E_{eff}^2}\frac{\partial^2 \sigma_r}{\partial \varepsilon_r^2} \text{ for } 2\sigma_{es}/E_{eff} \le \varepsilon_r \le 2\varepsilon_a \,. \tag{15}$$

The saturated effective stress σ_{es} can be determined from the shift of the probability density function when plotting the second derivative of the hysteresis half-loop (multiplied by $-2/E_{eff}^2$) vs. fictive stress $\varepsilon_r E_{eff}/2$ as shown in Fig. 8.

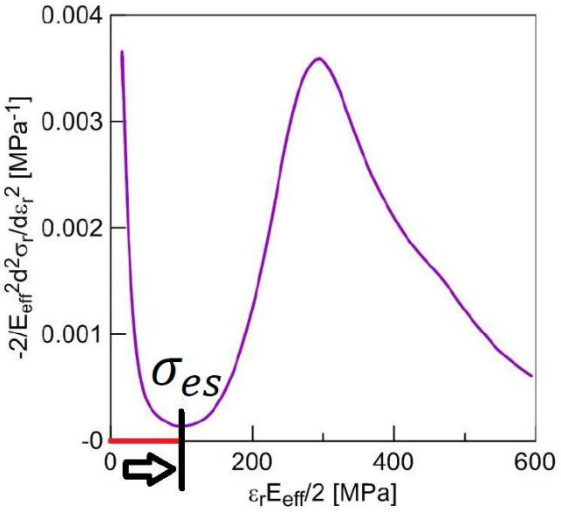

Fig. 8. The shape of the second derivative of the tensile hysteresis half-loop segment.

The first and the second derivatives of the equation (13a) lead to zero in the quasi-elastic approximation. The relaxation of the plastic strain driven by the negative effective stress carries on in all microvolumes formerly plastically deformed in compression for small fictive stresses $\varepsilon_r E_{eff} < \sigma_{es}$. Only the microvolumes with the lowest critical stress are under action of positive effective stress when $\sigma_{es} < \varepsilon_r E_{eff} < 2\sigma_{es}$, while the vast majority of the microvolumes is unloaded elastically. If $\varepsilon_r E_{eff} > 2\sigma_{es}$, the each microvolume starts yielding provided its critical stress is reached under action of the saturated effective stress [25, 30, 31].

The statistical approach has been adopted in study of the fatigue response of carbon steel, austenitic and duplex steels as well as of nickel-based superalloys [40].

2.6 Mechanisms of isothermal fatigue

Study of the cyclic deformation mechanism under low cycle fatigue conditions carried out for decades has revealed strong temperature dependence. Well known temperature-related phenomenon is mechanism of dislocation motion. While at low temperatures dislocation glide typically prevails, the dislocation climb gains its importance with increasing temperatures. The cyclic deformation behaviour of a material is related to microstructural changes and mutual interactions among dislocations and microstructure. This gives rise to phenomenon such as deformation induced transformation, deformation induced precipitation, mechanical twining and coarsening. The metallic materials frequently exhibit a strong interaction of moving dislocations with the point defects known as a dynamic strain ageing [41, 42].

The temperature has essential influence on dominant damage mechanism responsible for fatigue life of the material. The shift from cycle-dependent damage to time-dependent damage results from the rise of temperature. Typically, the damage mechanism is attributed to the cyclic loading at the room temperature, where creep contribution is negligible. The localization of the cyclic plastic strain into persistent slip bands (PSBs) in the interior of the material leads to the formation of the specific surface relief known as persistent slip markings (PSMs). PSM consists of extrusions and intrusions. Since intrusion represents the notch-like defect, it is considered as a crack nucleation site [25]. By increasing of the temperature, some materials can be susceptible to specific environmental effects resulting in damage such as hydrogen effect (titanium alloy at moderate temperatures) or dynamic embrittlement, also termed as stress assisted grain boundary oxidation (SAGBO) (polycrystalline Ni-base superalloys), for instance. Finally, need to mention the creep-dominated damage that typically evolves in the interior of the material via development of the cavities and their subsequent coalescence resulting in internal cracks formation [41, 42]. More detailed description of these mechanisms will be presented.

2.7 Damage mechanism in room temperature cyclic loading

2.7.1 Models of surface relief evolution

Mechanism of the fatigue crack initiation in crystalline materials represents a long-term interest in the study of fatigue damage. Localization of the cyclic plastic strain into PSBs and subsequent initiation of fatigue cracks in FCC metals represents the hot topic since publishing the pioneering work by Ewing and Humfrey in 1903 [43]. The microscopic study on Swedish iron fatigued in rotating bending revealed the occurrence of fatigue induced slip bands for the first time.

Early studies of the specimen surface relief after fatigue loading were accomplished by optical microscopy. Wood [44] studied different fatigued materials by method so-called taper sections. The sectioning of the fatigued specimen under a rather small acute angle to the surface and perpendicular to the traces of the slip bands allowed to obtain an considerably magnified picture of the vertical displacements at the surface, see Fig. 9.

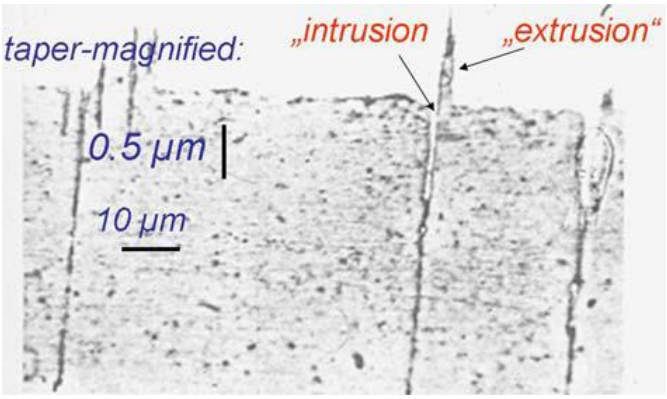

Fig. 9. Illustration of optical micrograph of taper section of fatigued copper polycrystal [44].

The observation revealed the peaks egressing from the material and notches. Studies made by Cottrell and Hull were coequally important. The experiment incorporated the high resolution of the electron microscope replica technique to image the surface relief of fatigued copper single- and poly-crystals [45]. The observations revealed formation of elevations (so-called extrusions) along the PSMs at the specimen surface as well as depressions (so-called intrusions). Based on some observation where extrusion-intrusion pairs were developed side by side it could be suggested that intrusions and extrusions form at the same time. Moreover, intrusions were supposed to be referred to as inverse mechanism of extrusion formation.

The early dislocation models put forward were outlined to interpret the observation regarding simultaneous formation of extrusion and intrusion in the form of extrusion-intrusion pair. The Cottrell and Hull model considered two dislocation sources on different slip systems to be effective in sequence, firstly in the forward and then in the reverse half-cycle, see Fig. 10 [45]. An extrusion and an intrusion are formed accordingly. The model can be questioned by the fact that the extrusion and the intrusion do not appear on the same slip system and that they are isolated and spaced apart, but mainly that the operation of the model depends on very special assumptions.

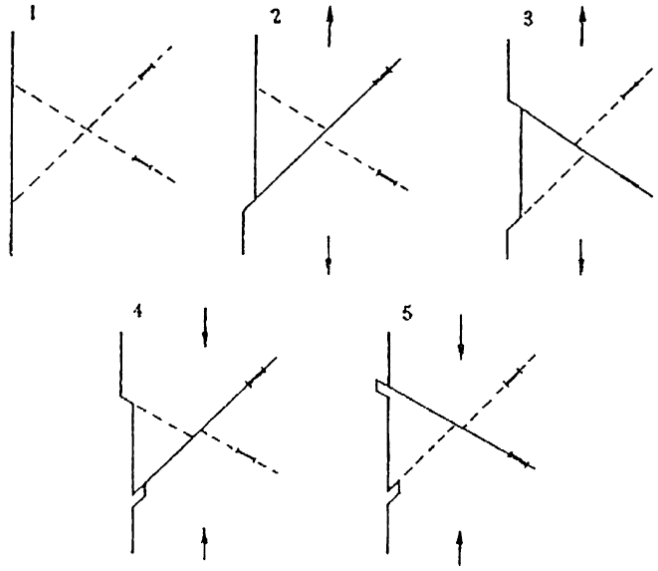

Fig. 10. Sequence of slip movements producing an extrusion and an intrusion [45].

Watt's model [46] of the surface relief evolution differs substantially from the dislocations model put forward without knowledge of the real dislocation arrangement. The most important aspect was the introduction of TEM observation as a background for the Watt's model proposed. The material investigated was copper fatigued from low to intermediate loading amplitudes. The observation revealed the dislocation arrangements formed initially during cyclic hardening consisted of dislocation clusters, so-called ''veins'', made up originally of glissile elongated edge dislocation dipole loops of either vacancy or interstitial character, see Fig. 11. When elongated loops are being swept to the surface, a vacancy or interstitial-type dipole leave behind an embryonic extrusion or intrusion. It is then expected that, when these processes take place in a statistical manner, a surface relief consisting of extrusions and intrusions will form during continued cyclic loading [46].

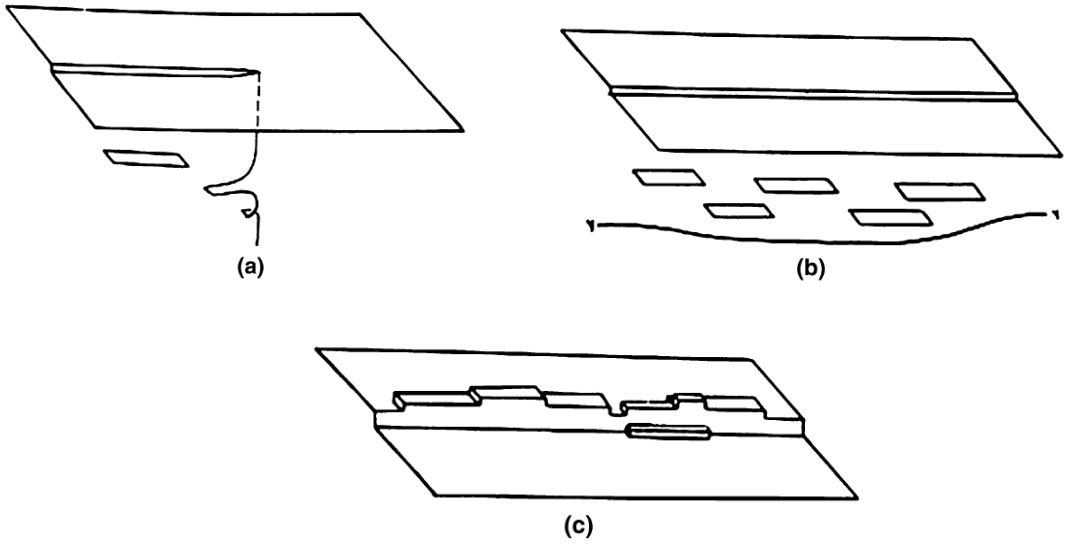

Fig.11. Watt's model of the evolution of the surface relief: (a) dipole formation, (b) dislocation approaching and transporting the dipoles to the surface, (c) emergence of dipoles and formation of the surface relief [46].

The investigation of single crystal of copper fatigued at room temperature by means of transmission electron microscope revealed specific dislocation arrangement of PBSs [47, 48]. The arrangement reminded of ladder shape and later on it was referred to as ladder like dislocation structure. However, in three dimensions, it is an alternation of thick dislocation-poor channels and thin dislocation-rich walls.

The early models of surface relief evolution included the dislocation movement and their mutual interaction based on the knowledge of dislocation arrangement of PBSs [49]. It was claimed that steady state dislocation pattern of PSBs is in relation with two processes, production as well as annihilation of the dislocations. The development of pronounced surface relief in the form of extrusion and intrusions was difficult to explain, especially when referring to an idea, that only dislocations were considered to play the dominant role in cyclic plastic straining.

2.7.2 Extrusions (and intrusions) in cyclically loaded materials

Scrutiny of the dislocation structure of cyclically strained materials by means of TEM revealed the localization of the cyclic plastic strain in ladder-like dislocation arrangement. It was found that areas from where PSBs emerge from the material on the surface form PSMs consisting of extrusions and intrusions. But the question of an actual model taking into account the relation between PSBs and PSMs remained open.

The resistivity measurement of cyclically strained copper single and polycrystals disclosed high production rate of point defects as well as their mobility at the temperatures starting from temperature of liquid helium [50, 51, 52, 53]. These important findings have become an essential background for two well-known and generally accepted models of surface relief formation and nucleation of the fatigue crack.

2.7.2.1 Essmann's model of surface relief formation

The experimental evidence of the dislocation arrangement of PBSs as well as the high production rates of point defects stimulated Essmann et al. [54] to propose the EGM (Essmann, Gösele and Mughrabi) model. The essential process of the surface relief formation is the annihilation of the edge dislocations taking place within the PSB's regions of high density of edge dislocations i.e. in the walls. Let's follow the slip activity depicted in Fig. 12a.

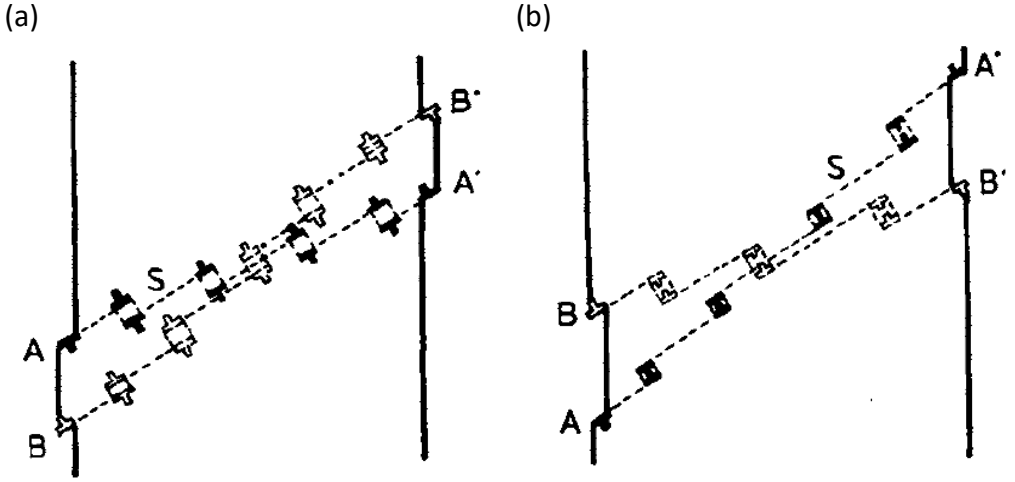

Fig. 12. Fundamental mechanisms of (a) extrusion formation, (b) intrusion formation, by chains of slide areas terminated by annihilation of dislocations [54].

The full symbols display the dislocation slip activity in tension, while empty symbols denote the dislocation slip activity in compression. The slip takes place over the whole slip band through the sequence of the microscopic slip along the line A - A' during tension. After mutual annihilation of two edge dislocations (in the ladder's rungs) on separate slip line the excess of vacancy-type dipoles left over. The chain-like sequences of annihilation processes of two neighbouring edge dislocations are illustrated in Fig. 12a. The parallel slip lines are several interatomic distances apart from the original slip lines. Considering the homogeneous dislocation flux of stacks of neighbouring 'chains' of glide processes in the PSB, then edge

dislocations will be deposited at the end of these chains at the PSB/matrix interfaces. As a consequence of the dominance of vacancy-type edge dipoles, the interface dislocations have extra half-planes within the PSB, see Fig. 13.

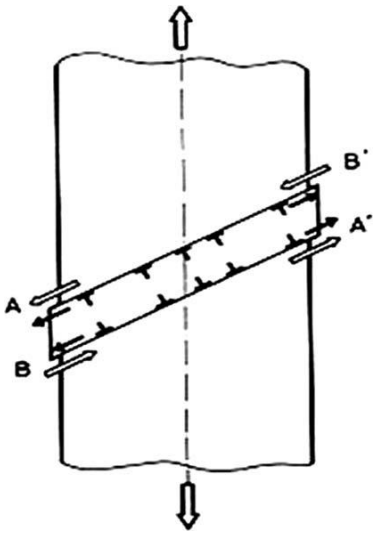

Fig. 13. The effect of external and internal stresses on interface dislocations in PSB. Open arrows mark forces caused by external stress, while full arrows denote repulsive between dislocations [54].

The interface dislocations will glide out at A and A' during the tension half-cycle, while the remaining interface dislocations will glide out at B and B' in the compression. This process leads to formation of the static extrusion. The extruded material volume is attributed to number of the vacancy concentration at annihilation sites in the walls [54]. The less plausible alternation of this mechanism is the variation in accord to the production of interstitial atoms resulting in formation of the intrusion, see Fig. 12b.

The profile of the static extrusion formed is gradually roughened by random slip in PSB during further straining [55]. The EGM model proposes following two sites of the crack initiation. It is anticipated that cracks are initiated either at the PSB/matrix interfaces or in the sharp valleys within the extrusion [56].

2.7.2.2 Polák's model of surface relief formation

Polák's [57, 58] quantitative model is based on the ladder-like arrangement of dislocations within the PSB as well as on the knowledge of the inhomogeneous high production rate and mobility of the vacancies. There are three distinctive assumptions Polák adopted to elaborate the EGM model:

- The localization of the cyclic plastic strain in the PSB leads to vacancy formation both in the dislocation walls and also in the channels.

- The vacancies formed in the channels represent the essential role in terms of mass transfer due to their migration and annihilation at the dislocations in the matrix.

- The vacancy fluxes leaving the PSB to the matrix are replaced by recently produced point defects.

The mechanisms of PSM formation does differ significantly when comparing to EGM model. The edge dislocations as well as edge dislocation dipoles serve as a perfect sink for point defects. There are two types of point defects; interstitials and vacancies produced and athermally annihilated when encountering of expanding dislocation segments in the PSB channel. The annihilation process takes place also once the interstitial and the vacancy engage. The production rate of vacancies is higher than the production rate of interstitials. The vacancy production rate given by the overall production rate minus the annihilation rate caused by annihilation with the edge dislocations and interstitials is positive at the onset of cyclic loading. The equilibrium state characterized by the steady production of vacancies and migration to dislocations meets the assumption of the Polák´s model where the interstitials are not considered at all [57, 58].

The excess of the vacancy concentration strongly depends on the sink density. Since there is a huge difference regarding the concentration in the channels and the walls, the excess of the vacancy concentration will differ accordingly. The vacancy fluxes are schematically depicted in Fig. 14a. The steady production of the vacancies in the channels and their subsequent flow under concentration gradient in the walls and the matrix leads to flow of the atoms in the opposite direction [59].

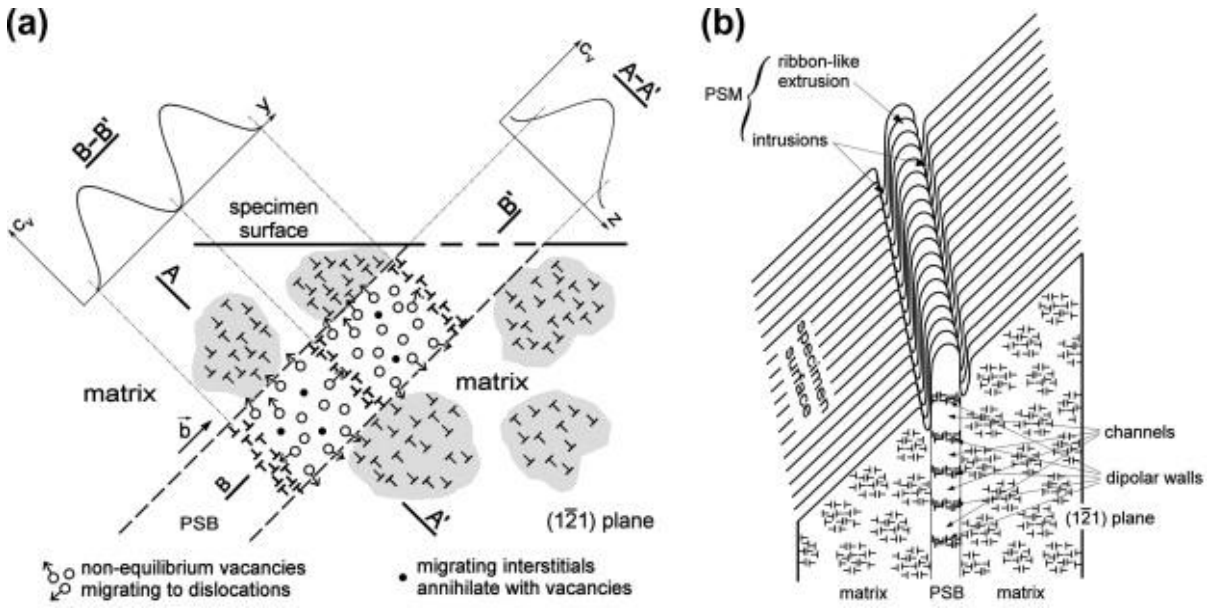

Fig. 14. Surface relief formation in the temperature range in which interstitials and vacancies are mobile; (a) schematics of ladder-like dislocation arrangement in a PSB and interstitial migration and annihilation at unit vacancy dipoles and at dislocations and (b) the shape of anticipated surface relief at emerging PSB [59].

The vacancy annihilation at the dislocation walls has no influence on the redistribution of the matter. The vacancy flow to the matrix and their annihilation at sinks close to the PSB/matrix interface leads to transfer of atoms from the matrix into the channels within the PSB and results in an accumulation of the matter in the PSB. The gradual increase of the volume takes

place in PSB lamella while the volume of two thin sheets at both PSB/matrix interfaces decreases. The mutual atom redistribution leads to the formation of the internal compression stress in the PSB lamella and internal tensile stresses in both sheets at the PSB/matrix interfaces. The internal stresses both in PSB lamella and sheets at the PSB/matrix interfaces are relaxed by the motion of the dislocations in the direction of the active Burgers vector b denoted in the Fig. 14a. The material is extruded from the PSB forming an extrusion and the intrusions on the both sides at PSM/matrix interfaces. The predicted surface relief related to the internal PSB structure is depicted in Fig. 14b. The width of the intrusions is rather small than the width of the extrusion. Moreover, since yield stress is higher in the matrix when comparing to the PSB, the intrusions occur with some delay [59].

The profile of the PSM can be calculated analytically for ladder-like dislocation structure within the PSB. Polák et al. [60] recently presented analytical model on the PSM shape prediction. Two simplifying premises needs to be considered; (a) all vacancies produced in the whole PSB migrate to the adjacent matrix, (b) homogeneously distributed edge dislocation with the density ρ_e in the matrix represent the sites where migrated vacancies get annihilated. The PSB embedded in the matrix is shown in Fig. 15. *l* denotes the depth of PSB under the surface, *w* is the width of the PSB. Provided *T* is the cycle period and D_v indicates the vacancy diffusion coefficient the profile of the vacancy concentration c_v related to distance *x* from the PSB centre can be portrayed by solving diffusion equation taking account the appropriate boundary conditions [60, 61, 62].

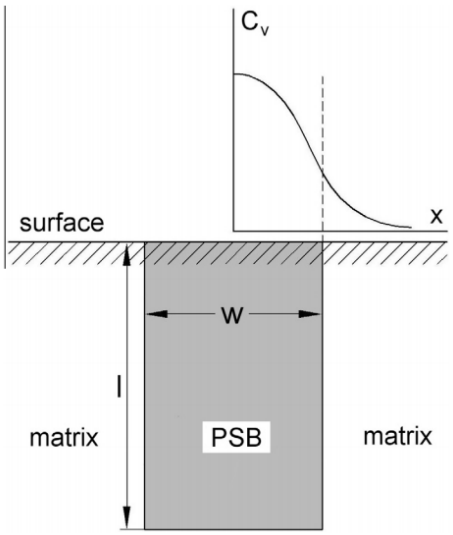

Fig. 15. Schematic drawing of a PSB having width w and length l embedded in the matrix (artificially inclined 90° to the surface) and predicted profile of vacancies migrating to the matrix and getting annihilated there at edge dislocations [60, 61].

The diffusion equation does have different forms for $x \le w/2$ and for $x \ge w/2$. Concerning the point defects generation within the PSB, their migration and athermal annihilation; the diffusion equation is

$$\frac{d^2 c_v}{dx^2} - \frac{A}{\tau D_v} c_v + \frac{p}{\tau D_v} = 0 \text{ for } x \le w/2, \tag{16}$$

where *A* is athermal annihilation coefficient and *p* is production rate of point defects. The point defects in the matrix migrate and get annihilated on the edge dislocations having density ρ_e

$$\tau D_v \frac{\partial^2 c_v}{\partial x^2} - \tau D_v \rho_e c_v = 0 \text{ for } x \ge w/2. \tag{17}$$

When appropriate boundary conditions are implemented, the vacancy profile c_v vs distance *x* from the PSB centre can be determined accordingly [61], see Fig. 15.

The growth rate r_{Ec} of the extrusion height h_E as well as growth rate r_{lm} of the intrusion depth d_l can be evaluated utilizing the relation [60, 61]

$$\frac{\Delta h}{\Delta N} = -\tau l D_v \frac{d^2 c_v}{dx^2}. \tag{18}$$

r_{Ec} is the growth rate in the centre of the extrusion (x = 0)

$$r_{Ec} = \frac{pl}{\cosh(aw/2) + \left(a/\sqrt{\rho_e}\right)\sinh(aw/2)}. \tag{19}$$

The extrusion growth rate is constant during the steady state. Hence h_E is proportional to the length of the PSB under the surface *l*, to the vacancy production rate in the PSB *p* and to the number of loading cycles. Extrusion height can be evaluated as

$$h_E = \frac{plN\cosh(ax)}{\cosh(aw/2) + \left(a/\sqrt{\rho_e}\right)\sinh(aw/2)} \text{ for } x \langle w/2. \tag{20}$$

r_{lm} denotes the peak intrusion growth rate at the PSB/matrix interface

$$r_{lm} = \frac{pl\left(\sqrt{\rho_e}/a\right)}{\coth(aw/2) + \left(a/\sqrt{\rho_e}\right)}. \tag{21}$$

The intrusion depth at the number of cycles N is given by

$$d_l = r_{lm} N \exp\left(-\sqrt{\rho_e}\left(x - w/2\right)\right) - d_c \text{ if } r_{lm} N \exp\left(-\sqrt{\rho_e}\left(x - w/2\right)\right) \rangle d_c \text{ for } x \rangle w/2 \tag{22a}$$

$$d_l = 0 \text{ if } r_{lm} N \exp\left(-\sqrt{\rho_e}\left(x - w/2\right)\right) \le d_c \text{ for } x \rangle w/2, \tag{22b}$$

where d_c is the parameter characterizing the delay between the extrusion formation and intrusion growth caused by different yield stress of the PSB and material matrix.

Fig. 16 shows the right part of symmetrical surface profile of the PSM estimated using eq. (20) and (22) along with the common set of parameters related to cyclically strained copper at room temperature [60, 61].

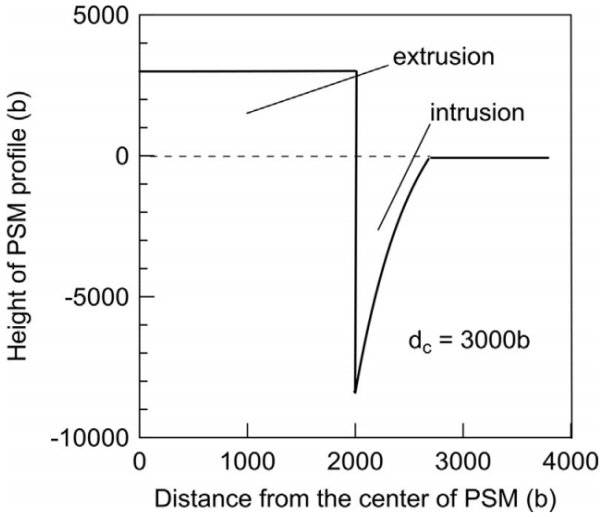

Fig. 16. PSM profile (right part of a symmetrical profile) consisting of half of an extrusion and intrusion calculated using eq. (20) and (22). It corresponds to cyclic straining of copper at room temperature for 1000 cycles. The extrusion height in the centre is $3000b$*, critical distance is* $d_c = 3000b$*. Edge dislocation density in the matrix* $\rho_e = 1\times10^{-13} m^{-2}$*. All dimensions are in units of the Burgers vector modulus b (for copper b = 2.7 × 10⁻¹⁰ m) [61].*

Currently, the ongoing experimental research on the dislocation structure arrangement in PSBs and adjacent matrix as well as on the PSMs profile has exposed many findings allowing to elaborate the models accordingly. The novel experimental techniques involved in the study of PSBs and PSMs such as high resolution scanning electron microscopy (SEM) in combination with focused ion beam (FIB) and transmission electron microscopy (TEM) [59, 63, 64], SEM equipped with FIB [65, 66, 67], atomic force microscopy (AFD) [68, 69, 70], scanning transmission microscopy (STEM) and high-resolution transmission electron microscopy (HRTEM) [71, 72] contribute to the clarification of the fatigue crack initiation at room temperature.

The specimen surface of the various materials such as ferritic steels, austenitic stainless steels and polycrystalline copper have been investigated by means of AFM. Unfortunately, the physical limitation of the AFM tip brings inaccurate image of the actual situation for two main reasons. The first one, since AFM tip cannot access into the narrow depressions, the narrow intrusions or potential cracks cannot be displayed. The second, the extrusions developed on the specimen surface emerge under and angle of approximately 45 deg. The profile detected by AFM tip is distorted at the area where the extrusion makes an acute angle with the specimen surface. This issue was overcome in the work of Polák el al. [70] where the plastic replicas of particular areas of the specimen surface were studied by AFM. More reliable picture of the PSMs can be obtained when introducing the FIB technique.

The early shape of the PSMs was investigated on 316L steel by preparation of the FIB cuts perpendicular to the direction of PSMs and to the specimen surface by Polák et al. [66]. It was

concluded that fatigue crack was initiated in the central part of the PSMs from the tip of crack-like intrusion where the depth of the intrusion was most pronounced. The detailed study on the role of extrusions and intrusions in fatigue crack initiation has been done recently [71]. Four different polycrystalline materials with FCC structure were uniaxially and biaxially loaded and subjected to study of PSMs along with PSBs by FIB sectioning and SEM observation. Subsequently, TEM inquiry of oriented surface foils was carried out. Based on the experimental results it has been concluded that the most plausible model of fatigue crack initiation includes formation of the extrusion and intrusion as the primary crack initiation site producing stress and strain concentration.

2.7.3 Mechanisms of fatigue crack growth (long cracks)

The first fatigue cracks are commonly nucleated in the early stage of the fatigue process. The fatigue life of the specimen is usually determined by the crack propagation [25]. There are two stages of the fatigue crack growth identified by Forsyth [73, 74]. In the Stage I, crack growth follows crystallographic slip planes inclined at 45° to the loading axis, while in Stage II, the crack propagates on a planes arranged approximately perpendicular to the direction of stress axis. The Stage II crack growth is gradual repetitive process, where the length of the crack increases during each cycle. The macroscopic crack length increment per cycle can be very often correlated to the striation spacing. Nevertheless, there are circumstances in which the striation spacing is lower than the crack length increment and vice versa.

Based on the fractographic study Laird and Smith [75, 76] put forward general plastic blunting model of the fatigue crack growth. Even though the model has been later modified the main idea is still preserved [77, 78, 79]. Fig. 17a depicts the unloaded state of a specimen with crack. Once the material is subjected to tensile loading, an intensive plastic deformation takes place ahead of the crack tip because of the stress concentration. The plastic strain occurs mostly in the slip planes inclined at 45° to the loading axes, see Fig. 17b.

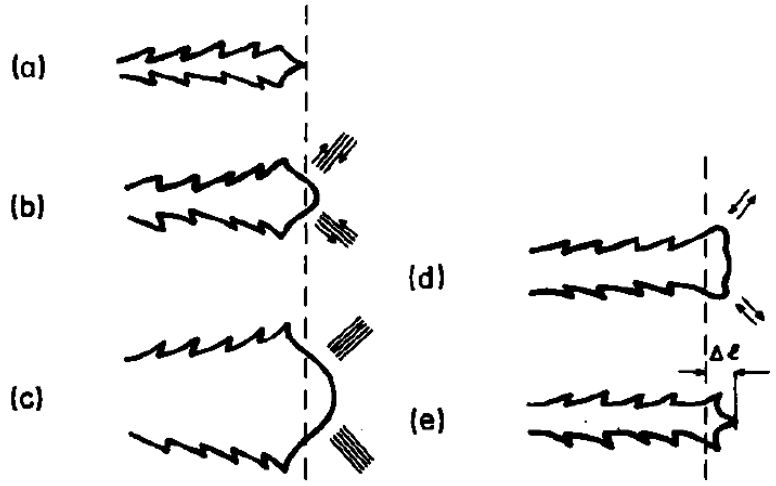

Fig. 17. Laird's model of crack propagation.

Intensification of the slip zones at the peak tensile load leads to blunting of the crack tip and its advancement (Fig. 17c). Application of the compressive stress leads to reverse evolution of the plastic deformation in the slip zones. Both newly developed surfaces resembling the 'ears' become closer without rewelding as shown in Fig. 17d. The 'ears' can be recognized on the fracture surface as striations. In the end of the loading cycle, the resulting configuration (Fig. 17e) is similar to the initial state but the crack length is larger by Δl. The basic mechanism presented results in the formation of striations.

The Laird's model illustrates the general mechanism, but it is not definitely the only option. Need to be mention that in several technical materials the mixture of transcrystalline and intracrystalline crack path may occur. Furthermore, intracrystalline crack propagation cannot be classified as a special case of the Laird's mechanism, since the plastic deformation in the slip zones of the crack tip is an inherent part of this mechanism [26]. The intracrystalline crack formation will be clarified in the following chapter.

2.8 Damage mechanism in high temperature cyclic loading

When structural materials are exposed to high temperature cycling loading several additional effects have to be considered. The influence of the temperature on material starts to be crucial when the operating temperature is higher than approximately half of the melting point of the material.

There are substantial additional effects related to the high temperature loading that need to be taken into account for the thorough analysis of the material resistance. The effect of the time factor is influential especially for long-time material exposure. The creep damage and associated creep cavity formation and their subsequent coalescence represent the internal deterioration. Moreover, the effect of the environment cannot be neglected either. The presence of the corrosive environment (air) may lead to diffusion of the oxygen in the crack tip leading to oxide layer formation and subsequent brittle fracture. It results in the accelerating of the fatigue crack growth. The synergic effect of the fatigue damage and creep deterioration along with the effect of oxidation can result in premature fracture of the component eventually [25].

2.8.1 Creep damage mechanisms

Since the creep damage is anticipated during the fatigue loading at elevated temperatures, the main features such as the nucleation and growth of creep damage should be briefly illustrated. Creep is known as a time dependent plastic deformation under constant load applied at elevated temperature for long time. The importance of the time effect is underlined by the fact that inelastic deformation occurs even if the stresses applied are less than the yield stress. Generally, creep deformation is divided in three main stages (see Fig. 18) [80].

Primary creep (I) – period of transient creep whereabouts the creep resistance of the material increases by virtue of its own deformation (strain hardening).

Secondary steady state creep (II) – The creep deformation is characterized by a constant creep rate that stems from the balance between two competing processes of recovery and strain hardening.

Tertiary stage (III) – The creep damage accumulated increases the creep rate resulting in the fracture of the material.

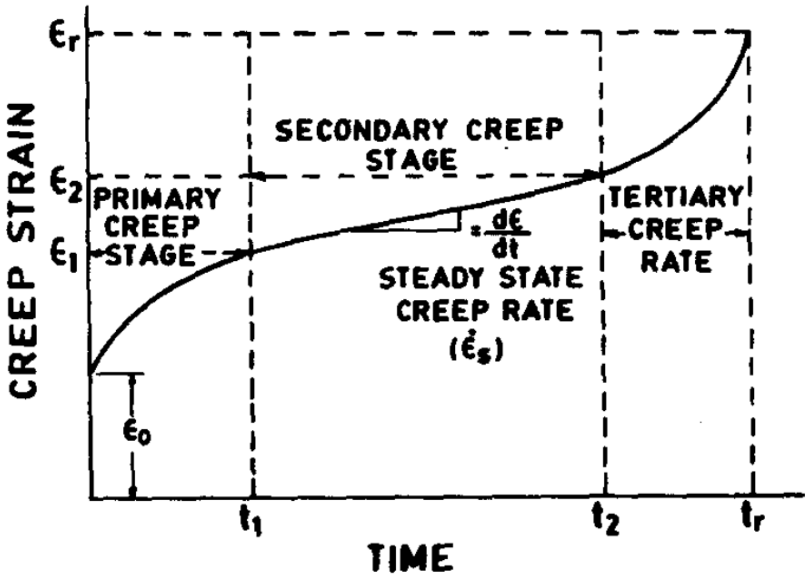

Fig. 18. Schematic creep curve showing three stages of creep [80].

The creep damage is associated with the cavity nucleation, growth of the cavities and cavity coalescence resulting in intergranular cracking during tertiary creep. Besides the cavity formation, the grain boundary sliding may lead to the formation of the sharp wedge cracks on the grain boundaries contributing to the intergranular fracture [80].

2.8.1.1 Mechanisms of creep cavity formation

The experimental study of cavity formation has revealed that the cavities commonly nucleate at the grain boundaries perpendicular to the loading axis. The mechanism of the cavity nucleation is still not well clarified, and several theories have been proposed.

(a) Dislocation pile-ups

The mechanism resembles of a Zener-Stroh mechanism [81] of micro-crack nucleation by the dislocations piled-up along a slip plane against the grain boundary. Fig. 19 shows the impingement of the dislocations on grain boundary resulting in stress concentration that may cause the cavity nucleation ahead of dislocation pile-up.

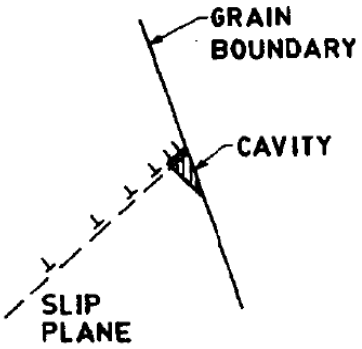

Fig. 19. Coalescence of dislocations at the head of a pile-up [80].

(b) Grain boundary sliding and cavity nucleation at grain boundary ledges

The grain boundary ledges may originate due to slip in the adjacent grains intercepting the grain boundary or they can be grown-in feature of the grain boundary. Applied load may lead to cavity formation in this regard by two possible mechanism, see Fig. 20.

- Cavity formation at the triple point of adjacent grains due to grain boundary sliding.
- The tensile boundary ledges with the respect to sliding direction experiencing tensile stresses as depicted in Fig. 20 can act as a cavity nucleation sites [80].

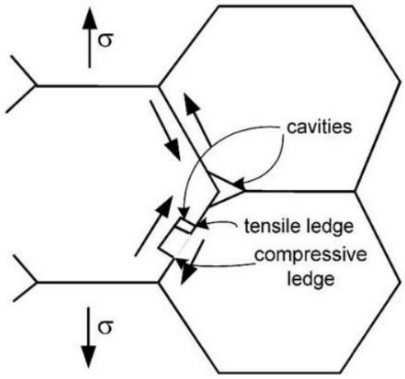

Fig. 20. Cavity nucleation at triple junction and at grown-in slip induced ledges [80].

(c) Cavity nucleation at grain boundary particles

The second phase particles located at the grain boundaries represent plausible cavity nucleation sites in structural materials. Since they reduce the grain boundary sliding, the stress concentration may occur. Cavities can nucleate due to vacancy condensation at the particle/matrix interface (Fig. 21a). Cavity nucleation at second phase can be also initiated by stress concentration due to the impingement of slip bands on particles located at the grain boundary (Fig. 21b) [80].

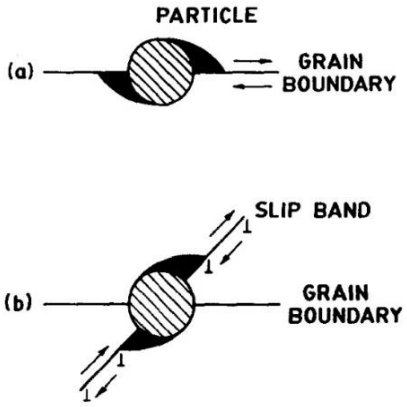

Fig. 21. Cavity nucleation mechanisms (a) Grain-boundary sliding at boundary particle (b) Slip band at grain boundary particle [80].

(d) Cavity nucleation at triple junctions and on grain boundary

The internal damage formation may occur by wedge-type cracking (w-type) at grain boundary triple points, see Fig. 22a. Since the w-type cracks are commonly found after creep testing at high stresses it has been suggested that opening up is due to sliding of the inclined grain boundaries. Wedge crack formation is sometimes referred to as a brittle decohesion of the grains. The second model of internal damage has been attributed to r-type cavities or irregularities, see Fig. 22b [80]. Stiegler et al. [82] proposed the w-type crack can be formed as an accumulation of r-type cavities. In the case of r-type cavities, they are dominantly formed at the grain boundaries, see Fig. 20b and their growth is driven by the tensile stress normal to the facet resulting in uniform distribution of the cavities along the grain boundaries. Baik and Raj [83] found that w-type damage is favoured in unsymmetrical strain-rate loading while during tension hold cycles r-type cavity formation prevails.

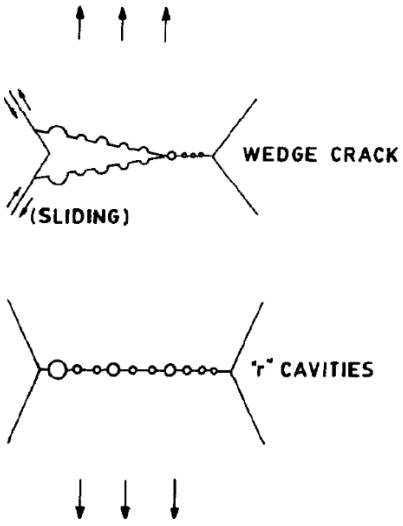

Fig. 22. An illustration for "w" and "r" type cavitation. Sliding is a necessary condition for wedge cracking [80].

2.8.1.2 Creep cavities growth

The growth of creep cavities is mostly associated with vacancy diffusion. In the terms of the diffusion growth models, the cavity serves as a sink for the flux of vacancies promoted by the applied tensile stress. The three distinct situations may appear concerning the cavity growth [80]:

(i) Broadening of the cavity due to continual grain boundary sliding (Fig. 23a)

(ii) Cavity growth caused by vacancy condensation (Fig. 23b)

(iii) Combination of grain boundary sliding and vacancy condensation (Fig. 23c).

In the different models it is assumed that the cavity behaves as a shear crack growing by the grain boundaries sliding [84].

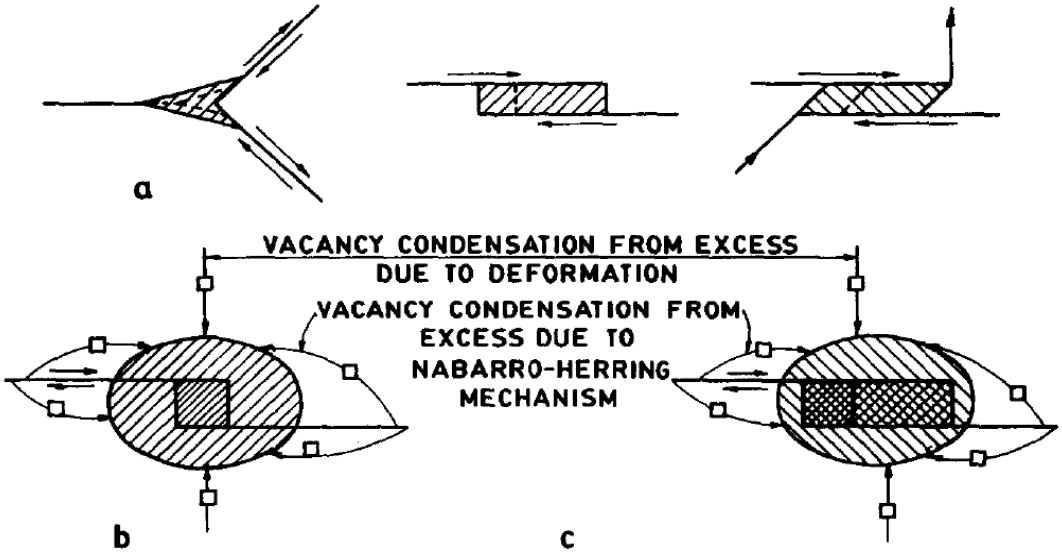

Fig. 23. Schematic of mechanisms of growth for cavities along grain boundaries [80].

2.8.2 Effect of environment

The high temperature corrosive environment can considerably affect the fatigue crack nucleation, fatigue crack propagation rate and final fracture. The aggressiveness of the environment strongly depends on material and temperature of exposure. Relatively mild environment such an atmospheric air can become highly aggressive at elevated temperatures. The body exposure to elevated temperature leads to the formation of the protective oxide layer on the specimen surface, internal oxidation and selective oxidation. Many models have been introduced to clarify the influence of fatigue-environment interaction on the damage mechanisms. Two considerably distinct mechanisms can be recognized; intergranular and transgranular crack initiation mechanisms [25].

2.8.2.1 Intergranular crack initiation

Intergranular crack initiation has been widely observed in numerous studies of different materials cyclically loaded at elevated temperatures. Preferential selective oxidation of the grain boundaries is attributed to reduced Cr-concentration near the grain boundary area due to precipitation of chromium rich particles. Moreover, the combination of high tensile stress applied along with the high temperature exposure promotes the oxygen diffusion to grain boundaries resulting in enhanced grain boundary oxidation. The mechanism is well known as stress assisted grain boundary oxidation (SAGBO). The early studies acknowledged this damage mechanism to be crucial during low-cycle fatigue of gas turbine blades [85]. Rapid intergranular crack propagation is related to the sufficiently rapid kinetics of oxide formation. Thus, the rapid crack propagation is driven by the brittle fracture of the oxide facilitated by creep cavities in the high-stressed damage zone ahead of the crack tip [86]. In this model, the diffusing oxygen reacts with an alloying element forming oxide at the head of the crack tip at the grain boundary. The oxide developed is believed to be responsible for the embrittlement resulting in rapid intergranular crack propagation.

Nevertheless, the oxide formation is not requisite premise for oxygen-induced intergranular fracture. The oxidation kinetics is temperature related and depends on material investigated as well [86]. Generally accepted model suggested by Pfaender and McMahon consists of three steps, mechanism is depicted in Fig. 24 [87]. The oxygen diffuses along the grain boundary ahead of the crack tip. The body exposure to the elevated temperature leads to enhanced diffusion rate promoted by tensile stress. Subsequent embrittlement of the grain boundary due to oxygen adsorption results in grain boundary decohesion. Lastly, the stress applied breaks the grain boundary open [87]. The intergranular failure caused by dynamic embrittlement was the subject of the early studies e.g., tin-induced cracking of Cu-Sn alloys [88], sulfur-induced cracking of alloy steels [89], oxygen-induced cracking of Cu-Be alloy [90], of a Ni-Mo-Cr alloy [91] along with the intermetallic alloy Ni_3Al [92].

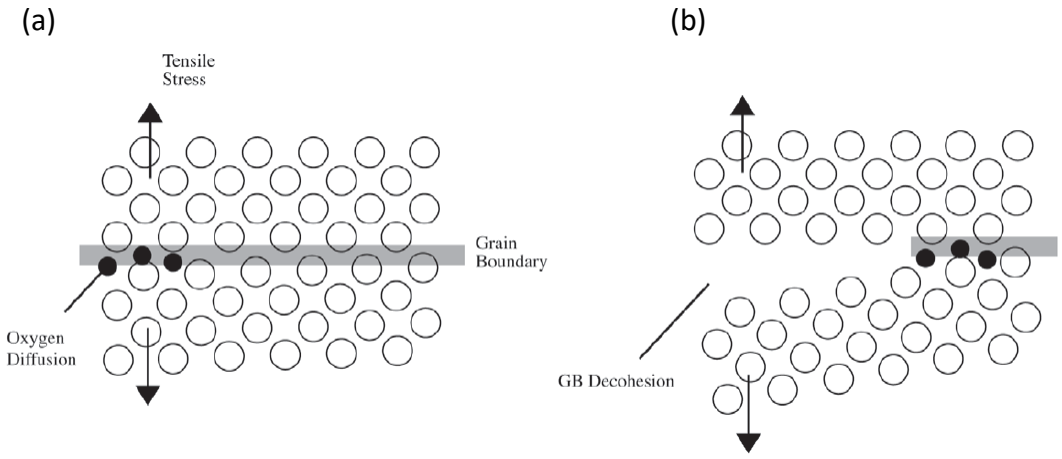

Fig. 24. Illustration of the dynamic-embrittlement mechanism [87]. (a) Oxygen diffusion along the grain boundary under action of tensile stress. (b) Cracking of the embrittled grain boundary.

Finally, let's mention the detrimental effect of hydrogen environment either in molecular or any other form termed as a hydrogen embrittlement that is mostly crucial for ferritic, martensitic and austenitic steels [26, 93].

2.8.2.2 Transgranular crack initiation

Transgranular crack initiation along with the following crack growth reflects the distinctive situation comparing to an intergranular failure. The fundamental premise is the formation of the uniform oxide layer when exposing the material to the environment at elevated temperatures. Crack initiation is considered as the random rupture of the first homogeneous oxide layer developed on the metallic surface. The repeated formation of an oxide layer at the crack tip of the fresh material and its rupture is defined as an oxide-induced crack growth. Two types of crack growth have been commonly observed:

Type I growth

The process of an oxide intrusion evolution is depicted on Fig. 25. Fig. 25a shows the oxide layer formation on the metallic surface. Once the critical thickness of the oxide layer is reached, the oxide layer breaks open and the nucleation happens (Fig. 25b). The fresh metallic surface is exposed to the environment and rapid oxidation takes place (Fig. 25c). When the thickness of the newly developed oxide layer reaches its critical value, the oxide cracks repeatedly (Fig. 25d). The oxide-induced crack gradually propagates in the material, accordingly, see Fig. 25e-f. The critical thickness of the oxide layer formed does depend on the applied strain rate, strain range and temperature [94, 95].

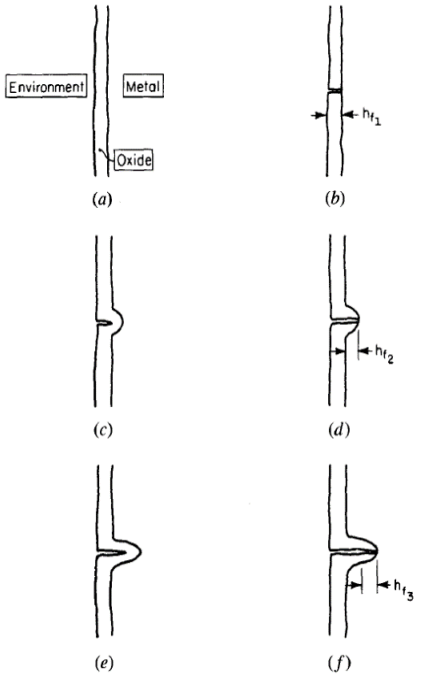

Fig. 25. Schema showing the nucleation of Type I oxide growth [95].

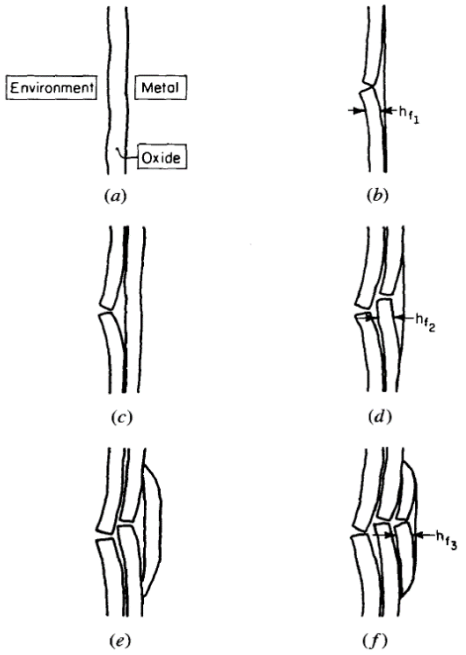

Fig. 26. Schematic showing the nucleation of Type II oxide growth [95].

Type II growth

The common attribute for this type of crack growth is the cracking of the homogeneous oxide layer provided the critical layer thickness is reached, see Fig. 26. Once the layer breaks open, it detaches from the metallic surface. In this instance, larger area of the fresh surface is exposed to the environment and the broad oxide intrusion proceeding in the material volume is produced [94].

The characteristic example of each type of the oxide growth is illustrated in Fig. 27.

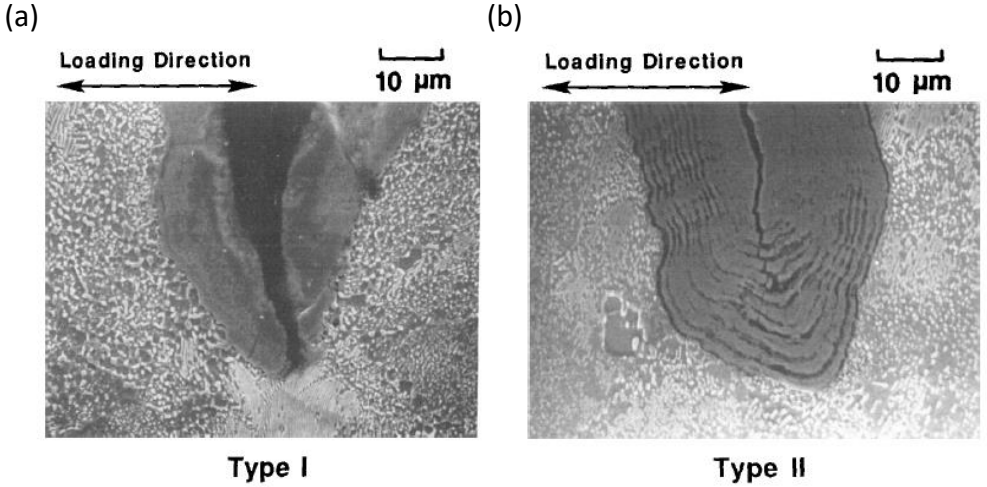

Fig. 27. SEM micrographs revealing an oxide intrusion tips resulting from (a) Type I growth (out of-phase TMF) and (b) Type II growth (isothermal fatigue) [95].

Even though it is almost impossible to simulate the actual service conditions in laboratory, the standard procedure such as isothermal low cycle fatigue loading at elevated temperature has brought rather valid results allowing to assess the damage mechanism and the fatigue life. The task is even more demanding since different materials are susceptible to different specific loading conditions. For this purpose, various alternation of the loading condition from isothermal fatigue tests with dwells to complex thermomechanical fatigue tests test have been introduced to the research.

2.9 Isothermal fatigue with/without dwells

The high temperatures have significant influence on the cyclic plasticity. The effect such as dynamic strain ageing manifesting as a repeated gradual increase and further rapid decrease of the stress during tensile (compressive) part of the loading cycle may occur in some materials. Moreover, dislocation motion is promoted by thermal fluctuations contributing to overcome of the local obstacles. The constant dislocation arrangement in the material may lead to a decrease of the effective stress component, while in the case of the recovery, the drop of the density of the mobile dislocation may result in increase of the effective stress to maintain the same strain rate [25]. The strain rate gains of its importance especially for low domain region when the cavitation as an internal damage is significant. Austenitic stainless steel 316L belongs to widely utilized materials for low and high temperature service. Therefore, a long-term effort has been made to clarify the fatigue properties along with the mechanisms of fatigue damage in detail [96, 97].

Influence of the time factor is enhanced by introduction of the hold time period into the loading cycle. Cyclic loading with the hold time period at the peak strain represents the basic creep-fatigue interaction procedure commonly conducted in laboratory conditions. Besides the damage accumulated from the cyclic loading, the creep deterioration due to the sustained loading period is anticipated as well, when exposing the material to the creep-fatigue interaction procedure. The extent of the creep deterioration depends on the material investigated and on the operating conditions such as temperature, loading waveform, applied stress and strain rate etc. Three distinctive situations may arise (Fig. 28) [98].

- The initiation of the cracks as well as further growth is fatigue dominated if high strain rates and short hold times are applied during cyclic loading see Fig. 28a.
- Application of the intermediate hold time periods and strain rates during cycling loading leads to initiation of a fatigue cracks that interact with creep damage resulting in accelerated crack growth, see Fig. 28b.
- The initiation of the internal cracks attributed to cavity formation and their mutual coalescence as well as the evolution of internal damage becomes creep dominated in cycling with low strain rate and/or long hold time periods, see Fig. 28c.

The extent of creep-fatigue interaction is related to creep ductility. The extent of creep-fatigue interaction can be significant as a result of cavity formation at the grain boundaries if creep ductility is low. In the case of high creep ductility, creep voids are commonly formed at inclusions due to particle/matrix decohesion [95].

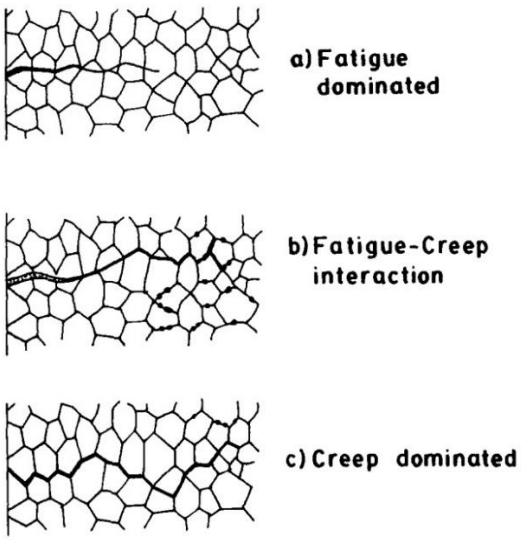

Fig. 28. Schematic diagram of failure modes during creep-fatigue interaction procedures [99].

The influence of the strain rate, dwell time in tension and compression, loading wave forms, environment as well as temperature on the fracture mode along with the fatigue life has been intensively investigated. The subject of the studies were several stainless steels such as AISI 304, 316, 316L and 348 steel [100, 101, 102]. Kim et al. [103] studied the influence of the nitrogen content on the fracture mode of type 316L and type 316LN in regard to the loading conditions. The intergranular fracture mode was found for creep-fatigue interaction tests, while the transgranular fracture mode prevailed under continual fatigue loading conditions regardless of the investigated material exposed to 600 °C [103]. Grain boundary microcracks such as wedge- and cavity-type were observed in tension hold time procedure as well as in slow-fast tooth wave shape of loading cycle [101]. The cracking mode during cyclic loading is temperature related [104]. If the material is exposed to the elevated temperature above the creep regime intergranular crack initiation along with intergranular crack propagation prevails. The increase of the hold time period introduced to the loading cycle can enhance cavity nucleation [105]. Subsequent cavity coalescence contributes to the internal integranular crack formation. The cavity nucleation as well as wedge crack development has been the subject of the studies in various stainless steels [106]. Creep-fatigue interaction results in the crack initiation on the specimen surface driven by fatigue and in development of the internal damage due to creep. The significant decrease of the fatigue life is given by encountering of these two mechanisms.

2.10 Thermomechanical fatigue

Thermomechanical fatigue (TMF) is caused by combined thermal and mechanical loading, where both the applied load (stress- or total strain-control) and temperature vary with time. Depending on the location of the component investigated and the temperature-related situation, distinctive types of strain-temperature phasing can occur. Two extreme cases, in-phase (IP) and out-of-phase (OP), are the most common procedures conducted in laboratory conditions. While in IP-TMF loading cycle, maximum temperature coincides with maximum mechanical strain, in the case of OP-TMF loading cycle maximum temperature coincides with

minimum mechanical strain. Thermomechanical fatigue is rather complex life-limiting factor for engineering components in plenty of high-temperature operations.

Generally, LCF data are widely used for design of components working at high temperatures. An attempt has been made to predict TMF life based mainly on isothermal LCF data. However, in order to predict TMF fatigue life correctly, investigation of the TMF behaviour is necessary. This is mainly due to reduced TMF lifetime compared to isothermal LCF fatigue life [107, 108].

Nitta and Kuwabara [109] proposed classification of the TMF life behaviour of metallic engineering materials, see Fig. 29. If the creep damage dominates, the combination of high temperature and tensile load during IP-TMF straining is more decisive comparing to OP-TMF straining (Type I). Since no creep contribution is assumed for OP-TMF cycling the environmental effects may result in an embrittlement of the surface giving a rise to the initiation of the early crack as a consequence of the high tensile load at low temperature. Thus, the fatigue life under OP-TMF conditions may be reduced when comparing to IP-TMF cycling. This situation is referring to the O-Type behaviour. Lastly, both types of loading conditions may result in the same fatigue life, if neither environmental effect nor creep damage prevails.

Typ		predominant damage mode
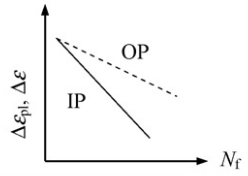	**Typ I**: IP-loading conditions cause earlier failure	creep damage
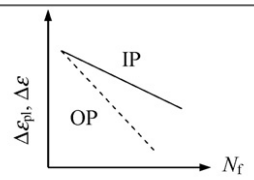	**Typ O**: OP- loading conditions lead to shorter fatigue life	environmental effects
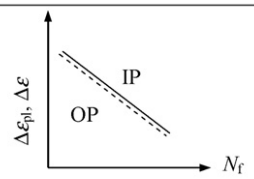	**Typ E**: IP- and OP-loading conditions show nearly the same fatigue life	neither environmental effects nor creep damage dominate
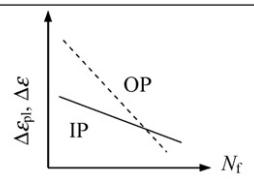	**Typ E'**: IP- loading conditions lead to short fatigue life at high strain amplitudes	creep damage only at high loading amplitudes

Fig. 29. Classification of the TMF life behaviour of engineering materials after Nitta and Kuwabara [109].

Several works have been presented on TMF behaviour and damage mechanism of individual types of stainless steel. For instance, the mechanical behaviour and fatigue life of 304 stainless steel was investigated by Kuwabara and Nitta [102, 110]. Zauter et al. [104] investigated the TMF behaviour of 304L stainless steel in vacuum. It was reported that the TMF fatigue life and damage development was governed by maximum temperature of cycling. The temperature

intervals introduced below the creep regime led to rather similar fatigue life for IP- as well as OP-TMF and transgranular crack initiation and propagation was typically observed. The differences between IP- and OP-TMF fatigue lives of 316L stainless steel in various temperature ranges were discussed by Shi et al [111]. Hormozi et al. [112] recently presented a detailed experimental study on failure of 316 stainless steel under IP-TMF and LCF loading conditions.

The extensive study of the environmental effects on thermomechanical fatigue life has been reported by Christ [113]. The investigation included three various materials to demonstrate the different susceptibility to the environment and its influence on damage evolution.

The moderate influence of an environment on TMF lifetime was observed in austenitic stainless steel AISI 304L. In low temperature regime IP- and OP-TMF resulted in similar fatigue life. Lifetime in vacuum was prolonged nearly twice the life in air (type E behaviour). Creep damage dominated, when the material was subjected to high maximum temperatures applied in the TMF cycle resulting in reduced fatigue life for IP-TMF comparing to OP-TMF cycling.

Enhanced environmental influence was found for high-temperature alloy IMI 834 [113]. In this instance not only oxidation at elevated temperatures is detrimental, but also hydrogen embrittlement at intermediate temperatures occurs. Material subjected to IP-TMF loading exhibited longer fatigue life comparing to OP-TMF loading. Hydrogen effects are crucial during OP loading, were freshly formed alloy surface is exposed to the ambient environment at intermediate temperature in tension. Since the relevant temperature range is overlapped in IP-TMF while the specimen is in compression, hydrogen effects are negligible.

TiAl-based intermetallic alloys exhibited significant environmental susceptibility and TMF fatigue life must be assessed very strictly for the design of the components. Dramatically shortened TMF fatigue life for OP-TMF loading conditions was associated with rapid oxidation-induced crack initiation. An oxide layer developed at high temperature was subsequently cracked when the specimen was subjected to tension at lower temperature. The oxide layer developed during IP-TMF at higher temperature while in tension was likely to withstand the compressive stresses without cracking [113].

3. Thesis objectives

The main intention of the dissertation thesis was to study the mechanisms that influence high fatigue and temperature resistance of the material and the mechanisms of damage under different types of loading conditions implemented. Material employed for this study was austenitic heat resistant stainless steel Sanicro 25 provided by Sandvik, Sweden.

Investigation includes the analysis and complex evaluation of the cyclic plastic response as well as fatigue life assessment. In order to bring deeper insight into evolution of the cyclic plasticity during low cycle fatigue tests at room and elevated temperatures, the experimental data were analysed using general statistical theory.

Investigation of the early stages of the fatigue damage in structural materials contributes to the understanding of the fatigue processes in cyclically loaded materials. In order to document the shape of the surface relief and thus reveal the stage-I crack under various cyclic loading conditions the scanning electron microscope equipped with focused ion beam technique was adopted. Besides the standard low cycle fatigue tests at constant temperature (room temperature and temperature 700 °C) the mechanism of the damage was investigated on the material subjected to various complex loading procedures such as creep-fatigue interaction procedures, thermomechanical fatigue and thermomechanical fatigue with dwell in the loading cycle.

The purpose of the study was to provide the basic overview of the material response along with the damage evolution under distinctive loading conditions. This contributes to the development of high temperature materials as well as to their application in the design of high temperature equipment.

4. Experimental part

4.1 Material investigated

Austenitic heat resistant stainless steel Sanicro 25 grade UNS S31035 supplied by Sandvik, Sweden in the form of cylindrical rod of 150 mm in diameter was investigated. The nominal composition in wt.% is given in Tab. 2 [4].

C	Cr	Ni	Mn	W	Co	Cu	Nb	N	S	Fe
0.1	22.5	25.0	0.5	3.6	1.5	3.0	0.5	0.23	0.2	Bal.

Tab. 2. Chemical composition of the material in wt.% [4].

The steel belongs to Fe-Ni-Cr alloy group consisting of high content of alloying elements improving the material properties. Solid solution hardening is enhanced by W, N, Co and Nb. In addition, high content of Nb, N, Cr and Cu may lead to precipitation strengthening. Good resistance to steam oxidation along with hot corrosion resistance is attributed to increased content of Cr. The stabilization of the FCC structure is ensured by Ni and N content.

Basic mechanical properties and creep resistance characteristics of the material in annealed state at room temperature and at 700 °C are listed in Tab. 3 and Tab. 4. The peak temperature for service is 750 °C [4].

Proof strength [MPa]	Tensile strength [MPa]
$R_{p0,2} \geq 310$, at 20 °C	$R_m \geq 680$, at 20 °C
$R_{p0,2} \geq 180$, at 700 °C	$R_m \geq 455$, at 700 °C

Tab. 3. Proof strength along with a tensile strength of Sanicro 25. $\mathrm{R_{p0,2}}$ *corresponds to 0.2% offset yield strength [4].*

Creep rupture strength according to VdTÜV Wb555, 09.2008, 700 °C	
10 000 h	145 MPa
100 000 h	95 MPa

Tab. 4. Creep rupture strength [4].

Sanicro 25 exhibits very good resistance to hot corrosion in a coal ash environment. Oxidation tests performed in the air at various temperatures followed by cooling to room temperature after different period of the exposure indicated very low mass rate change. Oxidation resistance was found to be very promising based on the oxidation test in aqueous steam at 600 °C and 700 °C for 500 and 1000 hours, respectively [4].

Half-products of specimens of different geometries were produced from the supplied cylindrical rod parallel to the ingot axis. Specimens were heat treated by solution annealing at the temperature of 1200 °C for one hour and cooling in air followed. For the purpose of the

subsequent study of the specimen surface by means of SEM to identify the responsive mechanism of damage, the gauge lengths of the specimen surface were mechanically and electrolytically polished. The geometry of the cylindrical specimens for different loading procedures is given in Tab. 5.

Testing procedure	Diameter [mm]	Gauge length [mm]
RT	8, 7*	14, 16*
IF	6	15
IF-D	6	15
IP- and OP-TMF	7	16
IPD- and OPD-TMF	7	16

*Tab. 5. Specimen geometry. * the geometry of the specimens subjected to investigation of the surface relief formation and crack nucleation.*

4.1.1 Specimen before testing

The electrolytically polished specimen surface before cyclic straining is displayed in Fig. 30. The typical grain size specified by the intercept method is about 60 μm. Some larger grains of the size up to 200 μm can be spotted in the structure. The observation of the specimen surface revealed different groups of precipitates developed. The spherically formed precipitates of average size of 400 nm decorate the grain boundaries. The smallest precipitates having approx. 100 nm in average represent the most numerous group developed mainly within the larger grains (20 μm and more). The small grains are mostly free of precipitates. In addition, the chain-like arrangements of the larger precipitates elongated in the direction of the specimen axis were observed. The chemical composition of the precipitates was identified utilizing STEM mode along with EDS technique. The particles were determined as a complex nitride (Cr,Nb)N, i.e. Z-phase. Moreover, the secondary chromium carbides $M_{23}C_6$ were observed primarily at low angle grain boundaries [114].

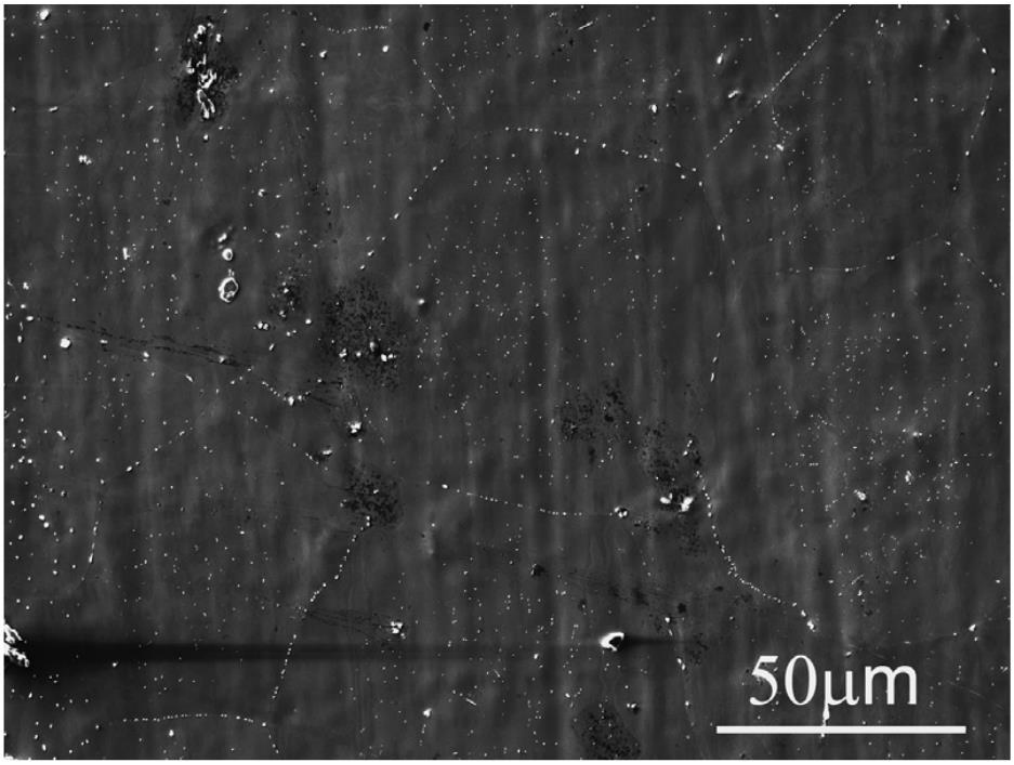

Fig. 30. Polished surface of the Sanicro 25 steel after 1 h annealing at 1200 °C followed by cooling in air.

4.2 Loading procedures

All experiments were carried out by means of computer-controlled servo-hydraulic mechanical testing system with hydraulic grips. Symmetric cyclic tension-compression straining (triangular shape wave form; R_ε= -1) with total strain amplitude control at constant strain rate was applied to the individual specimens. For the purpose of simplicity, the specific experimental set-ups used along with the loading conditions implemented (total strain amplitudes, strain rate etc.) will be listed for individual cyclic loading test. The large amount of data points was recorded for each hysteresis loop allowing the analysis of the cyclic plastic response of the material in agreement with statistical theory of the hysteresis loop in isothermal cyclic loading.

Firstly, tensile tests at room temperature as well as at 700 °C were conducted. Tensile tests were performed with extensometer used mostly for high temperature cyclic loading. The tests were performed at constant strain rate 2×10^{-3} s^{-1}. In the beginning of tensile test, the displacement and the strain measured by the extensometer were recorded. Once, the maximum strain range of the extensometer was reached, the extensometer was removed. Subsequently, the test was performed in displacement control at displacement rate corresponding to constant strain rate chosen.

In room temperature cyclic loading the specimens were cyclically strained at constant strain rate 5×10^{-3} s^{-1}. Total strain amplitudes ε_a in the interval from 2.5×10^{-3} to 1×10^{-2} were

applied to the individual specimens. The strain was measured and controlled with an extensometer having 8 mm base.

Two types of cyclic loading test were performed at 700 °C; isothermal fatigue (IF) tests and isothermal fatigue tests with 10 min tensile dwell introduced to the loading cycle at the peak strain (IF-D). The specimens were gripped by the high temperature grips in the split three-zone resistance furnace. The temperature in the chamber was controlled during the procedure by three independent thermocouples to avoid the thermal gradient. The strain was measured by high temperature extensometer with ceramic rods having 12 mm base. The specimens were subjected to isothermal fatigue loading at 700 °C under constant strain rate 2×10^{-3} s^{-1}. Total strain amplitudes ε_a in the interval from 2×10^{-3} to 7×10^{-3} and from 2.5×10^{-3} to 5×10^{-3} were applied to the specimens in IF and in IF-D tests, respectively.

Distinctive experimental setup was implemented in the study of thermomechanical fatigue. The temperature was controlled by high frequency inductive heating generator from Hüettinger. The cooling of the specimen during thermomechanical cycles was managed by water cooled clamping jaws along with the air flow. The specimen temperature was measured and controlled utilizing the ribbon thermocouple Type-K wreathed over the specimen in the middle of the specimen gauge length. The extensometer with ceramic bars had 12 mm base. The high temperature extensometer was attached to the specimen surface in the centre of the gauge length. The strain and the temperature were controlled using digital control system. Triangular wave shape form was adopted for mechanical and thermal cycling. The specimens were subjected to TMF loading in two extreme loading cycles; in-phase (IP-TMF) and out-of-phase (OP-TMF). Moreover, the influence of the creep component was simulated by introducing of 10 minutes dwells in the loading cycles. The respective tests are designated as IPD-TMF and OPD-TMF tests. Temperature interval from 250 to 700 °C and the alternation of temperature with the rate 4 K/s was chosen. Since the rate of temperature alternation was constant the strain rate was different for individual amplitudes of applied mechanical strain. Thereby, calculated strain rate is 5.3×10^{-5} s^{-1} and 1.07×10^{-4} s^{-1} for the lowest strain amplitude 3×10^{-3} and for the highest strain amplitude 6×10^{-3}, respectively. The mechanical strain was determined and controlled as a total strain minus the thermal strain. The fatigue life N_f was evaluated as a number of the cycles when 10 % of the stress range under a tangent line through the last points of the saturated part of the stress response curve in linear scaling was reached [115].

4.3 Techniques utilized for the analysis of the damage mechanism

The scanning electron microscope Tescan Lyra3 XMU FESEM equipped with focused ion beam along with X-Max80 energy dispersive X-ray spectroscopy detector for X-ray microanalysis and electron back-scattered detector by Oxford Instruments with Aztec control system was employed for the systematic scrutiny of the cyclically strained specimens.

4.4 Analysis of the hysteresis loops by means of statistical theory

The large amount of data points was recorded for each hysteresis loop in order to allow the analysis of the cyclic plastic response of the material in agreement with the statistical theory of the hysteresis loop [25, 30, 31]. The procedure embraced the evaluation of the effective stress component along with the distribution of the internal critical stresses from the experimental data and comprises of the following steps:

1. Step: The transformation of the hysteresis loop segment to the relative coordinates in accord with eq. 14a and 14b, see Fig. 31 (tensile half-loop is considered).

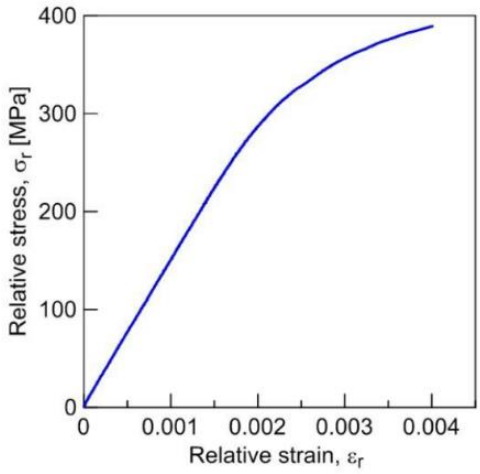

Fig. 31. The tensile hysteresis half-loop.

2. Step: The digital differentiation of the data and subsequent smoothing procedure of the segment in relative coordinates is applied for the evaluation of the first and the second derivatives. Accordingly, the effective elastic modulus E_{eff} is determined from the first derivative at the point where the second derivative of the segment reaches its first minimum, see Fig. 32.

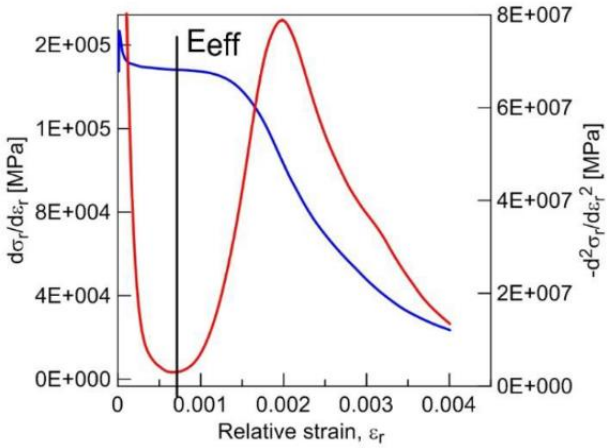

Fig. 32. The first and second derivative.

3. Step: In order to evaluate the effective stress component along with the distribution of microvolumes having internal critical stresses in agreement with the general statistical theory, the unique representation is required. The second derivative is therefore multiplied by $-2/E_{eff}^2$ and plotted vs. fictive stress $\varepsilon_r E_{eff}/2$. The shift of the probability density function from the origin represents the saturated effective stress, see Fig. 33.

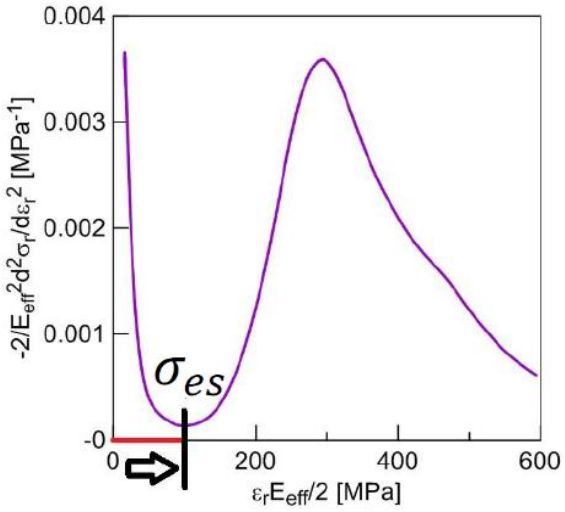

Fig. 33. The second derivative in unique representation in accord with the statistical theory of the hysteresis loop.

4.5 Investigation of the damage mechanisms

In the study of the fatigue crack nucleation at room temperature, the cyclic loading was regularly interrupted at selected number of the cycles. Accordingly, the specimen surface was observed using SEM at the several locations. FIB technique was employed in the locations where PSMs were formed to reveal the profile of the surface relief. In order to prevent the surface distortion by the incoming ion beam and thus to identify the actual profile of the PSMs, the protective platinum layers were deposited on these locations. Since there is a contrast difference between the layers deposited by electron- and ion-beam, the two-layer deposition was adopted to distinguish unequivocally the material from the deposition. The 1st thin layer was deposited by electron beam induced deposition followed by the thick layer deposited by the ion beam induced deposition. Lastly, the FIB trench was produced at the area oriented perpendicularly to the surface and to the direction of the PSMs. Moreover, in order to obtain the detailed SEM image of the PSM profile, perpendicular cut was smoothened by ion beam with significantly reduced intensity. Further cyclic loading resulted in the evolution of the surface relief also on the plane of the perpendicular cut. Hence, to clearly identify the modification of the PSM profile due to prior loading, the perpendicular cut had been smoothened with low intensity ion beam before further SEM observation was realized. This approach was repeatedly applied when additional cycles were implemented.

The methodology of the damage mechanism investigation of the specimens subjected to high temperature loading did not differ significantly. Predominantly the secondary cracks developed on the specimen surface were studied to assess the crack nucleation sites. In this regard SEM was involved in the study of the specimen relief in general. The importance of the oxidation processes can be estimated from the investigation of the profiles of the oxidized secondary cracks. For this purpose, FIB technique was utilized along with the deposition of the platinum layer when needed. In addition to the study of the surface cracks formation, the evolution of the internal damage due to creep was investigated on the longitudinal cross-sections of the specimen gauge length produced parallel to the stress axis. The longitudinal cross-sections were mechanically polished and re-polished by diamond paste. In order to document the crack path and its relation to the grain orientation within the material, longitudinal cuts were subjected to the EBSD. Furthermore, the chemical composition of the oxide layers developed was identified by means of EDS.

5. Results

The result section is divided into five chapters related to specific loading conditions applied. These chapters are further split into subheads devoted to cyclic plastic response of the material and experimental investigation of the distinctive damage mechanisms on the strained specimens. Short outcomes are given in the end of every chapter to briefly summarize the main findings.

5.1 Tensile tests

Stress-strain representation of the tensile test plotted in engineering units at room temperature and at 700 °C is depicted in Fig. 34. Tensile stresses at room temperature are significantly higher comparing to those at elevated temperature. Tensile parameters evaluated are given in Tab. 6.

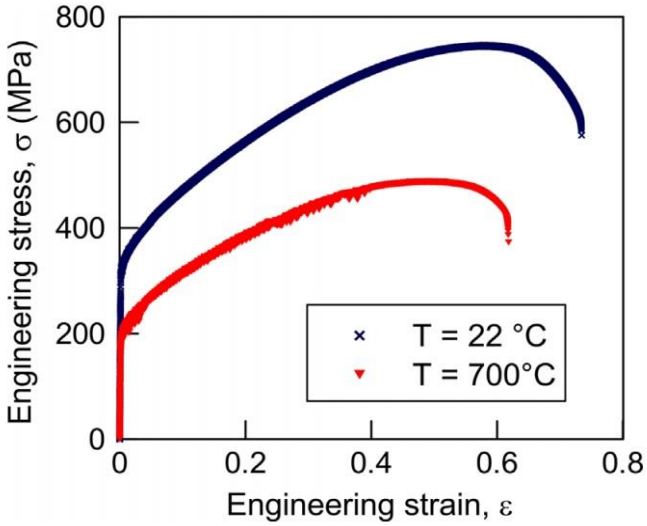

Fig. 34. Tensile stress–strain curves of the Sanicro 25 steel at two temperatures.

$T\left(^{\circ}C\right)$	$E\left(GPa\right)$	$R_{p0.2}\left(MPa\right)$	$R_m\left(MPa\right)$	$A(\%)$
22	200	320	740	59
700	130	190	487	51

Tab. 6. Tensile parameters of Sanicro 25 steel at two temperatures.

5.2 Room temperature cyclic loading

5.2.1 Cyclic hardening/softening curves

The response of the material subjected to room temperature low cycle fatigue loading is depicted in Fig. 35. The figure shows the cyclic hardening/softening curves for variety of constant total strain amplitudes applied to individual specimen. Stress amplitude σ_a is plotted vs number of the cycles *N* in Fig. 35a. The relation between the plastic strain amplitude ε_{ap} and number of cycles for the same set of total strain amplitudes is documented in Fig. 35b. The initial cyclic softening from the onset of the cyclic loading is observed for the lowest total strain amplitudes 2.5×10^{-3} and 3×10^{-3}. The material hardens slightly for the intermediate total strain amplitudes applied but most of the fatigue life is spent in cyclic softening. Only the highest total strain amplitudes manifest significant cyclic hardening in the commencement of the loading followed by softening. Fig. 35b documents the evolution of the plastic strain amplitude that is in accord with the stress amplitude development. The tendency of saturation of plastic strain amplitude during the fatigue life is noticeable for all loading tests regardless of the total strain amplitude applied.

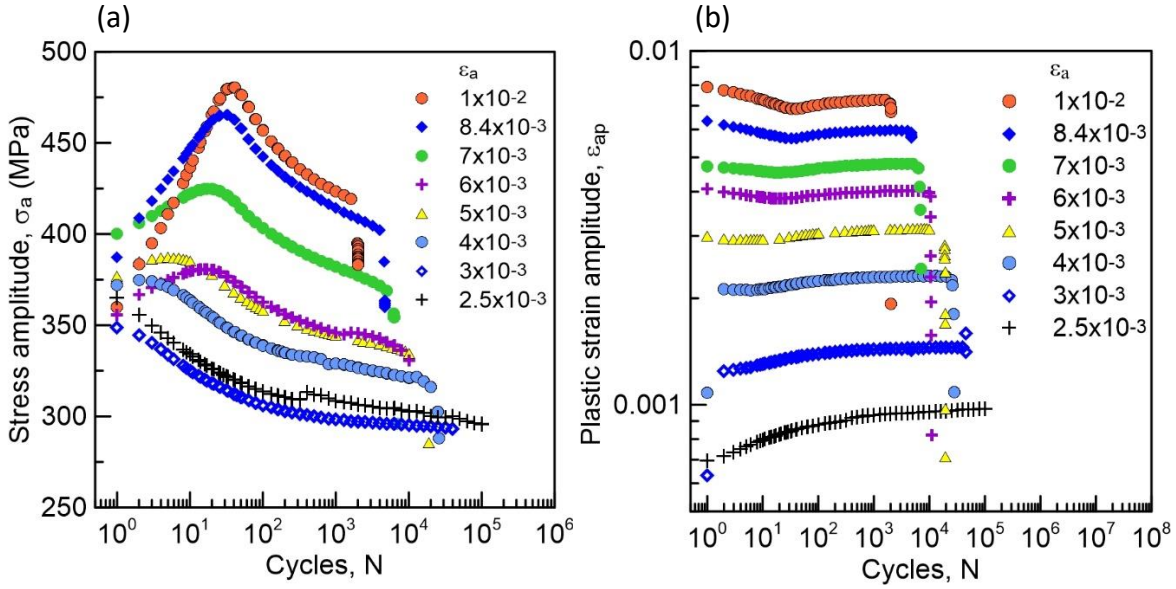

Fig. 35. Cyclic hardening/softening curves in constant total strain amplitude loading at room temperature, (a) stress amplitude vs. number of cycles, (b) plastic strain amplitude vs. number of cycles.

5.2.2 Statistical analysis of the hysteresis loop

The deeper insight in the mechanisms of the cyclic plastic straining is disclosed when applying the statistical theory of the hysteresis loop. For this purpose, the segments of the hysteresis half-loops are subjected to the procedure described in sec. 4.5. Fig. 36 and Fig. 37 document the evolution of the second derivative of the hysteresis half-loop multiplied by $-2/\left(E_{eff}\right)^2$ plotted vs. fictive stress $\varepsilon_r E_{eff}/2$. Let's consider the following convention; the tensile and

compressive half-loops are labelled as segments (sgm), while all even segments represent tensile segments and all odd segments are compressive segments.

Fig. 36 demonstrates room temperature cyclic loading with low strain amplitude for the tensile and compressive segments. The point where the second derivative drops to zero is equal to the effective stress. The probability density function is characterized by two peaks having rather similar height, but different effective stresses derived from the position of the peaks onsets. The second peak gets gradually reduced and diminishes during cycling. The first peak escalates and furthermore shifts to the lower values of the fictive stress. Accordingly, the microvolumes having smaller internal critical stresses tend to be more effective that is in agreement with the cyclic softening. Eventually, the distribution of the microvolumes is identified by one peak located at the fictive stress around 210 MPa. When comparing the second derivatives of tensile and compressive segments, the evolution of the shape of both segments is in good agreement.

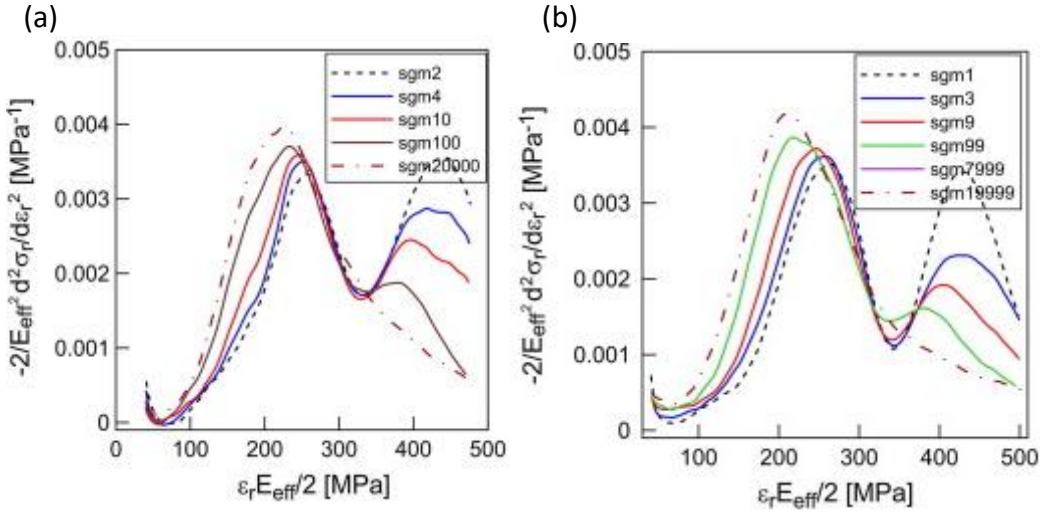

Fig. 36. Evolution of the second derivative of the tensile and compression segments in room temperature cycling with strain amplitude $\varepsilon_a = 2.5 \times 10^{-3}$ during the fatigue life (a) tensile half-loops (segments), (b) compression half-loops (segments).

Fig. 37 shows the response of the material to loading with total strain amplitude $\varepsilon_a = 5 \times 10^{-3}$. Comparing to the low strain amplitude cycling, the development of the second derivative for cycling with high strain amplitude differs especially when considering the evolution of the small second peak. Overall, no remarkable change of the probability density function comparing to straining with $\varepsilon_a = 2.5 \times 10^{-3}$ was observed. The initial shape of the second derivate is described by a large peak centred at fictive stress 240 MPa and relatively small peak centred at 630 MPa. During continuous cyclic loading the second small peak got vanished completely and the first peak got slightly shifted to the lower fictive stresses. Both these attributes refer to cyclic softening.

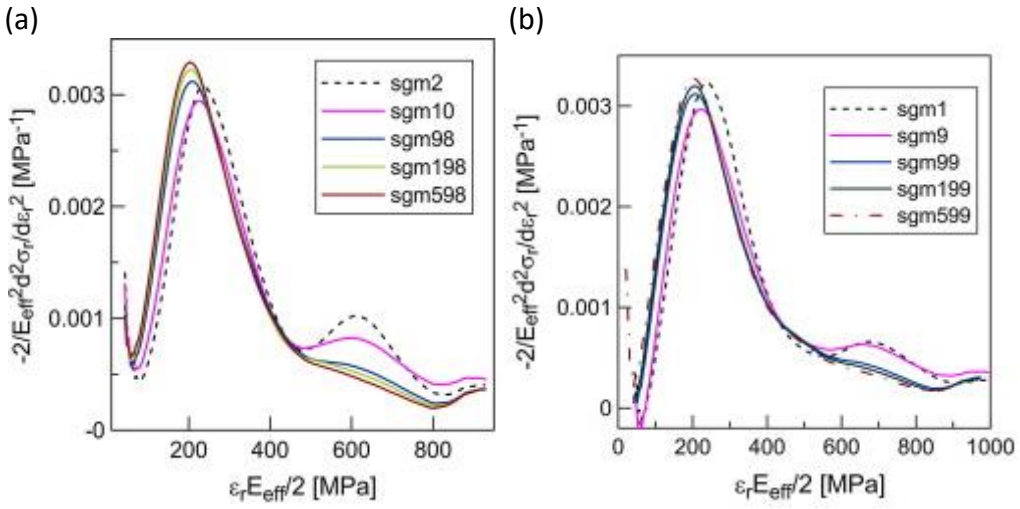

Fig. 37. Evolution of the second derivative of the tensile and compression segments in room temperature cycling with strain amplitude $\varepsilon_a = 5 \times 10^{-3}$ during the fatigue life (a) tensile half-loops (segments), (b) compression half-loops (segments).

5.2.3 Surface relief observation

The polished gauge length of the specimen was studied by means of SEM equipped by FIB technique. At selected number of the cycles, the test was interrupted and the specimen surface was exposed to detailed observation by SEM. At some particular locations, the FIB trench was introduced to identify the actual in-depth profile of PSMs. Fig. 38 represents the stress amplitude plotted vs. the number of the cycles and provides the schedule of the individual steps of investigation.

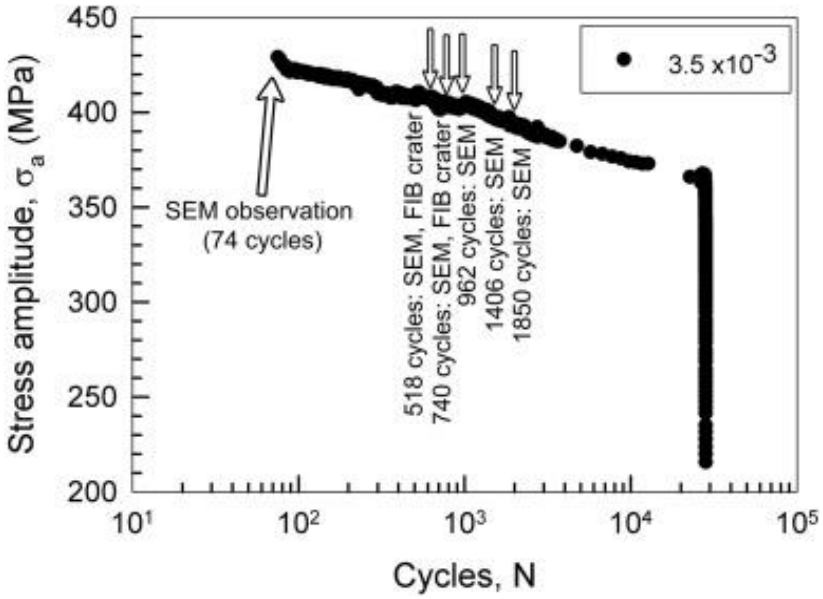

Fig. 38. Stress amplitude vs. number of cycles in constant total strain amplitude test. Arrows indicate the SEM observations and FIB milling.

The formation of surface relief starts in the very beginning of the fatigue life. The surface of the specimen cyclically loaded with strain amplitude $\varepsilon_a = 3.5 \times 10^{-3}$ after 74 cycles is shown in Fig. 39. Already after 74 cycles (0.25 % N_f), the early PSMs can be clearly recognized.

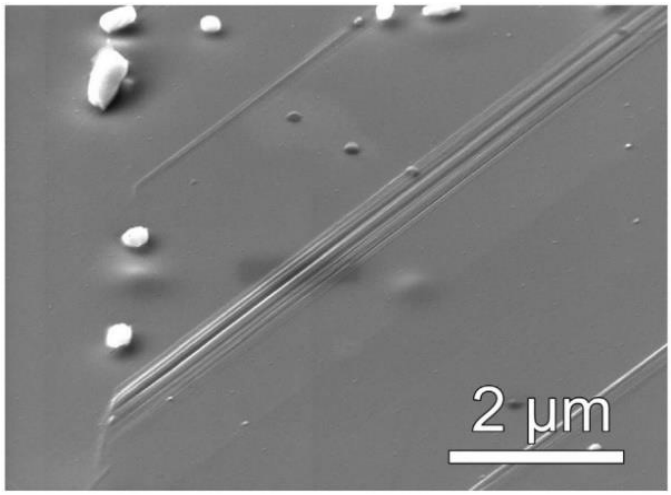

Fig. 39. Surface of the Sanicro 25 after 74 cycles with strain amplitude $\varepsilon_a = 3.5 \times 10^{-3}$.

It is noticeable that PSMs developed are very fine and the image indicates the occurrence of elevations and depressions within the central PSM. Additional cycling leads to gradual evolution of the PSMs profile. Generally, existing PSMs get broader i.e. their width gets expanded while entirely new PSMs are formed simultaneously.

Based on the prior studies of the surface relief it was anticipated that interval from about 500 to 2000 cycles could be crucial for the fatigue crack initiation. The representative specimen surface after 740 cycles is shown in Fig. 40.

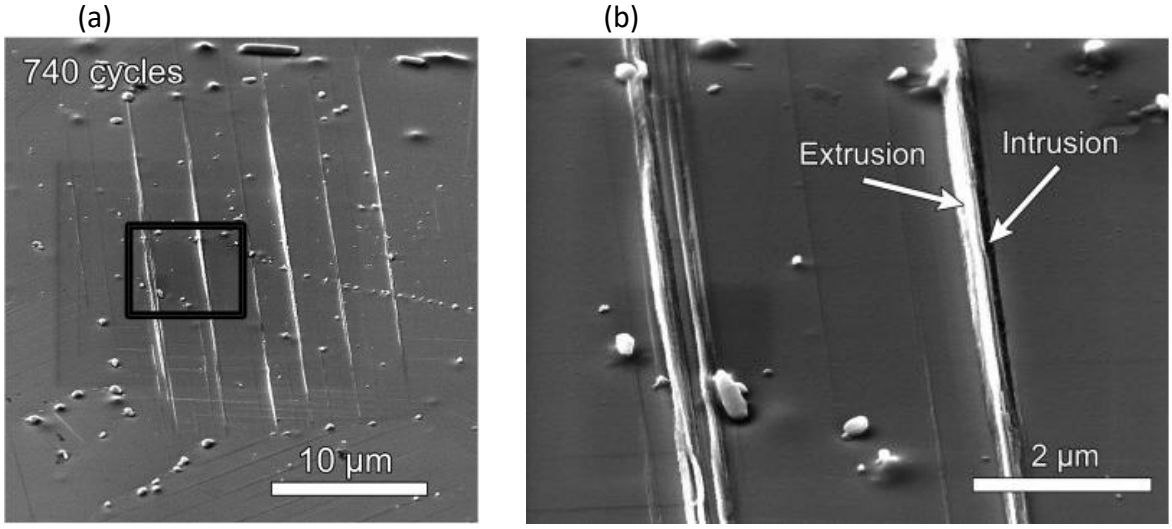

Fig. 40. SEM image of the surface relief in a grain of Sanicro 25 cycled at room temperature with total strain amplitude 3.5 x 10^{-3}; N_f =740 cycles (a); (b) enlarged area marked with black rectangle in (a).

The observation by means of SEM revealed six parallel PSMs within one grain. Higher magnification of the area marked with black rectangle in Fig. 40b reflects the diversity of the PSMs shapes. Two PSMs consisting of alternation of pronounced extrusions and intrusions can be distinguished. Unequivocal existence of the early crack could be just guessed; hence FIB was used to obtain the reliable information of the PSMs profile in three dimensions.

5.2.4 FIB cutting

The experimental study involving SEM observation combined with the FIB technique of three characteristic locations on the specimen surface is presented. The investigation included the picture of the surface studied, its in-depth profile at the position of FIB cut line and pictures of the following evolution of the PSM's profile during cyclic loading.

The first location

The surface of the first location chosen is shown in Fig. 41. Three well developed PSMs are presented along with the FIB cut line denoting the location of future FIB trench. This area was covered by two layers of platinum and FIB crater was produced perpendicular to the direction of PSMs.

Higher magnification of the area marked with the rectangle in Fig. 41b is shown in Fig. 42a. The detailed cross-section documents the complexity of the PSM profile consisting of extrusions and intrusions. In addition, the net step between the surface to the left and to the right of the PSM can be recognized. Considering the inclination of the electron beam to the perpendicular surface the height of the step was estimated to 30 nm. Deep intrusion on the left side of the PSM in a close neighbourhood of pronounced extrusion can be recognized.

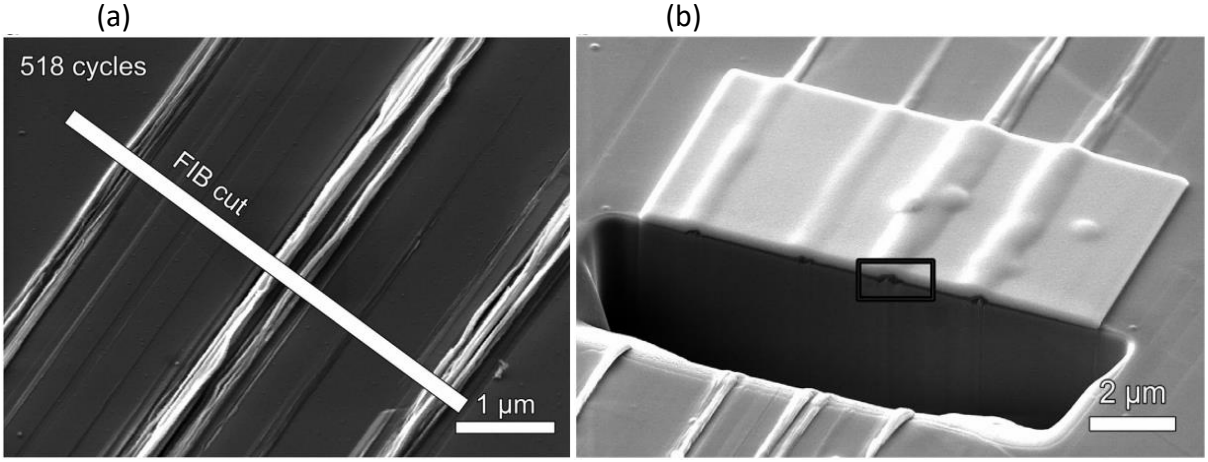

Fig. 41. Specimen surface at 518 cycles with an overall view of PSMs (a); platinum layer and a rectangular crater produced using FIB technique (b).

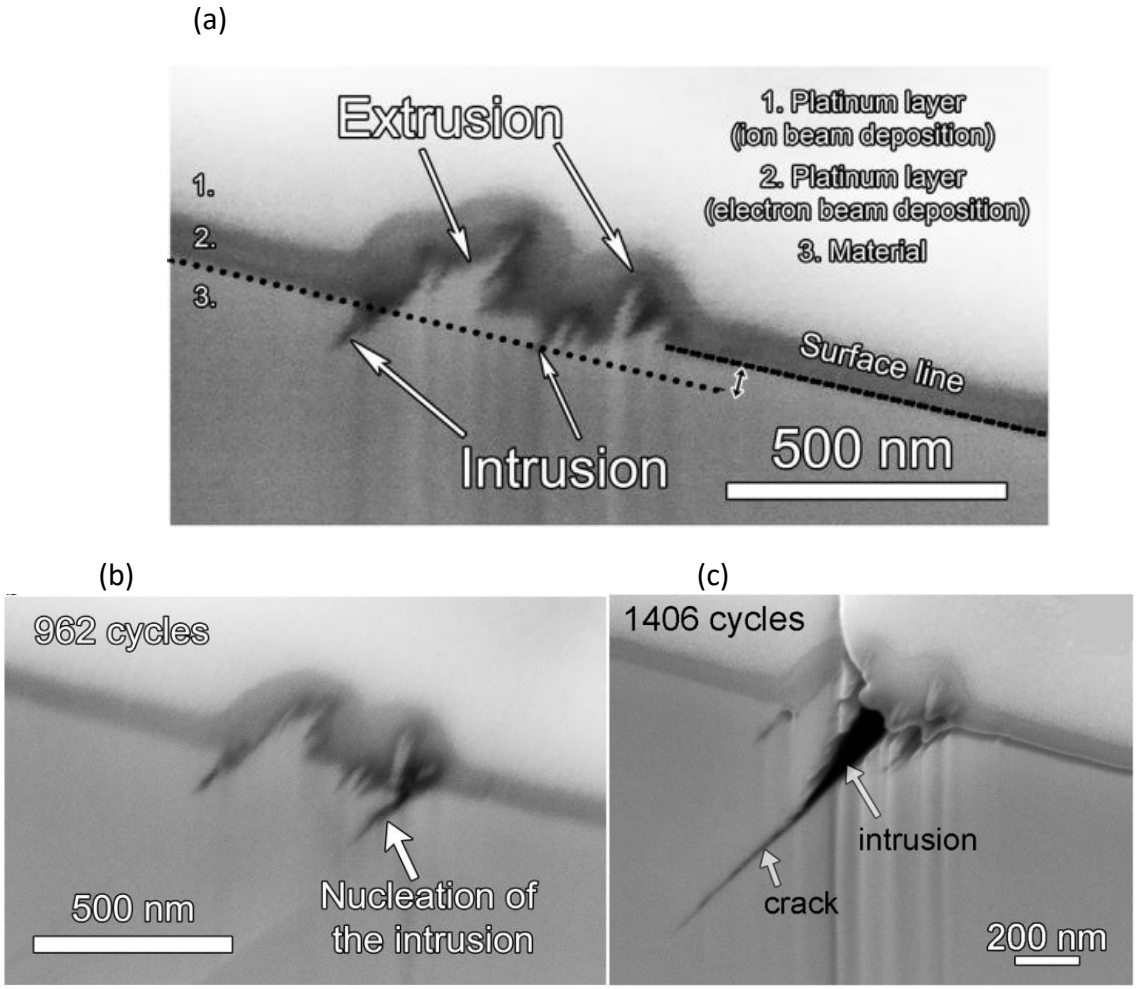

Fig. 42. The detail of the investigated area from Fig. 41b at different stages of the fatigue life; (a) detail of the PSM after 518 cycles; (b) nucleation of another intrusion at 962 cycles; (c) initiation of stage I crack at 1406 cycles.

The specimen was subjected to additional cyclic loading and to SEM observation as well. The evolution of the PSM profile during the cycling is documented in Fig. 42b at 962 cycles and Fig. 42c at 1406 cycles. Fig. 42b shows the formation of the very new intrusion in the right section of the PSM. This represents the most significant change in the PSM profile when additional cycles were implemented. No important change in the profile in the left side of the PSM was recorded. The image taken after 1406 cycles shows considerable modification of the PSM profile. The previously developed intrusions on the both interfaces between PSM and the matrix did not lead to the initiation of the fatigue crack. However, additional cycles resulted in formation of the massive intrusion in the centre of the PSM instead. The depth of the intrusion is crucial and represents the crack like defect. The stage I crack started from the tip of this intrusion.

The second location

Another location exposed to the study is presented in Fig. 43. There are four parallel PSMs developed after 740 cycles. Fig. 43b shows the trench produced by FIB at the location denoted

in Fig. 43a by FIB cut line after two-layer deposition. The detailed study of the two areas marked by the rectangles at the cross-section is presented in Fig. 44 and Fig. 45.

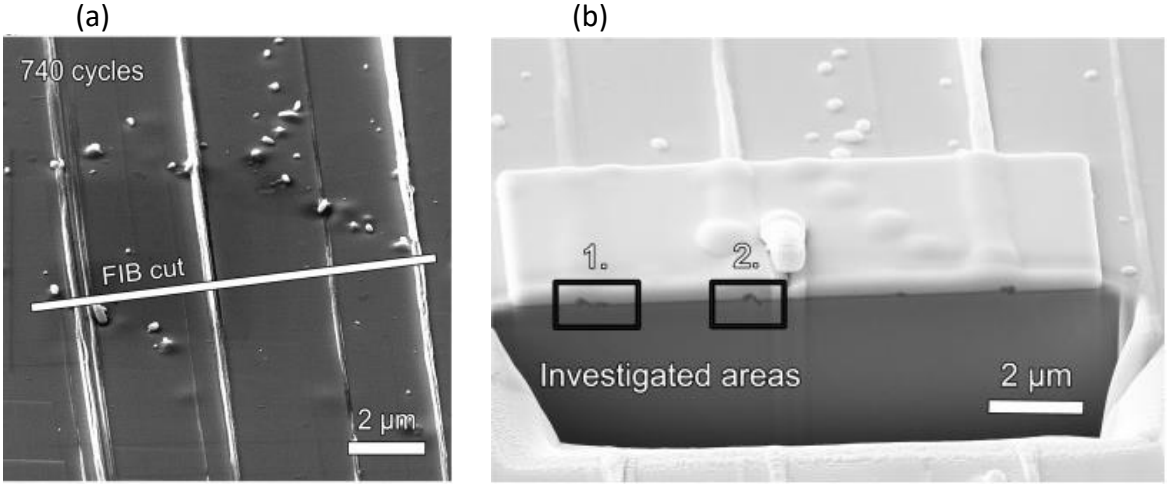

Fig. 43. Specimen surface at N = 740 cycles, (a) overall view of PSMs, (b) rectangular crater produced using FIB, two investigated areas.

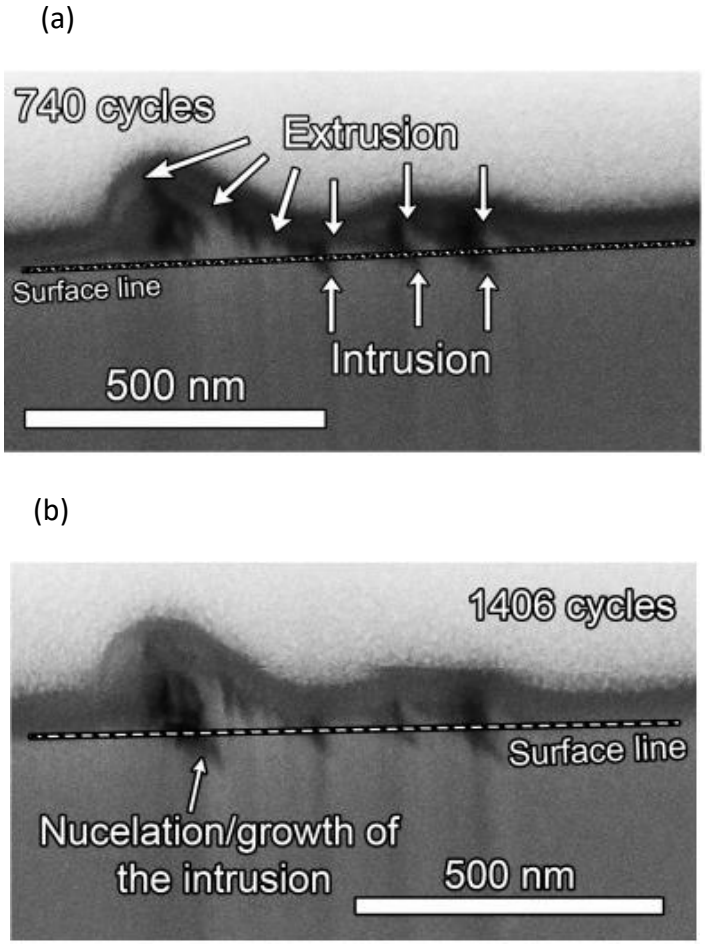

Fig. 44. The detail of the area No. 1 from Fig. 43b at different stages of the fatigue life; (a) detail of the PSM after N = 740 cycles; (b) nucleation of the intrusion on the left side of the PSM at N = 1406 cycles.

Higher magnification of the profile of the PSM developed in the first area is shown in Fig. 44. Three shallow intrusions along with the six tiny extrusions can be distinguished after 740 cycles. The straight surface line demonstrates no difference in height of the surface on the both sides of PSM. The further cycling up to 1406 cycles (see Fig. 44b) resulted only in very negligible evolution of the profile except the nucleation of the intrusion on the left side of the PSM. Even though the specimen was cyclically strained additionally, no crack initiation was observed before 2000 cycles.

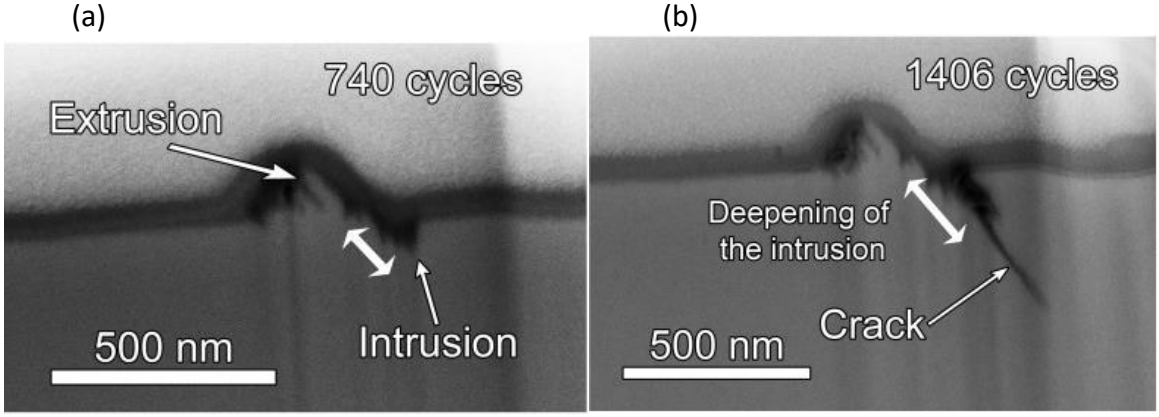

Fig. 45. The detail of the area No. 2 from Fig. 43b in different stages of the fatigue life; a) profile of the PSM after N *= 740 cycles; b) deepening of the intrusion followed by crack initiation at* N *= 1406 cycles.*

Fig. 45 shows the enlarged area of the second rectangle. Comparing to the PSM developed in the first location, the width of the PSM in this area is rather smaller. Cyclic loading after 740 cycles resulted in formation of pronounced broad intrusion accompanied by large extrusion to the left (see Fig. 45a). Significant change in the PSM profile was observed after 1406 cycles (see Fig. 45b). While the extrusion remained almost unchanged, further deepening of the intrusion followed till crack initiated from the tip of an intrusion. The crack can be well distinguished from the intrusion by its distinctive geometry.

The third location

In the last location only one PSM developed is presented. The image reveals the presence of the individual PSM after 740 cycles, see Fig. 46. Noticeable intrusion accompanied by the extrusion on the right side of the PSM can be recognized in Fig. 46b.

The detailed shape of the PSM profile is presented in Fig. 47. Higher magnification in Fig. 47a reveals the actual PSM consisting of the broad extrusion along with deep intrusion on the left side. The tendency of branching or possible crack initiation can be observed. In the case of cyclic loading after 1406 cycles, significant changes in PSM profile can be found. Narrow intrusion was formed on the right side of the extrusion. Moreover, the stage I crack was initiated from the tip of the formerly developed intrusion and started to grow. Additional 444 cycles (Fig. 47c) resulted in the substantial crack growth parallel to the primary slip plane. Newly developed intrusion did not develop any further.

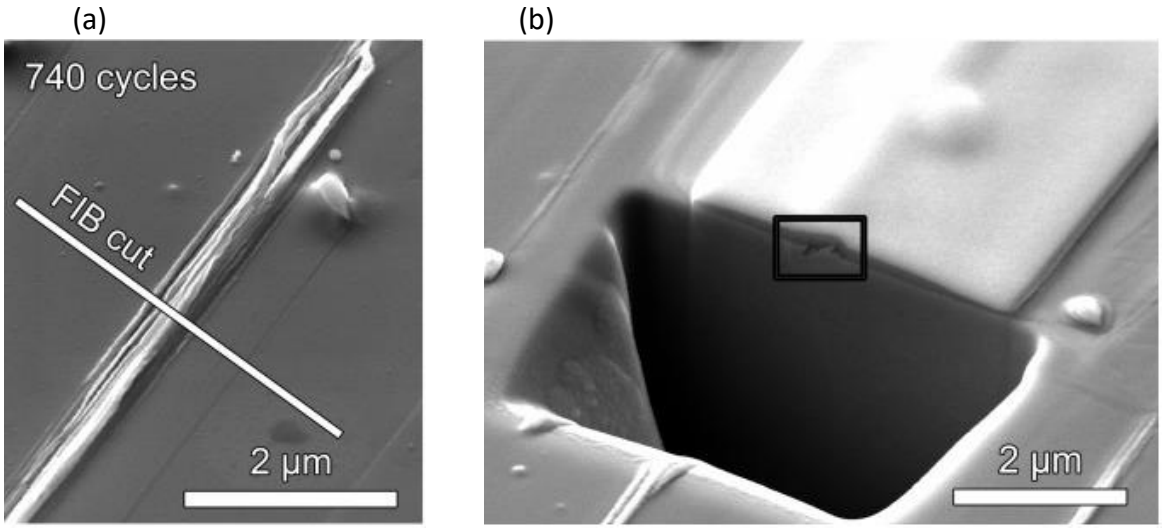

Fig. 46. Specimen surface at N = 740 cycles; (a) overall view of PSM; (b) platinum coating and rectangular crater produced by FIB.

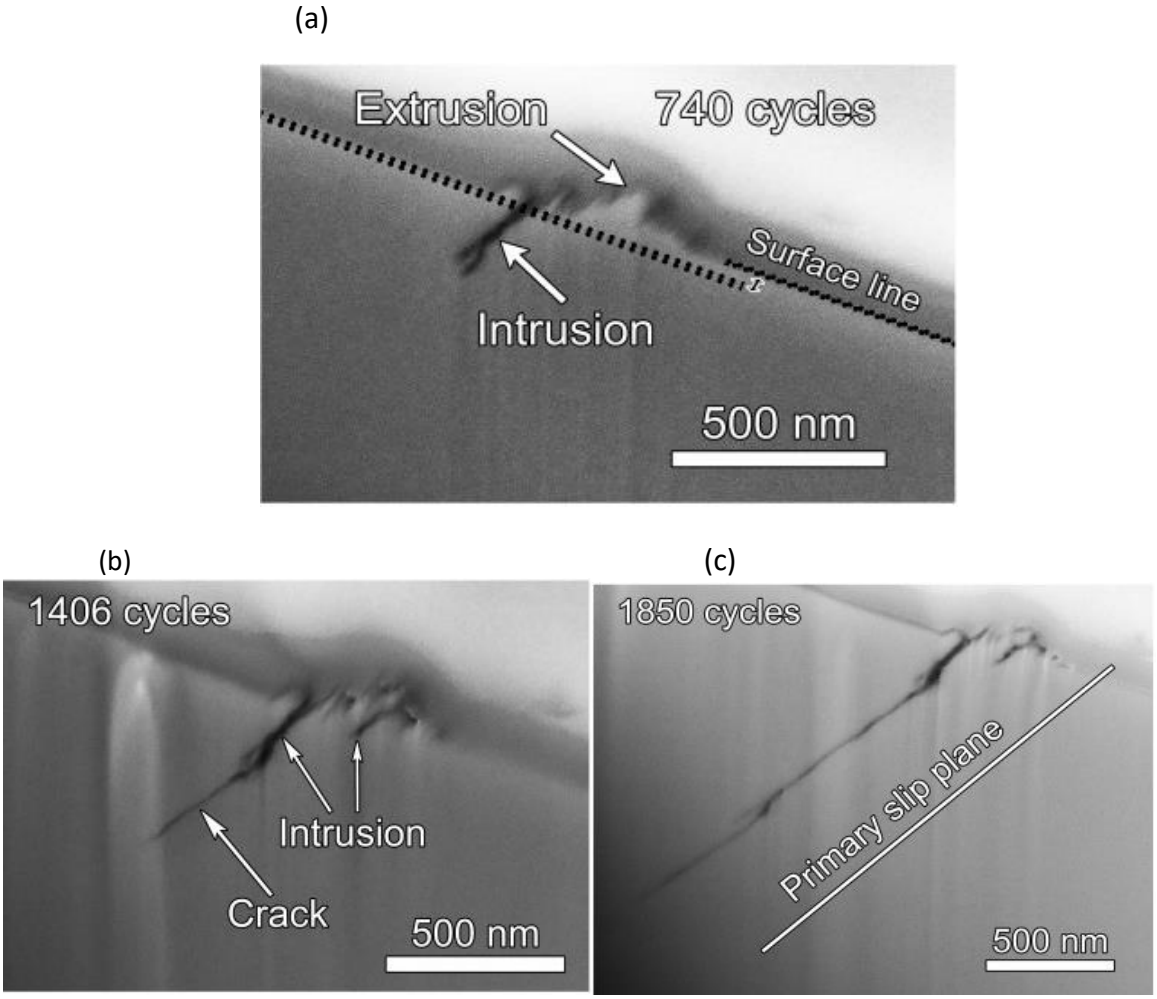

Fig. 47. The detail of the area denoted by rectangle in Fig. 46b at different stages of the fatigue life. a) N = 740 cycles, crack started to initiate from the intrusion; b) crack already initiated at N = 1406 cycles; c) growth of the fatigue crack along the primary slip plane at N = 1850 cycles.

5.2.5 Chapter highlights

- Cyclic softening is typical for room temperature cyclic loading.
- The statistical analysis brought out the formation of the two peaks in the distribution function. The shift of the probability density function to the lower fictive stresses indicates the cyclic softening.
- The deepening of the intrusion represents the crack-nucleation site and leads to crack initiation usually from the tip of the deepest intrusion during additional cyclic loading.

5.3 Isothermal fatigue loading at 700 °C

5.3.1 Cyclic hardening/softening curves

The material response to the low cycle fatigue straining at 700 °C is demonstrated in Fig. 48. Stress amplitudes plotted vs. the number of the loading cycles along with plastic strain amplitudes plotted vs. number of the loading cycle are shown in Fig. 48a and Fig. 48b respectively. Cyclic hardening from the onset of the loading is common for all total strain amplitudes applied. However, distinct character of the stress amplitude evolution during cyclic loading can be observed. The low strain amplitude cycling tends to harden rather gradually in the beginning of the cycling followed by relatively rapid increase of the stress amplitude with a tendency to saturation (this holds true for total strain amplitudes 2×10^{-3} and 2.5×10^{-3}). Rather steep onset of the stress amplitude relative to the number of the cycles can be recognized for higher total strain amplitudes. The trend of saturation in the end of the fatigue life is obvious for all cyclic tests regardless of the total strain amplitude implemented. Evolution of the plastic strain amplitude corresponds to development of the stress amplitude during loading and reflects the cyclic hardening with the tendency to saturation, see Fig. 48b.

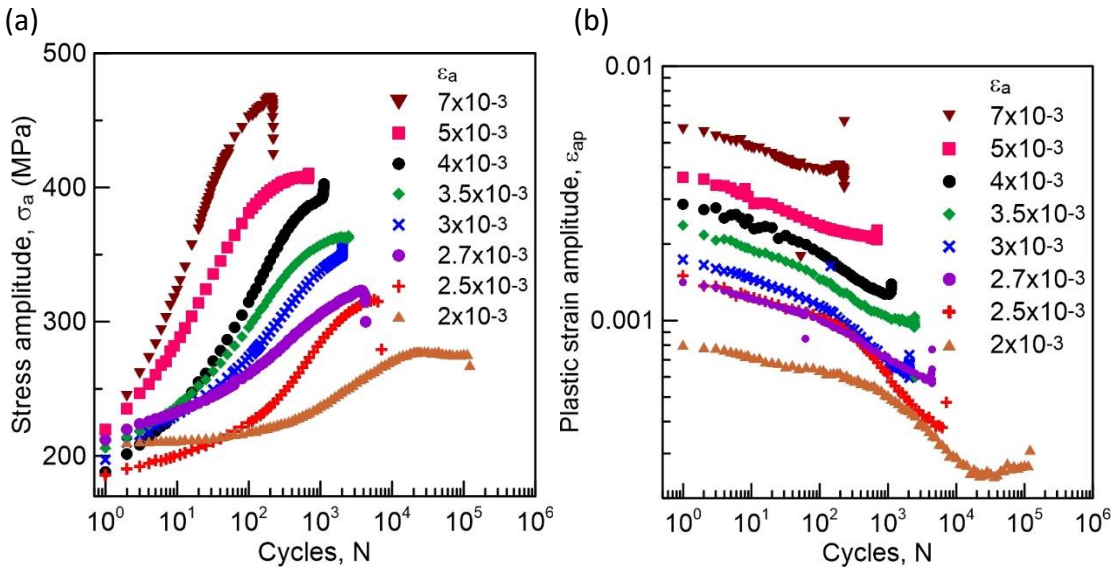

Fig. 48. Cyclic hardening/softening curves in constant total strain amplitude loading at temperature 700 °C, (a) stress amplitude vs. number of cycles, (b) plastic strain amplitude vs. number of cycles.

5.3.2 Statistical analysis of the hysteresis loop

The analysis of the hysteresis loop was performed in order to clarify the mechanism of the cyclic plastic evolution during low cycle fatigue loading at 700 °C. Accordingly, the second derivatives of the tensile and compressive segments were evaluated. Fig. 49 and Fig. 50. document the evolution of the second derivative of the hysteresis half-loop multiplied by $-2/\left(E_{eff}\right)^2$ plotted vs. the fictive stress $\varepsilon_r E_{eff}/2$. The convention to be considered; the tensile and compressive half-loops are labelled as segments (sgm), while all even segments represent tensile segments and all odd segments are compressive segments.

The evolution of the second derivative of the tensile and compressive segments in cycling with low total strain amplitude is documented in Fig. 49a and Fig. 49b, respectively. Pronounced large single peak centred at the fictive stress 130 MPa is a typical feature representing the second derivative in the beginning of the cycling. Additional cycling changes the character of the distribution function. The original peak diminished and got shifted to the higher fictive stresses while the second peak centred at 280 MPa turned out (see sgm 998). Eventually, only one extensive peak centred at 320 MPa containing wide scale of the fictive stresses was obtained. The analysis of the compressive segments yielded the same result.

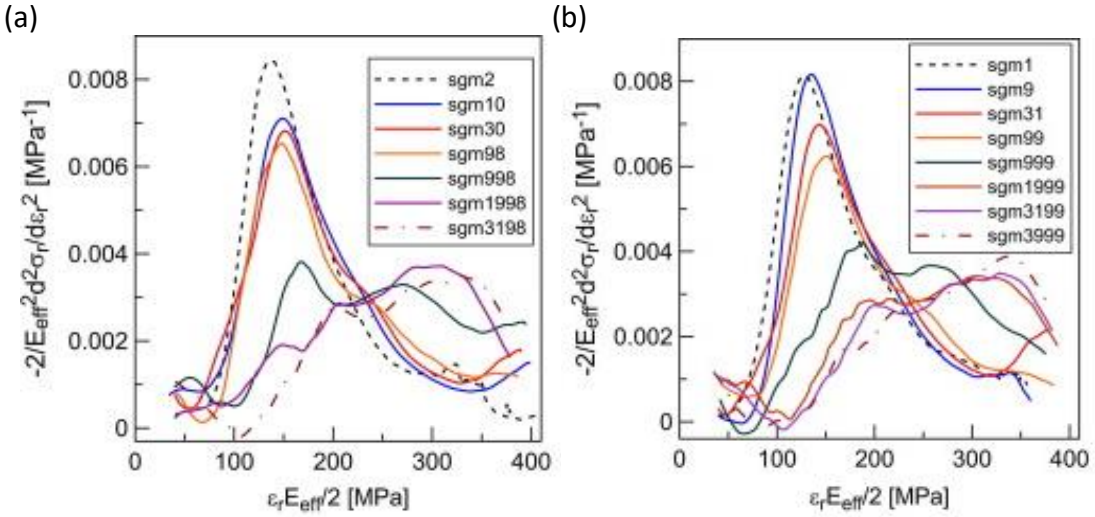

Fig. 49. Evolution of the second derivative of the tensile and compression segments in cycling with strain amplitude $\varepsilon_a = 2.5 \times 10^{-3}$ at temperature 700 °C during the fatigue life (a) tensile half-loops (segments), (b) compression half-loops (segments).

The probability density function during high temperature cyclic loading with high strain amplitudes (see Fig. 50) developed similarly to the probability density function during high temperature cyclic loading with low strain amplitudes. The trend of single peak formation can be recognized as well. Initially significant peak centred at 140 MPa diminished and later got shifted to the higher fictive stresses. However, the process of the broadening is much smoother in cycling with high strain amplitude (see sgm 2, 10, 30, 98), while in cycling with low strain amplitude the transition to the higher fictive stresses is not that pronounced. This situation is in full agreement with the evolution of the cyclic softening/hardening curves, where cyclic hardening is far more rapid for higher total strain amplitudes compared to lower

ones, see Fig. 48a. Finally, the second derivative is characterized by single broad peak centred at 340 MPa in the end of the fatigue life. The second derivatives of tensile and compressive segments are in good agreement and correspond to cyclic hardening.

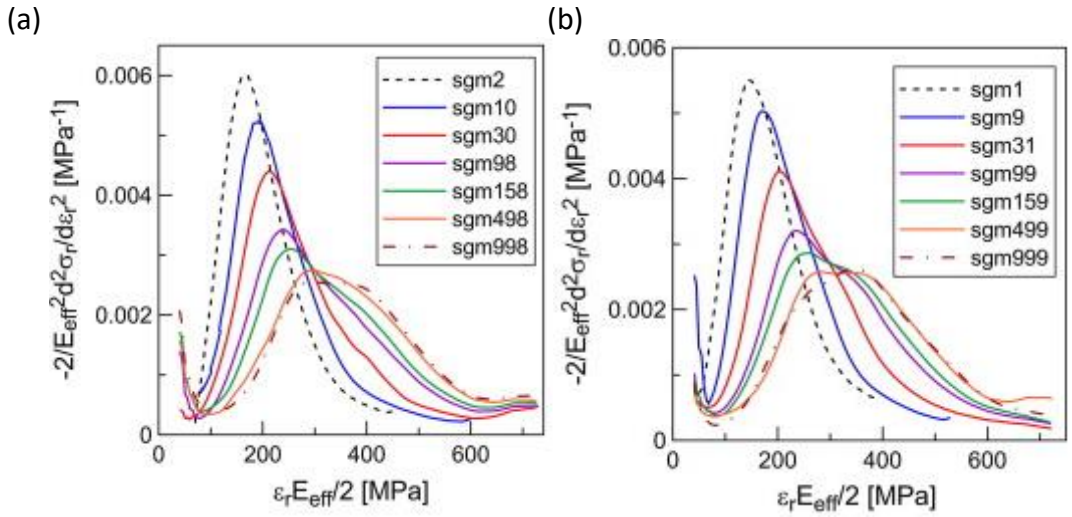

Fig. 50. Evolution of the second derivative of the tensile and compression segments in cycling with strain amplitude $\varepsilon_a = 5 \times 10^{-3}$ at temperature 700 °C during the fatigue life (a) tensile half-loops (segments), (b) compression half-loops (segments).

5.3.3 Surface relief observation

The inspection of the surface relief was carried out on the specimens at the end of the fatigue life. Since the study of the secondary cracks is fundamental for fatigue damage estimation, the crack formation along with the study of crack path was the subject of this investigation.

SEM observation of the specimen surface subjected to cyclic loading at 700 °C revealed the formation of the oxide layer and nucleation of numerous fatigue cracks. The common aspect for cyclic straining at 700 °C is the formation of the thin oxide layer developed within the grains and the pronounced oxide extrusions developed at some grain boundaries. Fig. 51 shows the surface of the specimen strained with total strain amplitude $\varepsilon_a = 4 \times 10^{-3}$ at the end of the fatigue life. The oxidic extrusion marked by rectangle formed at the oxidized grain boundary is cracked. The respective inset represents the higher magnification of the marked area. Study of the large area of the specimen surface revealed that only the grain boundaries arranged approximately perpendicular in relation to stress axis are significantly oxidized and cracked.

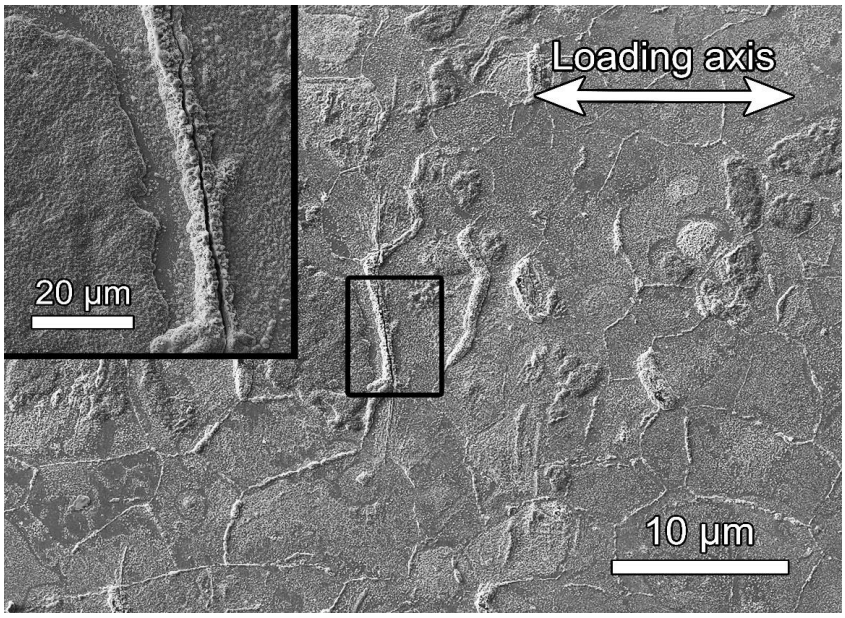

Fig. 51. Surface of the specimen cyclically strained under IF loading conditions at 700 °C with strain amplitude $\varepsilon_a = 4 \times 10^{-3}$. The inset shows the detail of oxidized and cracked grain boundary perpendicular to the loading axis.

5.3.4 FIB cutting

The study of the in-depth profiles of the secondary cracks was conducted by means of SEM equipped with FIB technique. The oxidized thick oxide layer developed at the grain boundary is shown in Fig. 52a. FIB trench was produced at the location previously denoted as FIB cut line in Fig. 52a.

(a) (b)

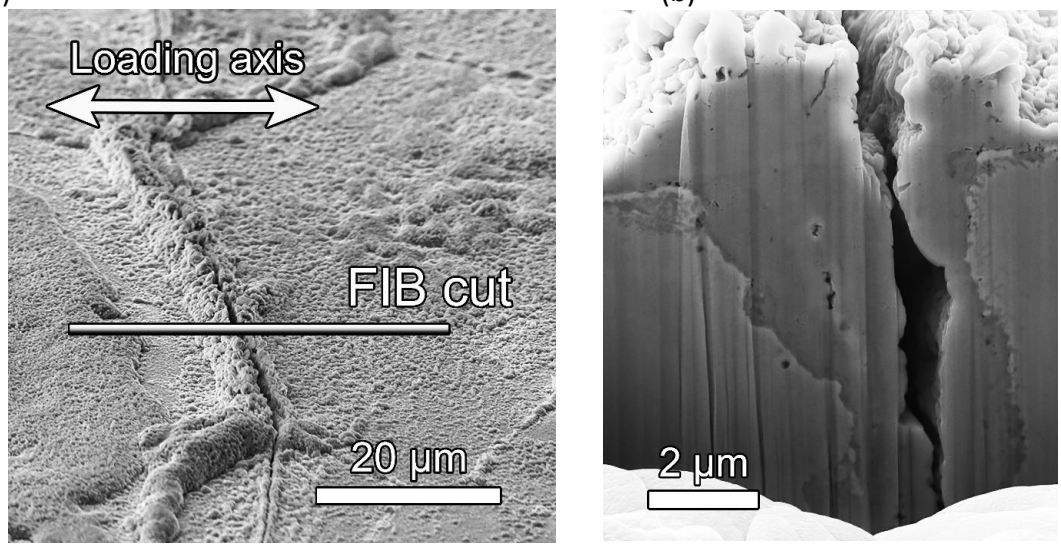

Fig. 52. Cracked grain boundary after IF loading with $\varepsilon_a = 4 \times 10^{-3}$; (a) enhanced oxidation and cracking of the grain boundary perpendicular to stress axis. The line denotes the location where the FIB cut was produced; (b) FIB cut showing the cracked oxide along the grain boundary.

The profile of the oxidized grain boundary with oxide extrusion and oxide intrusion shows Fig. 52b. This profile documents that grain boundary is massively oxidized and the oxide extrusion as well as oxide intrusion are cracked. The oxide layer formation and subsequent cracking of the grain boundary lead to early microcrack nucleation and in accelerated crack growth driven by tensile stress during cyclic loading.

5.3.5 Longitudinal cross section inspection

Additionally, to the specimen surface investigation the damage development in the interior of the specimen was studied. In order to clarify the internal damage, the longitudinal cuts of the specimen's gauge length parallel to the stress axis were produced. Once manufactured, the polished surface was exposed to the investigation using advanced SEM techniques. Moreover, the EBSD technique was adopted to identify the cracks paths.

Fig. 53 shows two large cracks located approximately in the middle of the longitudinal cut. They initiated from the specimen surface and propagated into the material matrix almost perpendicularly to the stress axis. The longitudinal cut was subjected to detailed SEM observation revealing no sign of internal damage in form of cavity or possible internal crack formation.

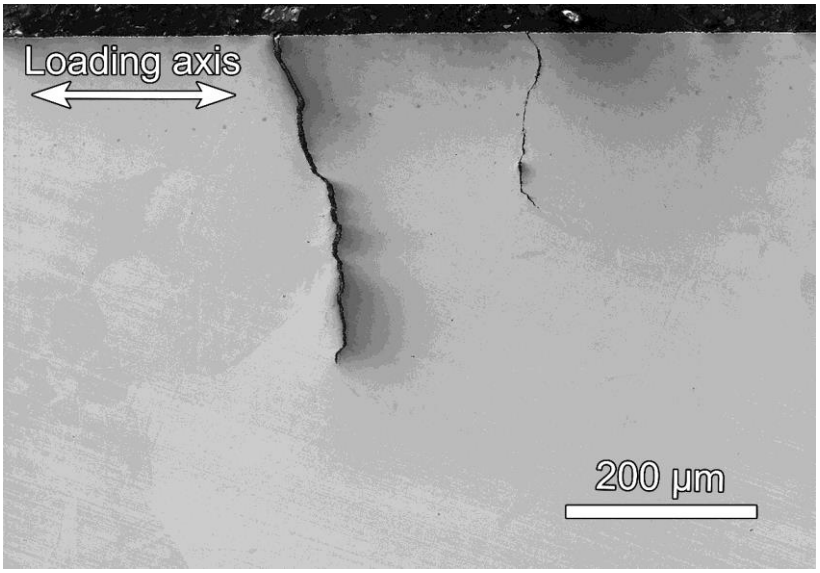

Fig. 53. Longitudinal cross section of specimen gauge length subjected to IF loading conditions with $\varepsilon_a = 4 \times 10^{-3}$ showing surface crack development.

Fig. 54 shows another crack growing perpendicular to the stress axis simultaneously with EBSD image of the respective area. EBSD image reveals that the crack developed from the specimen surface propagates transgrannulary. Based on the prior surface observation it can be stated that crack in Fig. 54b is well developed and the particular location in the perpendicular cut does not need to be the location on the surface from where the crack had been initiated.

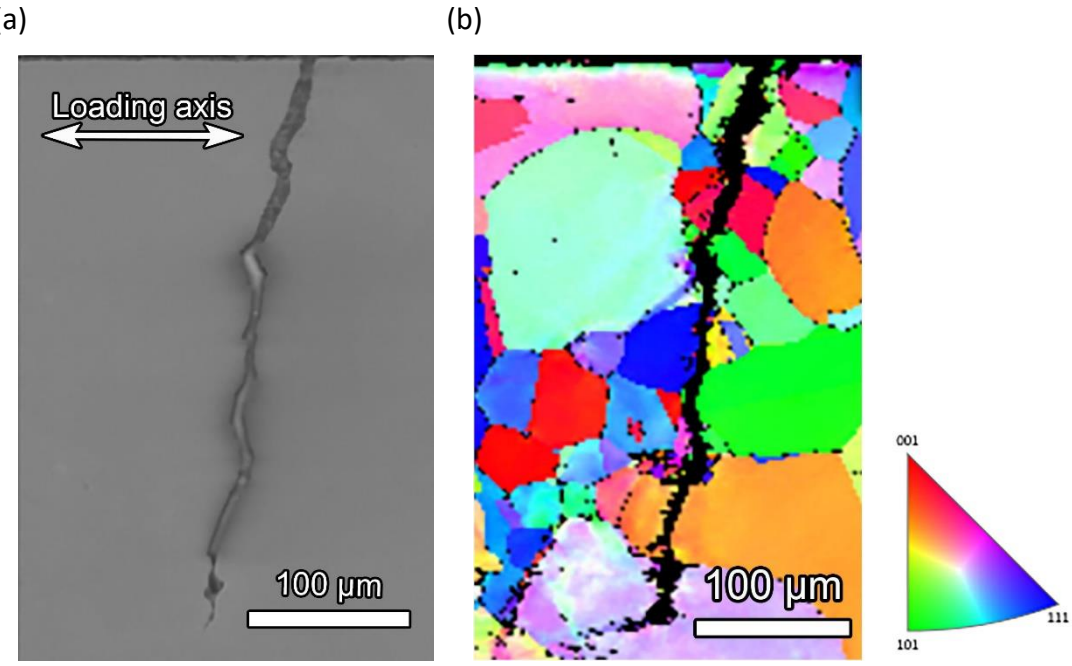

Fig. 54. Longitudinal section of the specimen subjected to IF cycling with $\varepsilon_a = 4 \times 10^{-3}$ showing surface crack, (a) SEM image, (b) EBSD image.

5.3.6 Chapter highlights

- Cyclic hardening is common for all total strain amplitudes applied.
- The initial peak of the probability density function tends to shift from the lower fictive stresses to the higher values and gets broaden during cyclic straining.
- The pronounced oxide layer formation especially at the grain boundaries plays decisive role in the crack initiation during the material exposure to cyclic loading at 700 °C in the air.

5.4 Isothermal fatigue loading at 700 °C with dwell in the loading cycle

5.4.1 Cyclic hardening/softening curves

The evolution of the stress amplitude under high temperature low cycle fatigue conditions with a 10 minutes tensile dwell in the loading cycle is demonstrated in the Fig. 55. Various total strain amplitudes were applied to individual specimen at constant strain rate 2 $\times 10^{-3}$ s^{-1}. The stress amplitude plotted vs. the number of the loading cycles and the plastic strain amplitude vs. the number of the loading cycles is documented in Fig. 55a and Fig. 55b, respectively. Cycling with all strain amplitudes leads to accelerated cyclic hardening from the onset of the straining. There is a tendency to reach saturation, however the premature fracture prevents reaching the pronounced stress saturation for the highest strain amplitude. The saturation character during straining along with a tendency to cyclic hardening can be

recognized in the case of the evolution of the plastic strain amplitude (Fig. 55b) for all total strain amplitude as well.

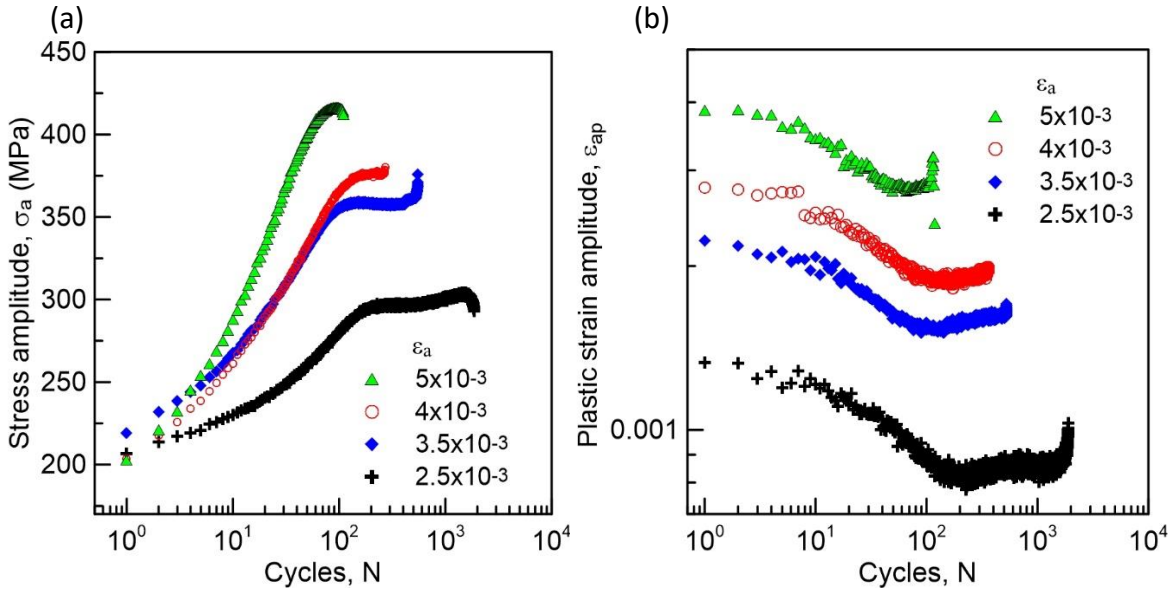

Fig. 55. Cyclic hardening/softening curves in isothermal fatigue loading at temperature 700 °C with 10 min tensile dwell. (a) stress amplitude vs. number of cycles, (b) plastic strain amplitude vs. number of cycles.

An additional parameter for LCF assessment in cycling with dwells has been followed. The evolution of the mean stress becomes significant when introducing the dwell into the loading cycle. Generally, mean stress does not change dramatically under symmetric cyclic loading ($R_\varepsilon = -1$) and remains rather stable around the zero stress.

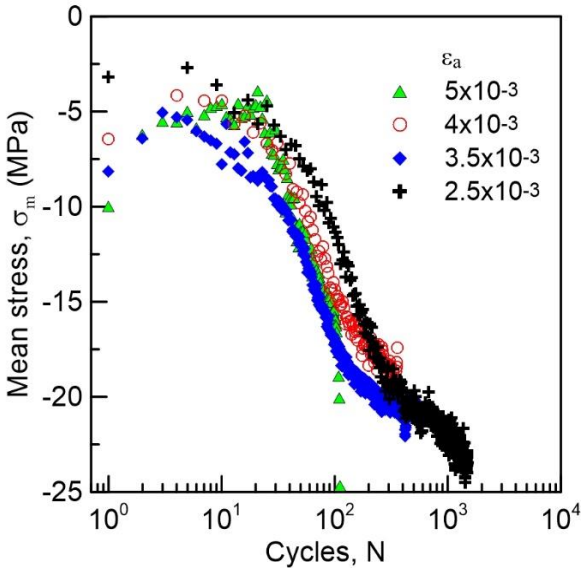

Fig. 56. Mean stress vs. number of cycles in isothermal fatigue loading at temperature 700 °C with 10 min tensile dwell.

In the case of IF-D tests the mean stress continually decreases during the fatigue life. Fig. 56 depicts the evolution of the mean stress vs. number of cycles. Mean stress rapidly decreases during cyclic loading for all total strain amplitudes. The most pronounced decrease of the mean stress was observed for $\varepsilon_a = 3.5 \times 10^{-3}$.

5.4.2 Surface relief observation

The surface fatigue cracks developed during isothermal straining with tensile dwell were studied at the end of the fatigue life by means of SEM. Since the secondary short cracks represent the early stages of the crack nucleation the detailed inspection allows identifying the mechanism of the crack initiation and estimation of the damage mechanism.

The investigation of the surface relief of the specimen subjected to IF-D procedure disclosed extensive formation of the oxide layer and nucleation of several fatigue cracks. Fig. 57 is representative image of the specimen surface relief evolved during loading showing three mechanisms involved in terms of the fatigue crack initiation. Oxidized grain boundaries can be recognized along with a homogeneous thick oxide layer developed within the grains. The cracks initiated on the uniform oxide layer grow transgranularly and perpendicularly to the stress axis. In addition to transgranular cracks, intergranular crack formation in the form of cracking of the oxidized grain boundaries as well as grain boundary sliding and associated formation of the wedge crack were documented.

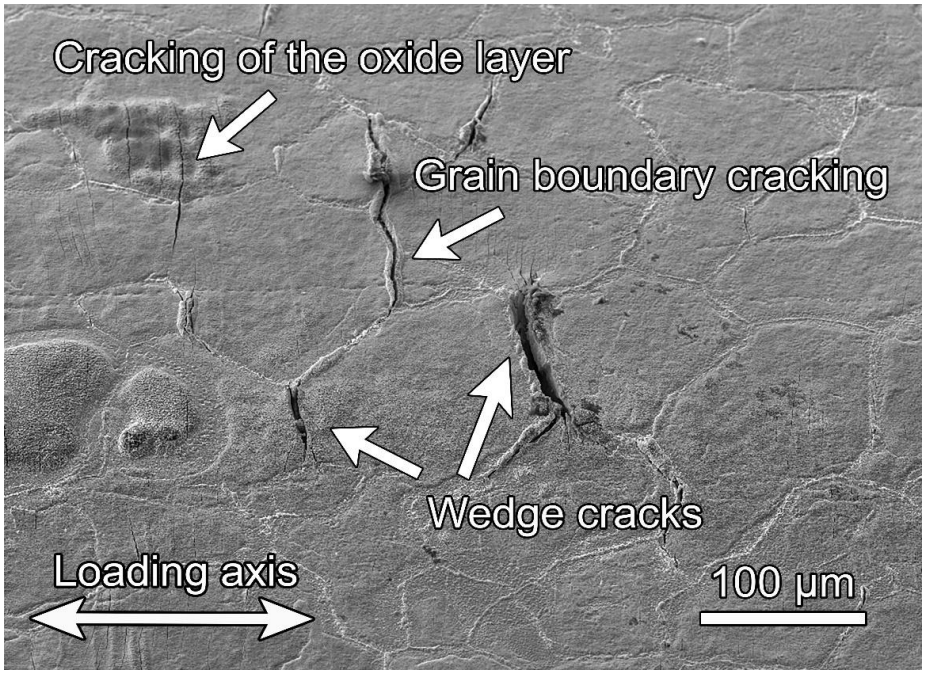

Fig. 57. Surface of the specimen cyclically strained under IF-D loading conditions with strain amplitude $\varepsilon_a = 4 \times 10^{-3}$. The arrows show different types of crack formation: grain boundary cracking, wedge cracks and cracking of the uniform surface oxide layer.

5.4.3 FIB cutting

SEM equipped with FIB was adopted to identify and to determine the mechanism of crack formation from the in-depth profiles of the secondary surface cracks. Heavily oxidized and cracked grain boundary is depicted in Fig. 58. The FIB trench produced on the location marked as FIB cut revealed the cracking of the oxidized grain boundary arranged perpendicularly to the loading axis.

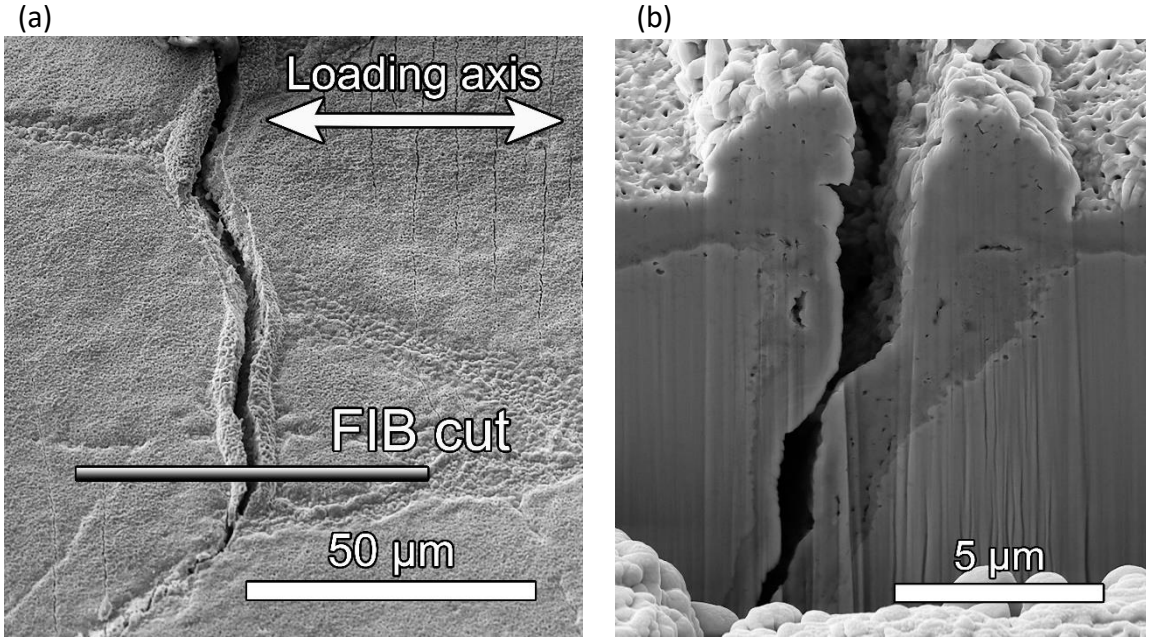

Fig. 58. Cracked grain boundary after IF-D cycling with $\varepsilon_a = 4 \times 10^{-3}$; (a) heavily oxidized and cracked grain boundary, (b) FIB cut showing oxidized grain boundary crack.

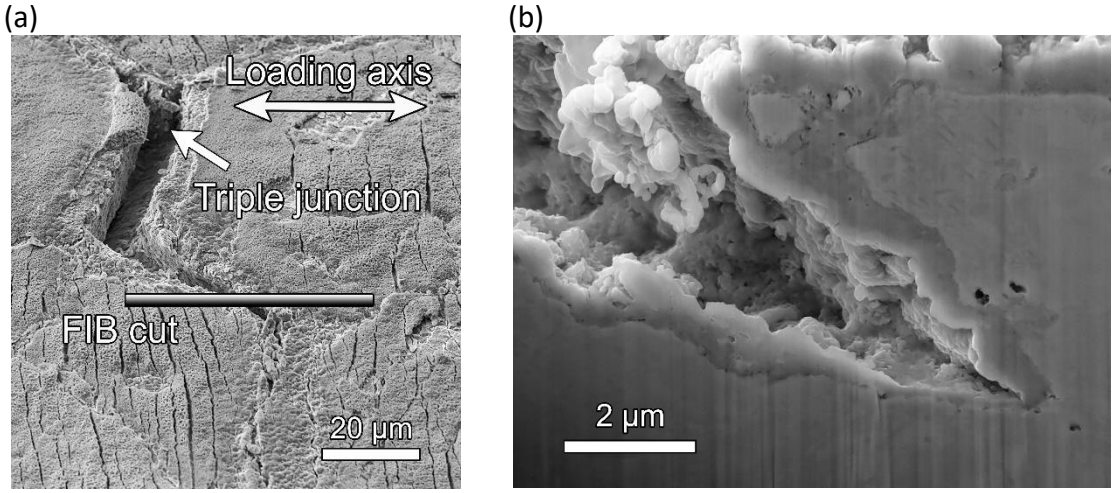

Fig. 59. Wedge crack developed after IF-D cycling with $\varepsilon_a = 4 \times 10^{-3}$; (a) grain boundary sliding leading to the wedge crack formation on the material surface, (b) FIB cut revealing its in-depth profile.

In addition to the cracking of the oxidized grain boundaries the wedge cracks were commonly observed. Fig. 59 shows the microcrack generally accepted as a wedge crack formed due to

grain boundary sliding to accommodate the change in the shape of elongated grains. The in-depth profile of the wedge crack at the location marked as FIB cut is given in Fig. 59b. It shows the wedge crack proceeding in the interior of the material at inclined angle. The crack is broadly open and decorated by rather thin oxide layer developed on its perimeter.

Besides the intergranular crack formation, the transgranular secondary fatigue cracks were observed as well. The third kind of crack nucleation was the initiation of the crack from the uniform oxide layer. Fig. 60a shows cracked homogeneous thick oxide layer within the grain. Fig. 60b demonstrates the respective in-depth profile of the location marked as FIB cut. Once the uniform oxide layer is cracked, the fresh metal surface is exposed to the oxygen present in environment and subsequently new oxide layer is formed. Gradual alternation of the oxide cracking followed by oxide layer formation in this location lead to the development of the V-shaped groove in the material volume. The propagation of the environmentally related crack is promoted by cyclic loading.

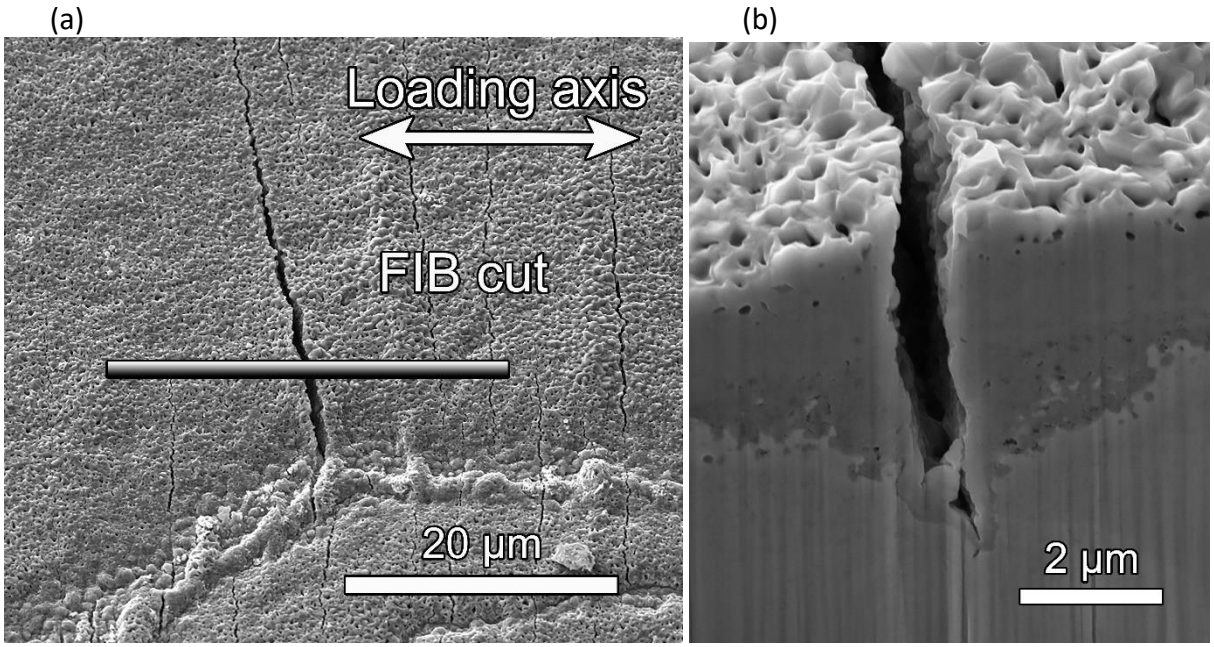

Fig. 60. Cracking of the uniform oxide layer after IF-D cycling with $\varepsilon_a = 4 \times 10^{-3}$; (a) short secondary crack developed in the oxide layer, (b) FIB cut showing localized oxidation in V-shape groove.

5.4.4 Longitudinal cross section inspection

The investigation of the crack formation of the specimen at the end of the fatigue life subjected to IF-D procedure revealed the mechanisms of the crack initiation from the specimen surface. In order to estimate the internal damage in material volume, the longitudinal cross-sections from the specimen gauge length were produced. The surface of the longitudinal cross-section was polished and studied by means of SEM, EBSD and EDS to reveal the internal damage, cracks paths and the chemical composition of the oxide layer developed.

Generally accepted concept of fatigue and creep interaction in terms of the damage development includes the coupling of the fatigue crack developed from the specimen surface and the internal intergranular damage commonly referred to as creep damage in the material volume. The situation in the interior of the material along with the inset of the well-developed crack from the specimen surface is documented in Fig. 61. Multiple secondary short cracks nucleated from the specimen surface (outer cracks) can be easily recognized from the inset. The internal damage in the form of internal cracks was discovered mostly in the neighbourhood of the dominant outer crack almost in the middle of the specimen. Once the dominant fatigue crack encounters the internal cracks the rapid increase of the fatigue crack growth follows.

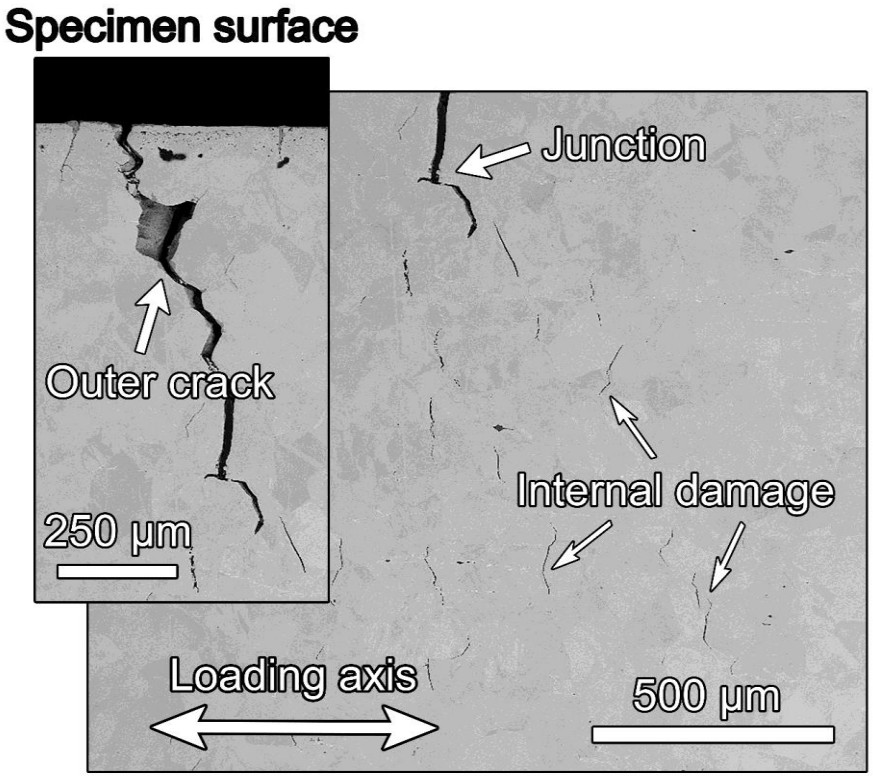

Fig. 61. Longitudinal cross-section of specimen gauge length subjected to IF-D cycling with $\varepsilon_a = 4 \times 10^{-3}$ showing internal damage development.

The extensive area of the longitudinal cross-section was inspected under high magnification by means of SEM. The scrutiny revealed the cavities dispersed mostly on the grain boundaries, see Fig. 62. The variability in the shape of the cavities is depicted in the inset image of the marked rectangle under higher magnification. The image captures the coalescence of the cavities in location of triple joint of the adjacent grains.

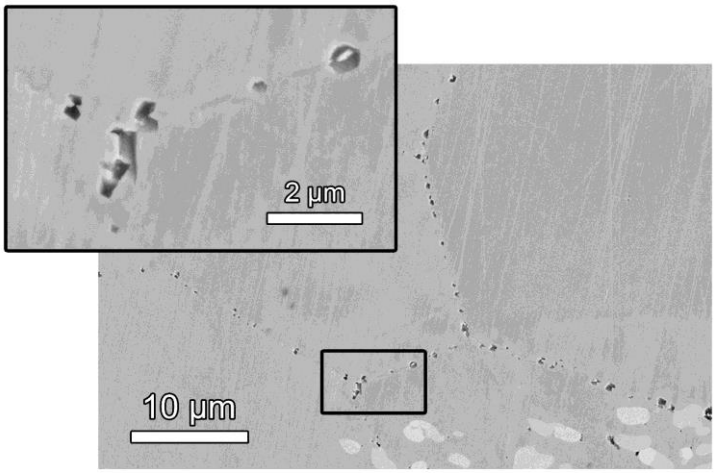

Fig. 62. SEM image of a longitudinal cross section; small cavities developed preferentially at the grain boundaries. The close up shows cavities located at the triple point of grain boundary junction.

Besides the cavities formed at the grain boundaries, the population of fine, mostly circular voids can be recognized in the interface of the coarse particles of the Z-phase complex nitrides and the matrix, see Fig. 63.

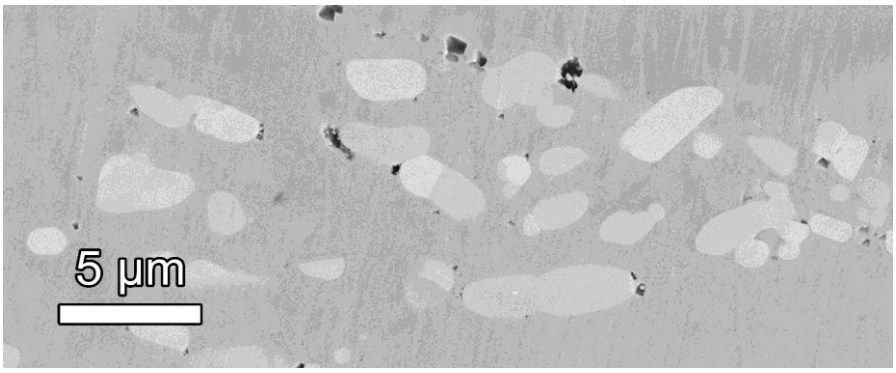

Fig. 63. Cavities developed at the nitride/matrix interface.

Additional cyclic loading with tensile dwell revealed not only formation of the cavities distributed at the grain boundaries but also gradual growth of the cavities and their coalescence. The evolution of the internal intergranular damage is documented in Fig. 64. The internal cracks formed at the grain boundaries are the result of the cavities linkage during cyclic straining. The early nucleation of the cavities and their subsequent coalescence stands for the early stage of internal crack formation.

(a) (b)

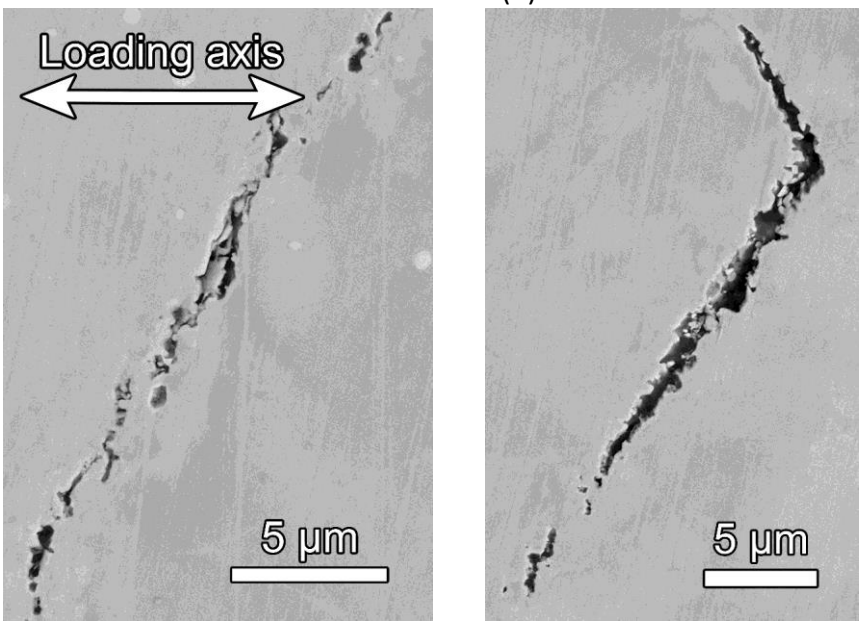

Fig. 64. Cavity coalescence under IF-D loading conditions. Cycling with $\varepsilon_a = 4 \times 10^{-3}$ and 10 min tensile dwell; (a) the cavities distributed along the grain boundary; (b) linkage of the cavities leading to early grain boundary crack formation.

In order to identify the crack paths developed under isothermal fatigue loading with dwells the longitudinal cuts were subjected to EBSD technique. The SEM image of the dominant crack initiated from the specimen surface encountering the internal crack is shown in Fig. 65a. The corresponding EBSD image is shown in Fig. 65b. Based on the EBSD image it can be stated that the dominant crack propagated both transgranularly and intergranurarly, nonetheless, the major fraction of the crack growth is intergranular.

(a) (b)

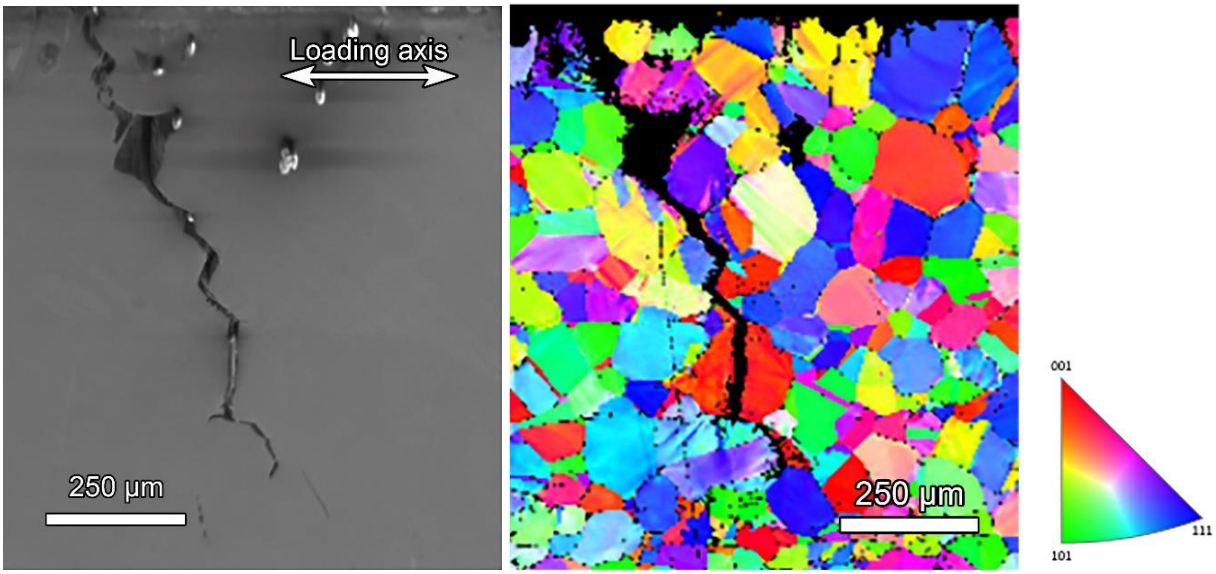

Fig. 65. Longitudinal cross-section of the specimen subjected to IF-D procedure showing surface crack, (a) SEM image, (b) EBSD image.

The SEM image of the internal crack on the longitudinal cross-section is shown in Fig. 66. The respective image obtained by means of EBSD confirms the previous indication that the internal cracks are developed at the grain boundaries. The upper part of the well-developed crack propagates in transgranular manner and could be driven by the cyclic stress applied.

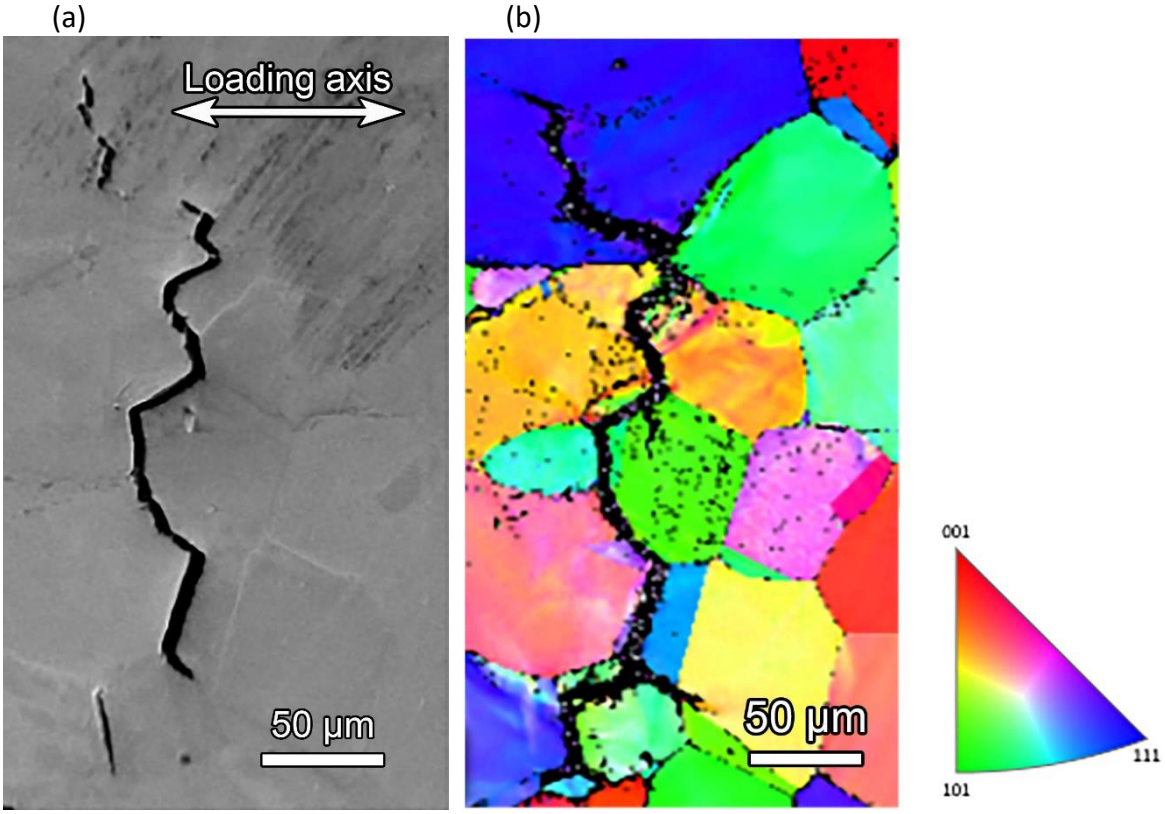

Fig. 66. Longitudinal section of the specimen subjected to IF-D procedure showing internal crack, (a) SEM image, (b) EBSD image.

The investigation of the surface relief developed at the end of the fatigue life revealed the formation of the oxide layer. In addition, the in-depth profiles of the oxidized grain boundaries disclosed the cracking of the oxidized grain boundaries and further oxide intrusion formation in the direction of proceeding crack in the material volume. The EDS analysis was adopted to study the chemical composition of the oxide layer on the longitudinal cross-sections. The rectangle area shown in Fig. 67 was subjected to EDS analysis. EDS revealed the formation of an oxide layer structure consisting of Fe-rich outer oxide and Cr-rich inner oxide layer. The coloured images decorating the main picture document the distribution of oxygen, nickel, iron and chromium in oxide intrusion along with the surface oxide in close neighbourhood and material matrix. Fe-rich oxide dominates in the centre of the intrusion while the Cr-rich oxide forms the narrow interface between Fe-rich oxide and the matrix. The content of the Ni is distributed rather uniformly in the material matrix, however, significantly higher concentration was found on the oxide/matrix interface.

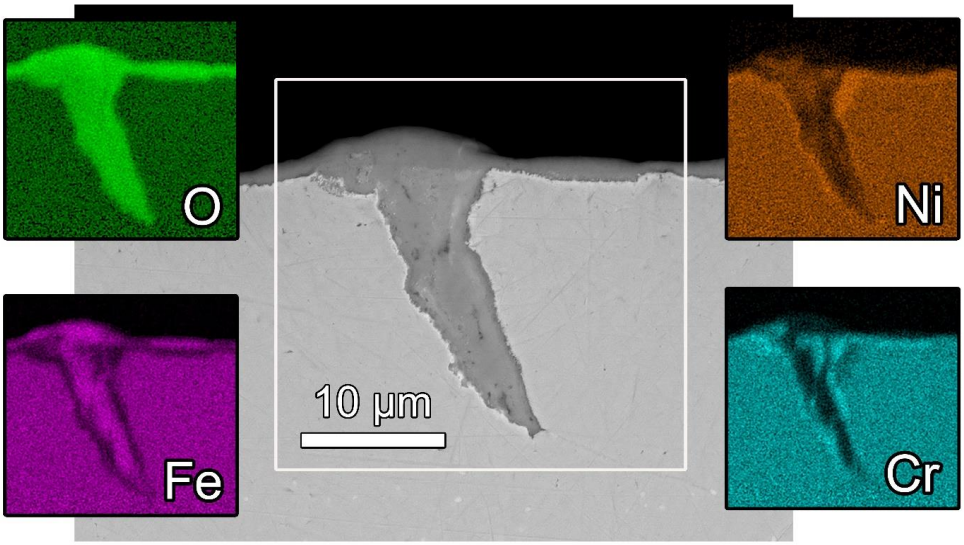

Fig. 67. Chemical composition of the surface oxide layer developed under IF-D loading conditions with $\varepsilon_a = 4 \times 10^{-3}$. EDS analysis of respective Fe, Cr, O, Ni content (vivid areas correspond to higher element concentration).

5.4.5 Chapter highlights

- Cyclic hardening is typical for all total strain amplitudes applied.
- Growth of the dominant crack developed from the specimen surface is promoted by the linkage with the internal cracks.

5.5 Thermomechanical fatigue

5.5.1 Cyclic hardening/softening curves

The material investigated was exposed to two distinctive loading tests; in-phase and out-of-phase thermomechanical cyclic loading. Cyclic hardening/softening curves for various total strain amplitudes implemented to individual specimens were evaluated. The plot of the stress amplitude vs. the number of cycles for IP-TMF as well as for OP-TMF is shown in Fig. 68a and Fig. 68b, respectively. Different loading conditions applied to the material resulted in similar fatigue response. Both testing procedures led to cyclic hardening and the increase of the total strain amplitude resulted in higher hardening rate. The tendency to the saturation of the stress amplitude is pronounced in OP-TMF loading regardless of the total strain amplitude applied. The shorter fatigue life in IP-TMF cyclic loading prevented reaching saturation.

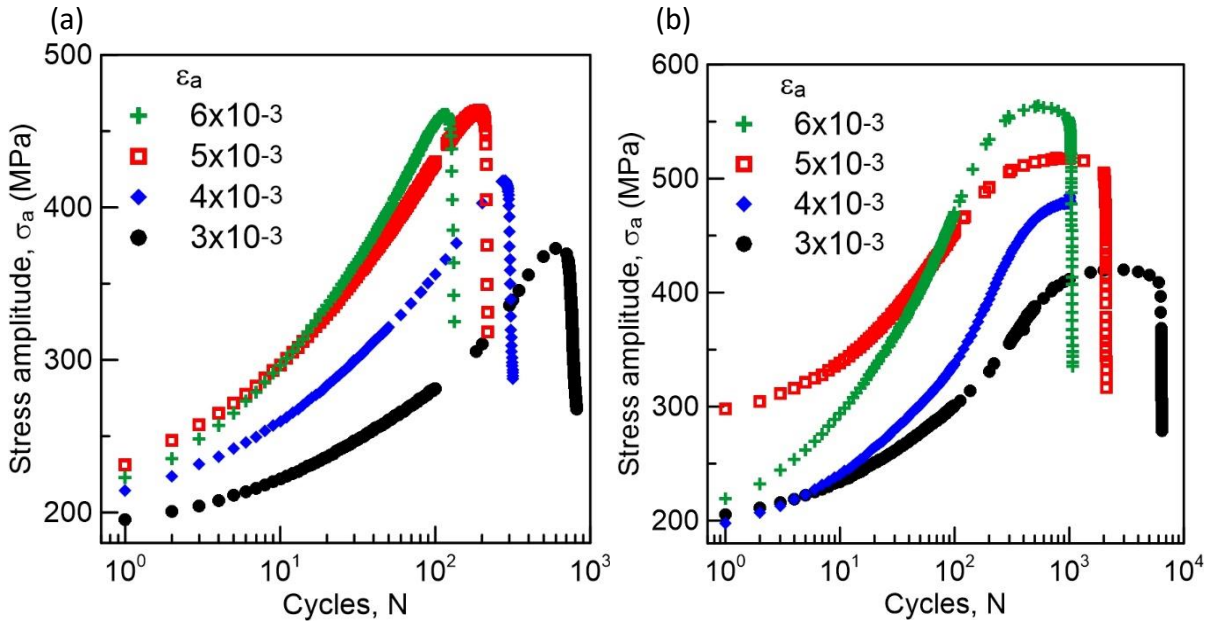

Fig. 68. Cyclic hardening/softening curves in TMF for all strain amplitudes; stress amplitude vs. number of cycles (a) in IP-TMF and (b) in OP-TMF cycling.

The evolution of the plastic strain amplitude during cyclic loading for both types of straining is depicted in Fig. 69. The typical attribute for all total strain amplitude is the decrease of the plastic strain amplitudes during the fatigue life for IP- and OP-TMF tests. The evolution of the plastic strain is in full correlation with the evolution of the stress amplitude in IP-TMF and in case of OP-TMF loading indicating fatigue hardening. Pronounced saturation region of the plastic strain amplitude is characteristic for OP-TMF cycling.

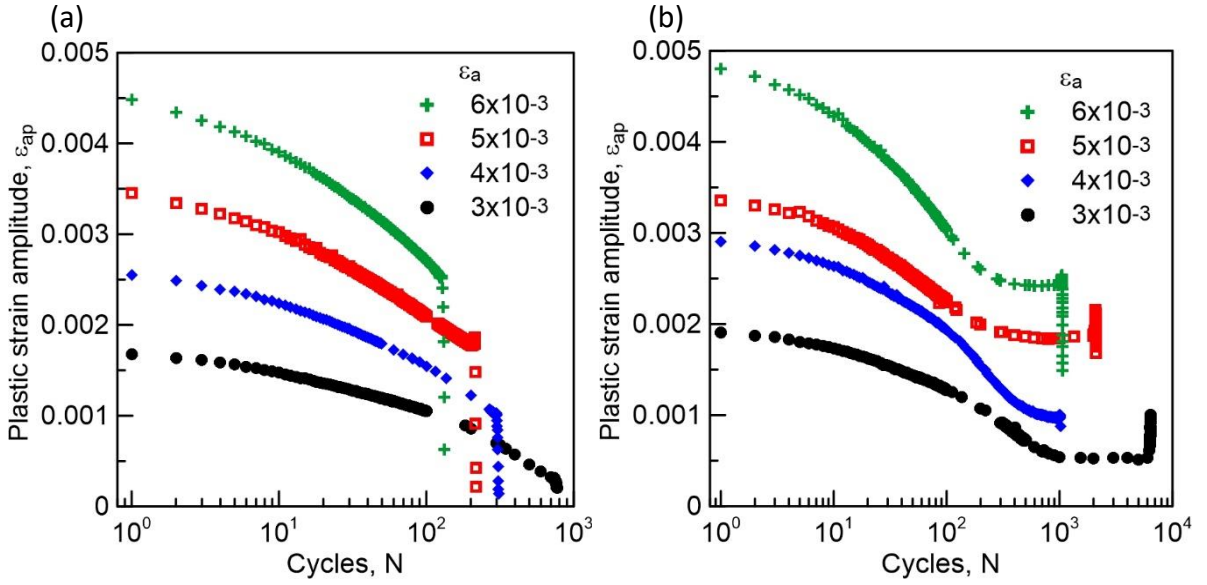

Fig. 69. Cyclic hardening/softening curves in TMF for all strain amplitudes; plastic strain amplitude vs. number of cycles in (a) IP-TMF and (b) in OP-TMF cycling.

Fig. 70 shows the plot of the mean stress during IP- and OP-TMF cycling. Negative mean stress is typical for all total strain amplitudes during IP-TMF cycling. The evolution of the mean stress

in the case of OP-TMF loading is overall opposite when compared to IP-TMF loading. The positive mean stress slightly decreases at the onset of the cycling but subsequently there is substantial increase of the mean stress after a few cycles. The drop of the mean stress in IP- and OP-TMF cycling at the end of the fatigue life is attributed to appearance of the principal fatigue crack. The change of the mean stress during cycling loading without the influence of the principal crack for both loading conditions can be assessed considering the evolution of the plastic strain amplitude. The real change of the mean stress during cycling can be estimated to only about 40 MPa for IP-TMF and 50 MPa for OP-TMF.

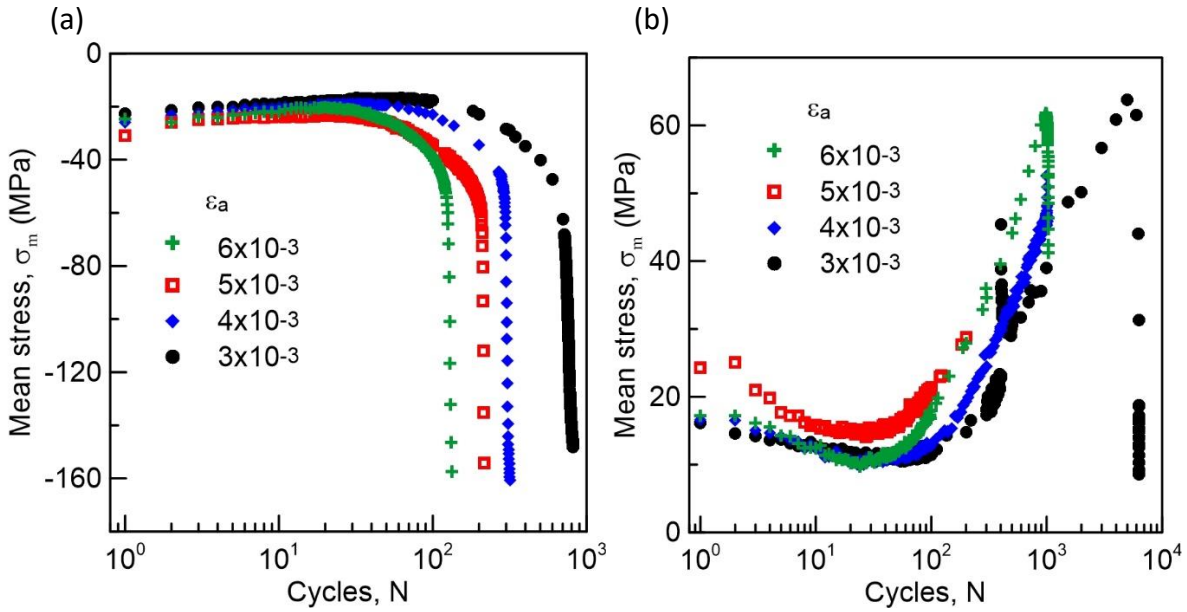

Fig. 70. Cyclic hardening/softening curves in TMF for all strain amplitudes; mean stress vs. number of cycles (a) in IP and (b) in OP cycling.

5.5.2 Surface relief observation

Thermomechanical fatigue loading resulted in nucleation of the multiple fatigue cracks on the specimen surface. The interaction of the adjacent cracks contributes to the formation of the dominant crack. The essential information can be acquired by the inspection of the secondary cracks initiated on the specimen surface. Accordingly, SEM equipped with FIB technique was adopted to identify the mechanism of the early crack formation.

The surface of the specimen cyclically strained under IP-TMF loading condition with total strain amplitude 3×10^{-3} is presented in Fig. 71a. The specimen surface is covered by the thin oxide layer. The thicker bands of oxide were predominantly developed at the grain boundaries oriented perpendicularly to the stress loading axis. Fig. 71b demonstrates higher magnification of the respective area from Fig. 71a. Fatigue cracks are formed practically exclusively at the grain boundaries. Moreover, the slip lines corresponding to the activation of primary slip system are noticeable in some favourably oriented grains.

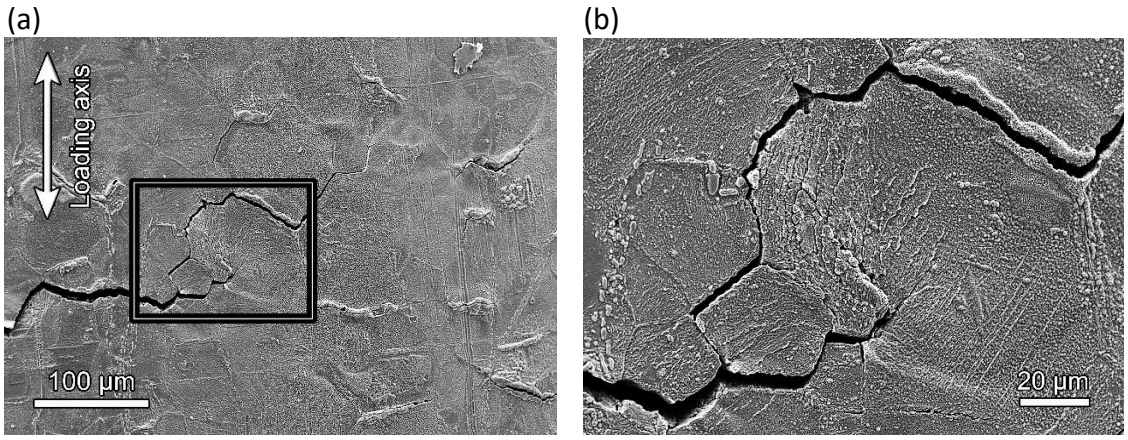

Fig. 71. Surface of the specimen cyclically strained in IP-TMF cycle with mechanical strain amplitude 3 × 10^{-3} to fracture (a) secondary cracks linking together (b) detail of the area denoted by a rectangle in (a) showing surface relief.

The surface observation of the specimens strained under OP-TMF loading conditions revealed a different mechanism of the crack formation. Fig. 72a demonstrates the formation of the thick homogeneous oxide layer within the grains. Several cracks developed on the oxide layer running transgranularly and perpendicularly with the respect to the loading axis can be recognized. Fig. 72b provides the higher magnification of the marked rectangle in Fig. 72a. The well-developed cracks nucleated by the cracking of the oxide layer can easily proceed to the material matrix. It can be noticed from the crack developed in the upper right corner of the image. The cracking of the oxidized grain boundaries turned out not to be crucial in this regard.

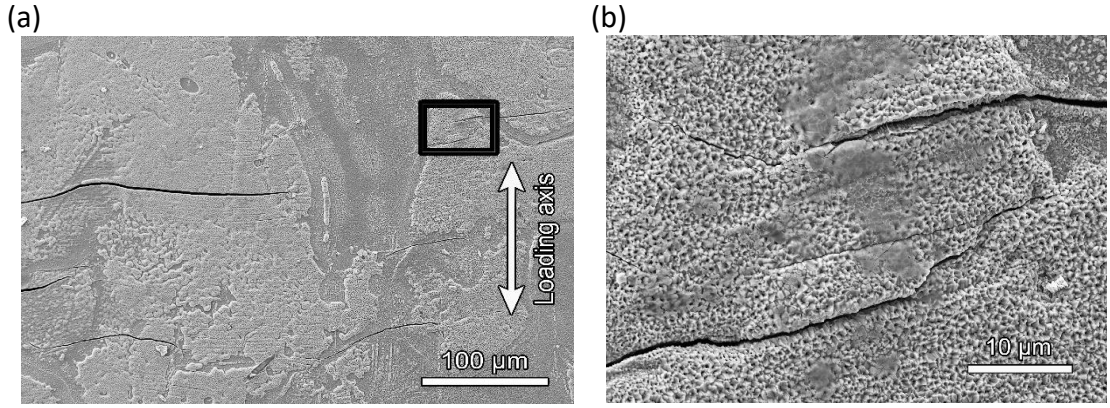

Fig. 72. Surface of the specimen cyclically strained in OP-TMF cycle with mechanical strain amplitude 3 × 10^{-3} to fracture a) area with several secondary transgranular cracks, (b) detail of the area denoted by a rectangle in (a).

5.5.3 FIB cutting

SEM equipped with FIB technique was adopted in the study of the crack in-depth profiles. The secondary crack nucleated from the oxidized grain boundary during IP-TMF is presented in Fig. 73. FIB trench produced perpendicularly to the direction of the crack revealed the in-depth profile of the oxidized and cracked grain boundary, see Fig. 73b. The thickness of the oxide layer in close neighbourhood of the crack does not significantly change with advancing crack.

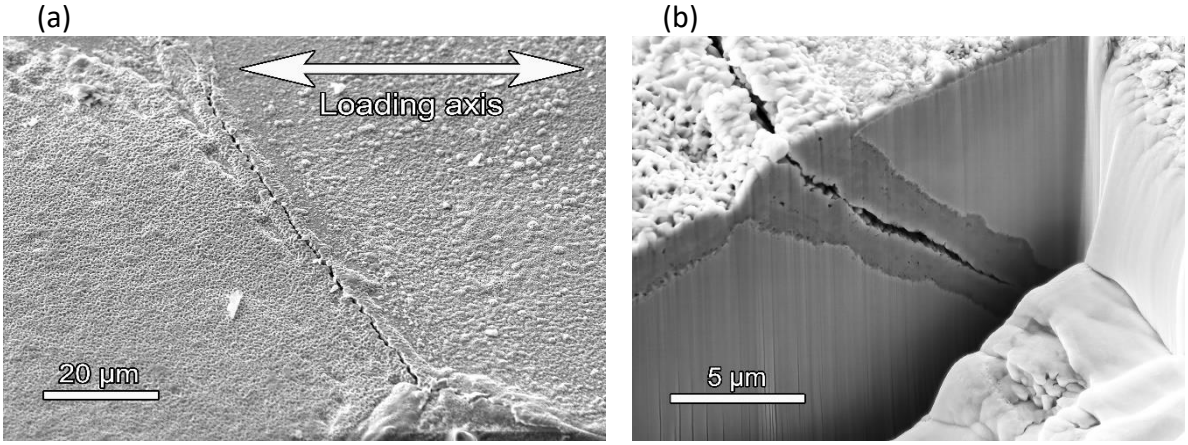

Fig. 73. (a) Cracked grain boundary after cycling with mechanical strain amplitude 3 × 10^{-3} in IP-TMF cycle (b) FIB cut of the grain boundary.

The surface relief of the specimen subjected to the OP-TMF is shown Fig. 74. The transgranular crack developed is approximately perpendicular to the loading axis. The in-depth profile revealed by FIB trench produced in the middle of the crack length shows transgranular crack decorated by the narrow oxide layer running into the material volume.

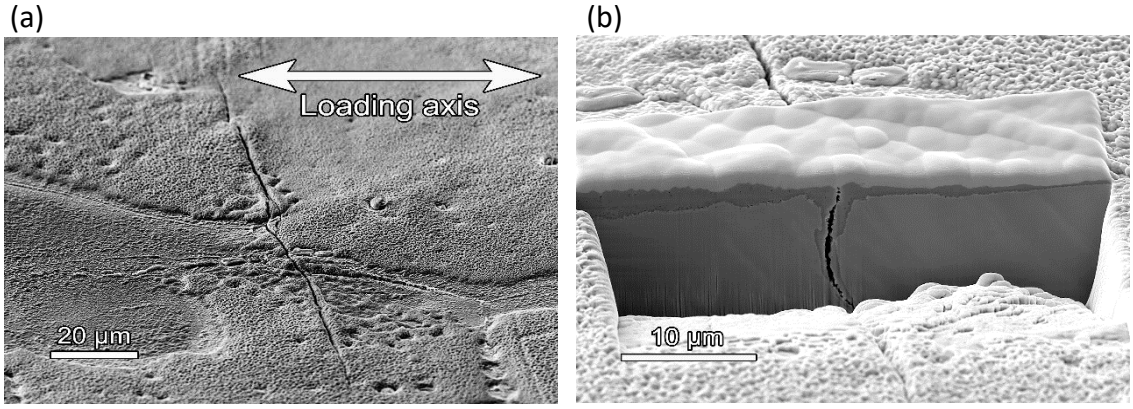

Fig. 74. (a) Surface crack produced by cycling with mechanical strain amplitude 3 × 10^{-3} in OP-TMF cycle (b) FIB cut produced perpendicularly to the direction of the crack.

In order to clarify the mechanism of the early crack nucleation under OP-TMF loading conditions additional study has been performed. For this purpose the homogeneous oxide layer formed within the grain containing thin short parallel crack was the subject of the scrutiny. In- depth profile of cracked oxide layer covered by thin platinum coating in the area of parallel short secondary cracks is shown in Fig. 75. Magnified images reveal the situation at

the interface between the material and the oxide layer. The detailed inquiry of Fig. 75b along with Fig. 75c discloses the early formation of the fatigue crack. It can be suggested that sudden cracking of the surface oxide takes place, provided the critical thickness of the developed oxide layer is reached. The crack initiated in the oxide tends to propagate through the oxide layer until the oxide/matrix interface is reached. Once the crack encounters the material it promotes the access of the oxidizing atmosphere locally to the metal surface.

(a)

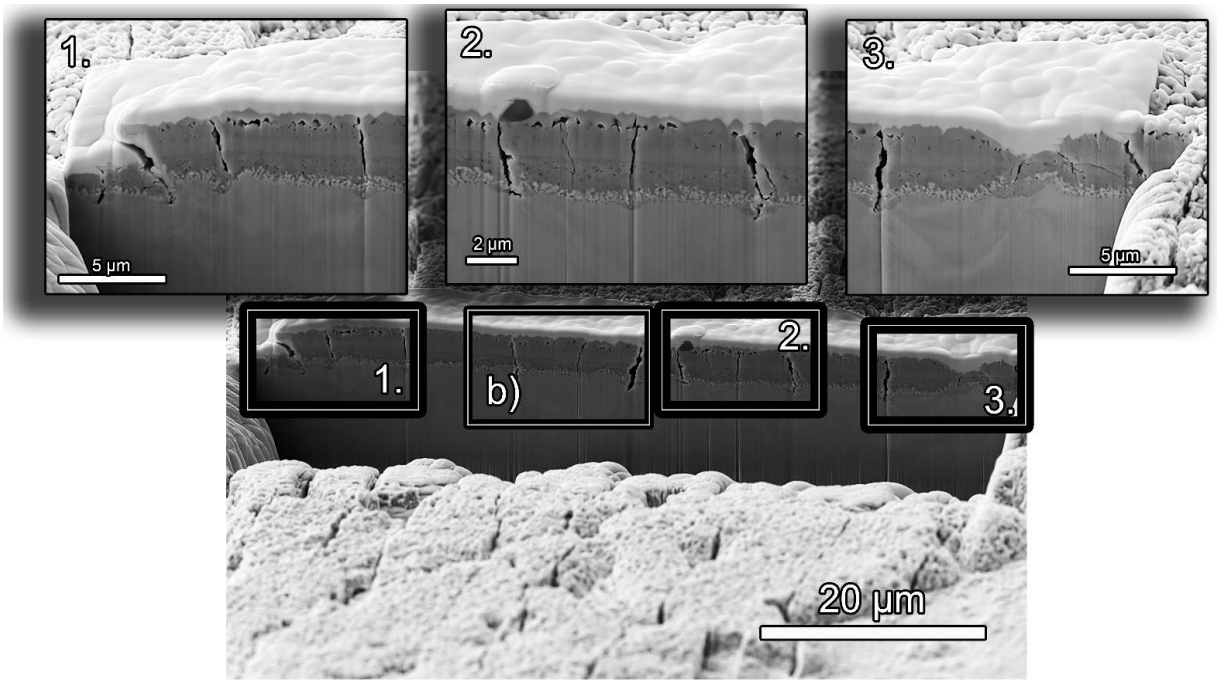

(b)

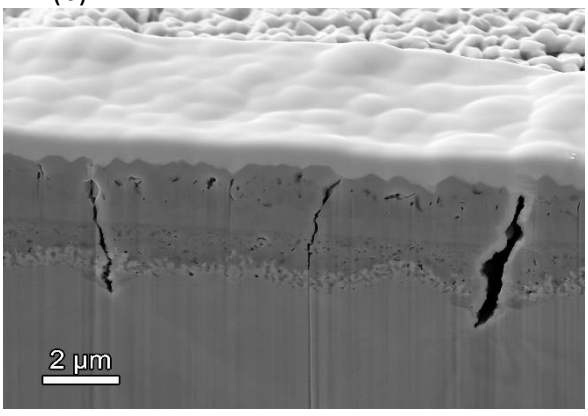

(c)

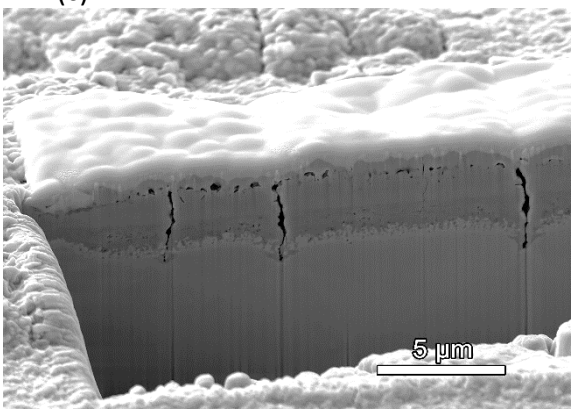

Fig. 75. Short parallel cracks in the oxide layer produced by OP-TMF cycling with mechanical strain amplitude 4 × 10^{-3}, (a) FIB cut and the surface with platinum coating; (b), (c) selected details of the FIB cut showing preferred oxidation and cracking.

Locally enhanced oxidation leads to the development of the V-shaped groove. V-shaped groove grows by alternation of cracking of the developed oxide and formation of the newly formed oxide when fresh material is exposed to the environment during cyclic loading.

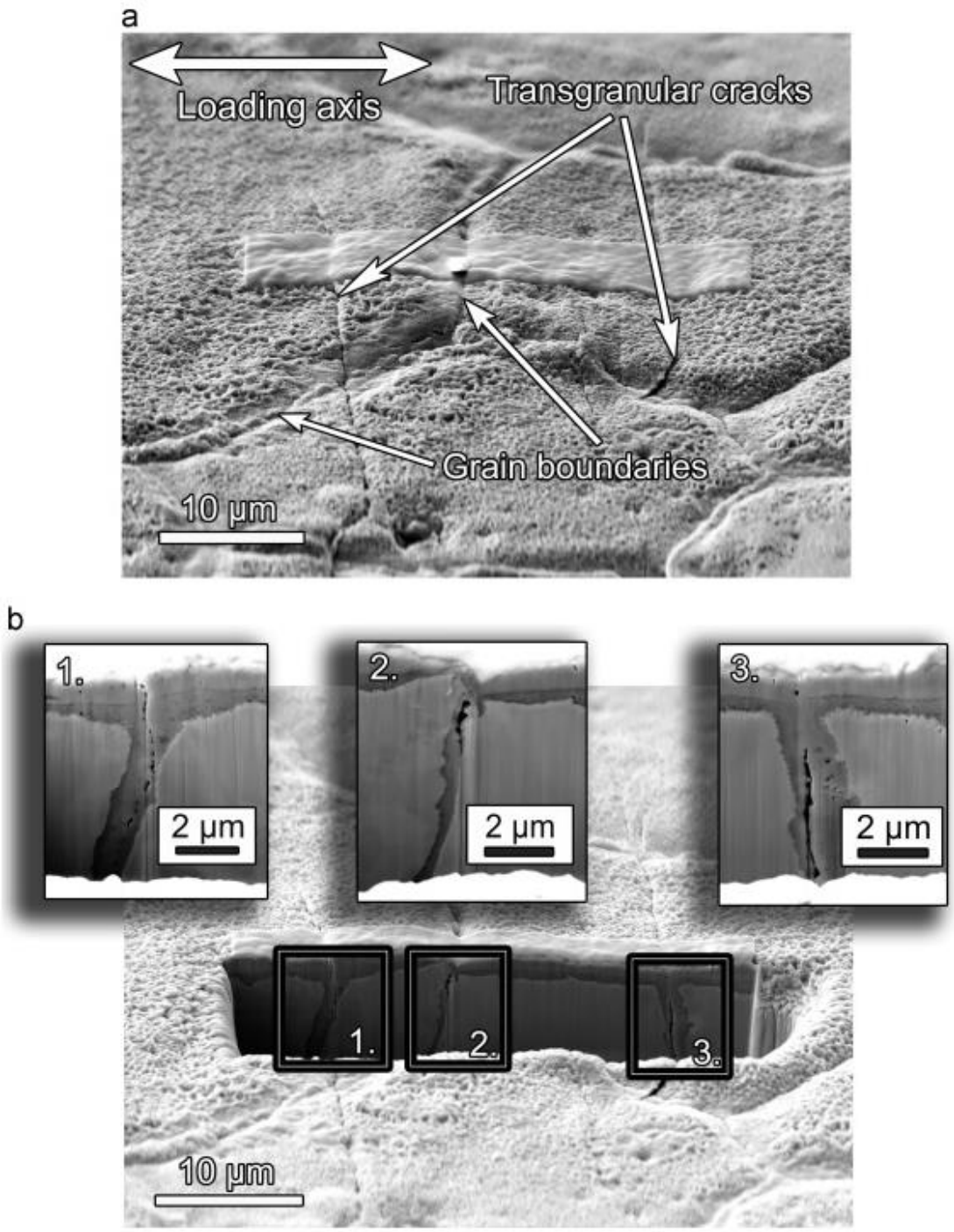

Fig. 76. Specimen subjected to OP-TMF cycling with mechanical strain amplitude 5 × 10^{-3}, (a) surface relief with platinum coating, (b) FIB cut showing in-depth profile.

In addition to the study of the crack initiation from the cracks in the uniform oxide layer, the role of grain boundaries in terms of crack formation was investigated. Fig. 76a shows the area chosen to study the importance of the grain boundary cracking which allows comparing the grain boundary cracks with transgranular oxide cracking. The platinum layer covers two transgranular cracks and the grain boundary crack between them. Fig. 76b documents the in-depth profile after FIB trench was produced. The grain boundary crack is listed in inset 2., while both transgranular cracks are shown in inset 1. and 3. Thickness of the oxide layer in the

close neighbourhood of the cracks is more pronounced in the case of transgranular cracks when compared to the cracked grain boundary. Several grain boundaries were subjected to the inquiry revealing that neither oxidation nor cracking was typical for the majority of the grain boundaries. Accordingly, it can be drawn that the cracking of the grain boundaries does not play a significant role in the crack formation comparing to the cracks developed from the uniform oxide layer.

5.5.4 Longitudinal cross section inspection

Besides the investigation of the fatigue crack initiation, the growth of the developed cracks was studied. In order to identify the crack paths, the longitudinal cross-sections of the specimen's gauge length parallel to the loading axis were machined. After production of the cross-section the surface was polished and subjected to SEM along with the EBSD technique.

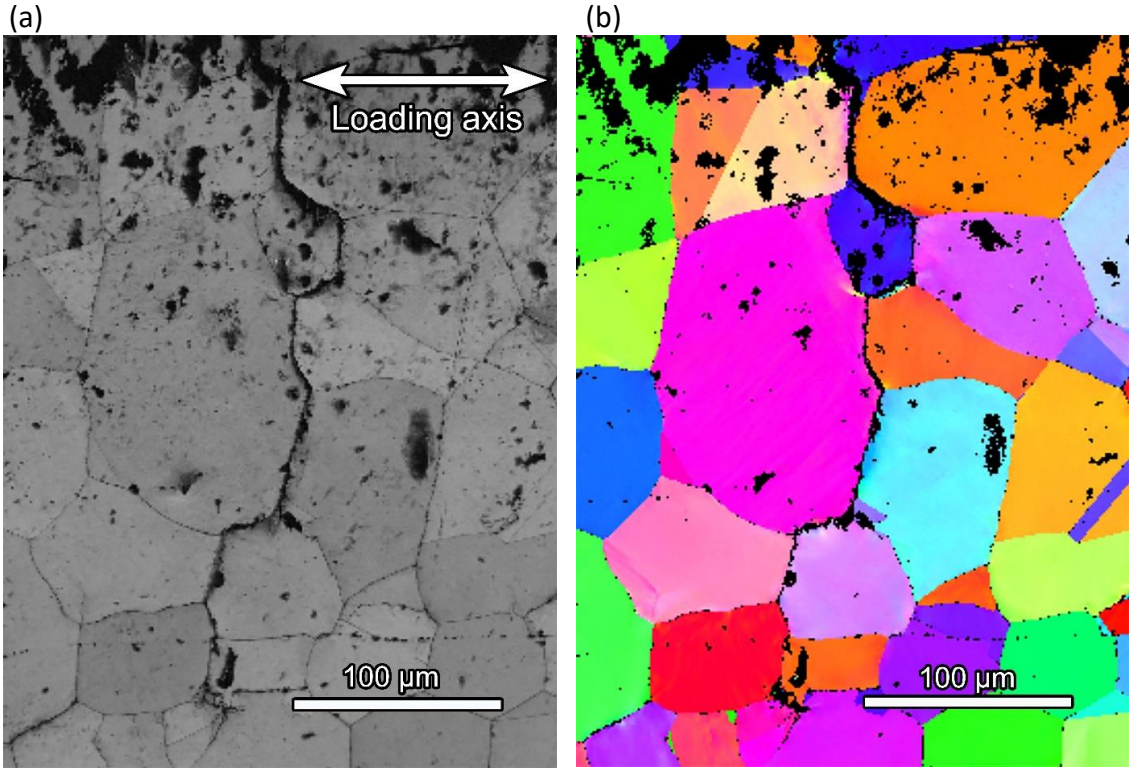

Fig. 77. Longitudinal section of the specimen subjected to IP-TMF cycling, (a) SEM image, (b) EBSD image.

SEM image of the secondary crack developed from the specimen surface under IP-TMF loading conditions is shown in Fig. 77a. Fig. 77b depicts the respective image obtained by EBSD technique. From the presented images can be concluded that IP-TM cyclic loading leads to the formation and growth of the intergranular cracks.

The situation in the case of OP-TMF loading is documented by SEM image and EBSD analysis in Fig. 78a and in Fig. 78b, respectively. Transgranular crack propagation is prevalent and results also in the branching of the crack developed in the interior of the grain.

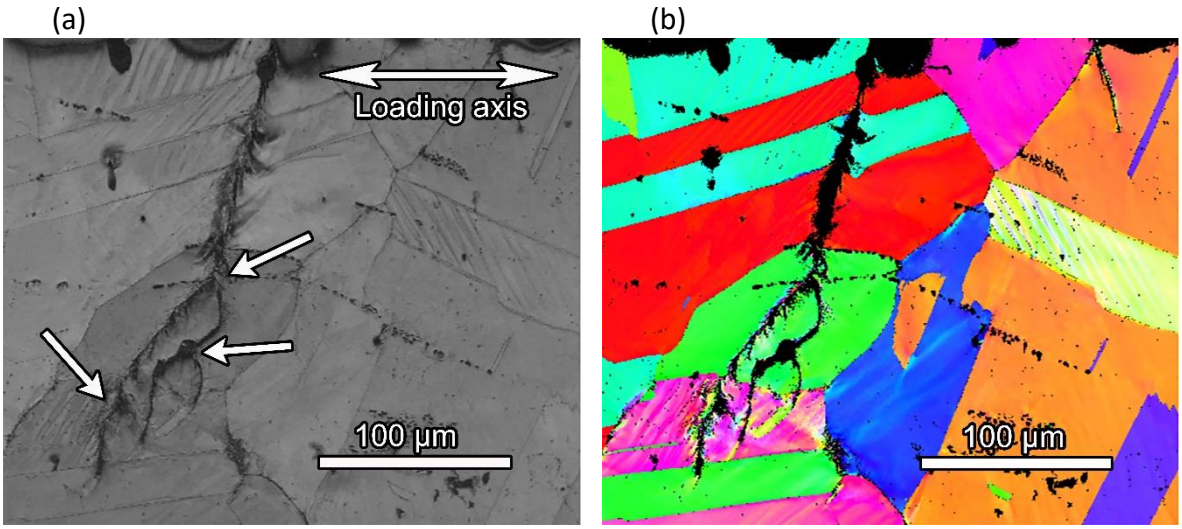

Fig. 78. Longitudinal section of the specimen subjected to OP-TMF cycling, (a) SEM image, (b) EBSD image.

5.5.5 Chapter highlights

- The material manifests rapid cyclic hardening when subjected to IP-TMF as well as to OP-TMF loading.
- The accelerated and favoured oxidation of the grain boundaries under IP-TMF conditions tends to the prompt cracking of the oxidized grain boundaries and development of the intergranular cracks.
- The transgranular crack initiation and growth under OP-TMF conditions is due to cracking of the thick oxide layer developed uniformly on the specimen surface. The localized oxidation and cracking of the newly developed oxide at the crack tip takes place once the incipient crack developed on the uniform oxide encounters the material.

5.6 Thermomechanical fatigue with dwell in the loading cycle

5.6.1 Cyclic hardening/softening curves

The response of the material exposed to the thermomechanical fatigue loading with dwell period introduced was investigated. Two different types of the loading cycle were applied; in-phase and out-of-phase cycle. The evolution of the stress amplitude σ_a plotted vs. number of the cycles *N* representing the behaviour of the material subjected to the IPD-TMF and OPD-TMF is documented in Fig. 79a and Fig. 79b, respectively. Both types of loading condition exhibit rapid cyclic hardening from the onset of the cyclic straining. While the IPD-TMF cyclic loading results in rapid hardening followed by cyclic softening, the pronounced cyclic hardening and subsequent saturation of the stress amplitude is characteristic for OPD-TMF loading conditions regardless of the total strain amplitude implemented.

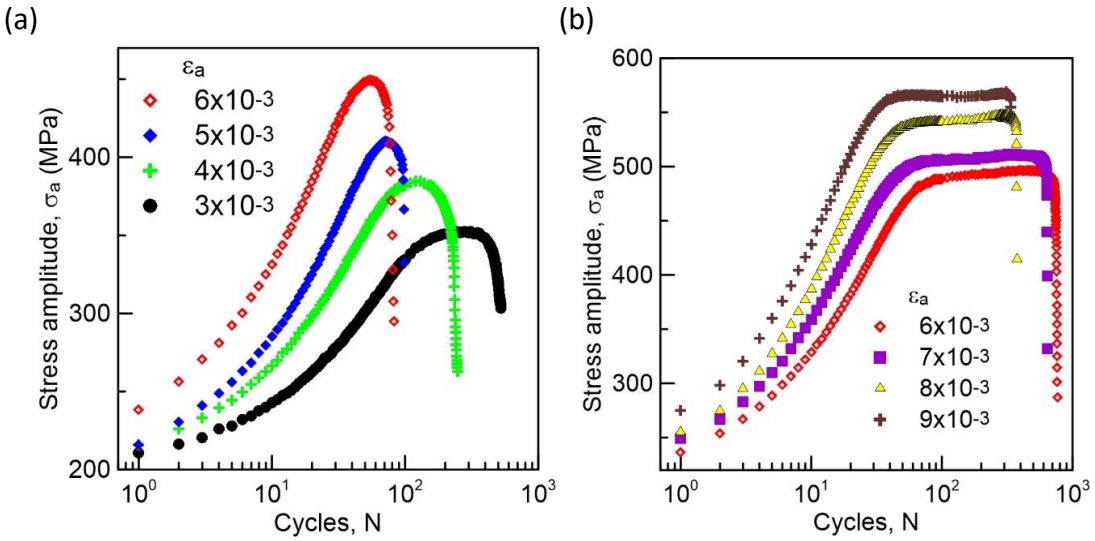

Fig. 79. Cyclic hardening/softening curves in TMF for all strain amplitudes; stress amplitude vs. number of cycles (a) in IPD and (b) in OPD cycling.

Plastic strain amplitude ε_{ap} plotted vs. number of the cycles *N* is documented in Fig. 80. The gradual decrease of the plastic strain amplitude for all total strain amplitudes applied is evident for both procedures. The evolution of the plastic strain amplitude corresponds to the cyclic hardening. Nevertheless, it should be noted that the decrease of the plastic strain amplitude in the end of the fatigue life under IPD-TMF conditions lessens that is in accordance with the stress amplitude peak followed by cyclic softening, see Fig. 79a. Continuous decrease of the plastic strain amplitude followed by pronounced saturation occurred only under OPD-TMF cyclic conditions.

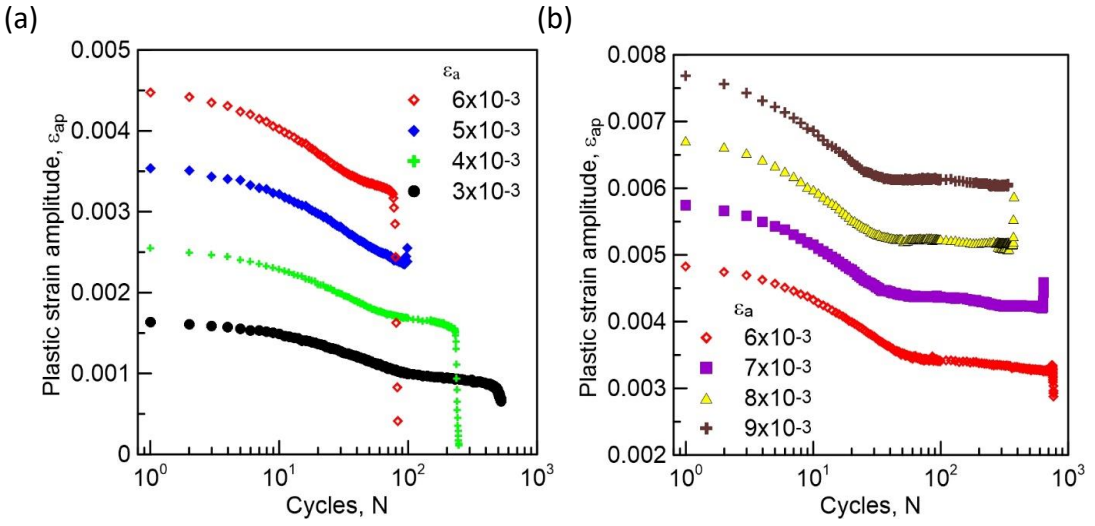

Fig. 80. Cyclic hardening/softening curves in TMF for all strain amplitudes; plastic strain amplitude vs. number of cycles; (a) IPD-TMF and (b) OPD-TMF cycling.

Evolution of the mean stress during cyclic loading for both procedures is displayed in Fig. 81. Negative mean stress is common in the whole interval of total strain amplitudes applied in IPD-TMF loading. Mean stress becomes positive in OPD-TMF tests except the final stage of the

fatigue life. Once the macroscopic crack is developed, the rapid drop of the mean stress occurred. The evolution of the mean stress is affected by the dwell introduced to the loading cycle. In order to distinguish the effect of the dwell and principal crack formation, the curves were correlated with the evolution of the plastic strain amplitudes vs. cycles. It allows separation of the effect of the straining from the effect of long crack growth. The real change of the mean stress without the influence of the principal crack can be estimated to only about 60 MPa for IPD-TMF and 90 MPa for OPD-TMF.

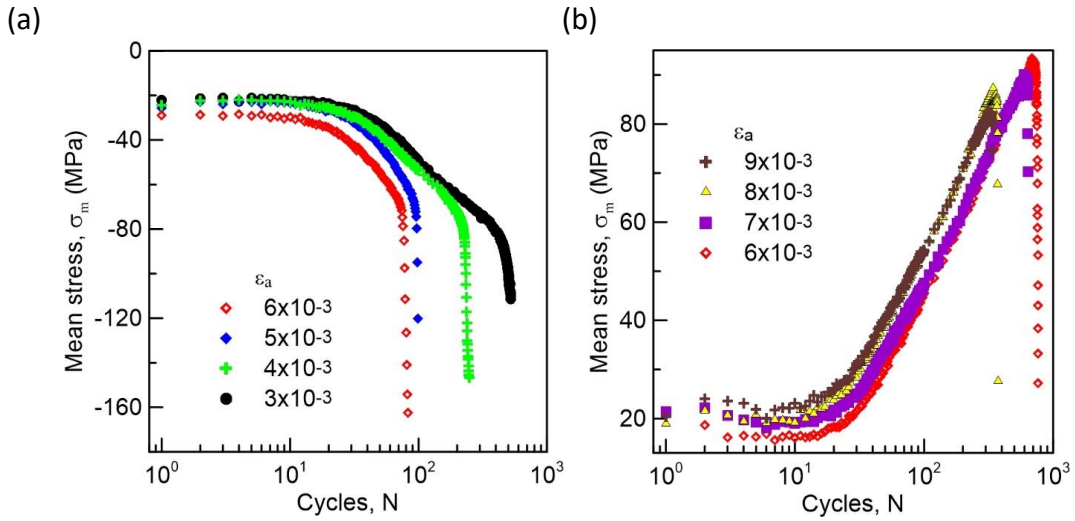

Fig. 81. Evolution of the mean stress in TMF for all strain amplitudes; mean stress vs. number of cycles (a) in IPD-TMF and (b) in OPD-TMF cycling.

5.6.2 Surface relief observation

Thermomechanical fatigue loading with dwell introduced to the loading cycle resulted in formation of the multiple fatigue cracks on the specimen surface. Mutual interaction of the cracks in close neighbourhood led to formation of the dominant crack. The secondary cracks were subject of the scrutiny to identify the mechanism of the crack nucleation. Surface relief of the specimens subjected to the IPD-TMF and OPD-TMF at the end of the fatigue life was exposed to the SEM investigation.

Fig. 82 represents the surface of the specimen subjected to IPD-TMF loading with total strain amplitude 6×10^{-3}. Oxide layer formed on the specimen surface can be easily recognized along with the bands of the thicker oxide developed preferentially at the grain boundaries. The early fatigue cracks are initiated exclusively due to cracking of the highly oxidized grain boundaries. This holds true particularly for the grain boundaries oriented perpendicularly to the stress axis.

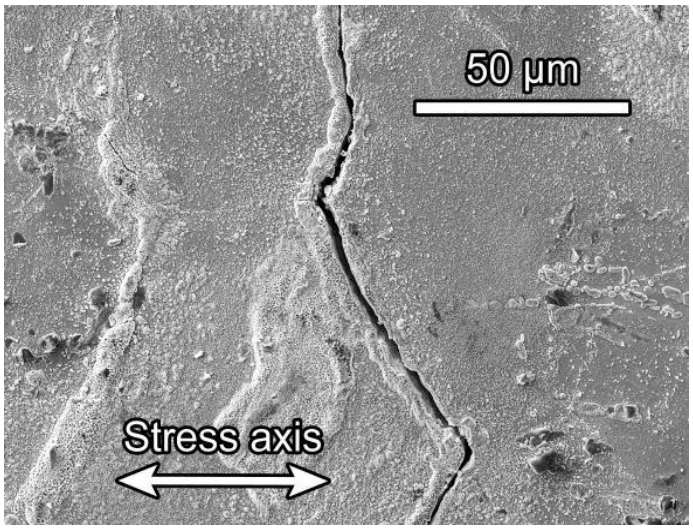

Fig. 82. Surface of the specimen cyclically strained under IPD-TMF conditions with mechanical strain amplitude 6 × 10^{-3} to fracture.

The study of the surface relief of the specimens exposed to OPD-TMF loading with total strain amplitude 6 × 10^{-3} is presented in Fig. 83. The specimen surface is highly oxidized and moreover the islands of thicker oxide layers can be distinguished within some grains. The fatigue cracks developed mainly on the thick oxide layers oriented perpendicularly to the stress axis. Tendency of the grain boundary cracking was found to be reduced when comparing to transgranular crack formation on the uniform oxide layer.

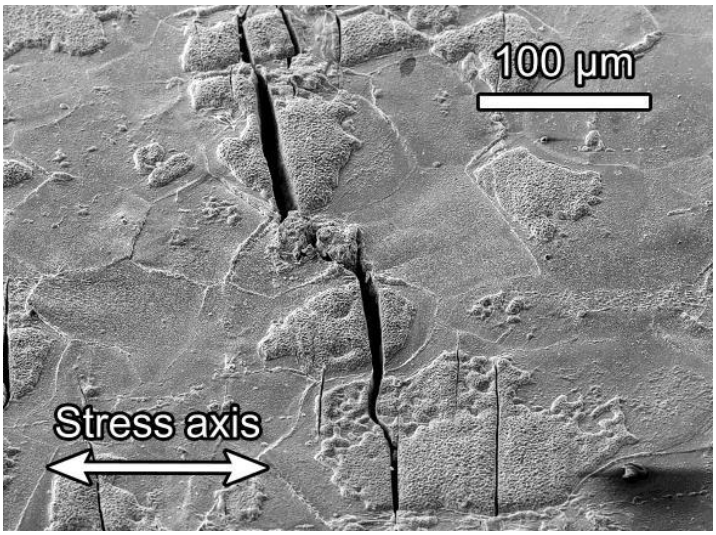

Fig. 83. Surface of the specimen cyclically strained under OPD-TMF conditions with mechanical strain amplitude 6 × 10^{-3} to fracture.

5.6.3 FIB cutting

The in-depth profile of the secondary cracks developed under IPD-TMF along with OPD TMF loading conditions was studied by means of SEM equipped with FIB technique. Once, the FIB

crater was produced, the profile was imaged using SEM. The oxidation and the cracking of the oxidized grain boundary in IPD-TMF cycling loading with total strain amplitude 6×10^{-3} is documented in Fig. 84. The crack was developed perpendicularly to the loading axis. However, the oxide intrusion changes its direction to the left when encountering the triple point where three adjacent grains meet. Subsequently, the oxidation and cracking follows the grain boundary.

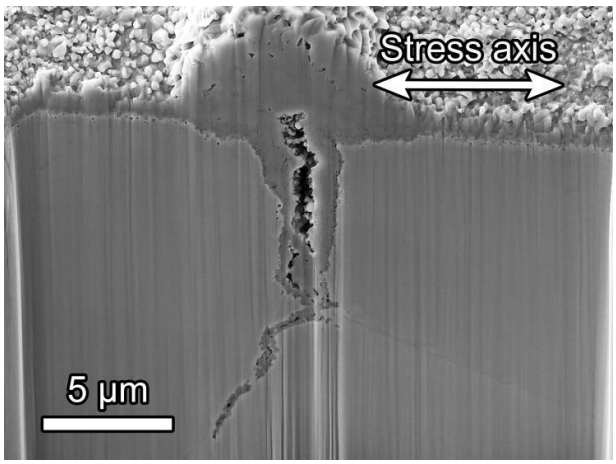

Fig. 84. FIB cut perpendicular to the surface and to the stress axis; cracked and oxidized grain boundary in specimen subjected to IPD-TMF.

The surface cracks of the specimen subjected to the OPD-TMF loading with total strain amplitude 6×10^{-3} are shown in Fig. 85. FIB cross-section revealed the in-depth profile of the oxidized and cracked grain boundary, see Fig. 85a. In addition to cracking of the oxidized grain boundaries the nucleation of the cracks from the uniform oxide layer was found in vast majority of the areas inspected as documented in Fig. 85b. Cracked homogenous thick oxide layer results in further crack development in the material.

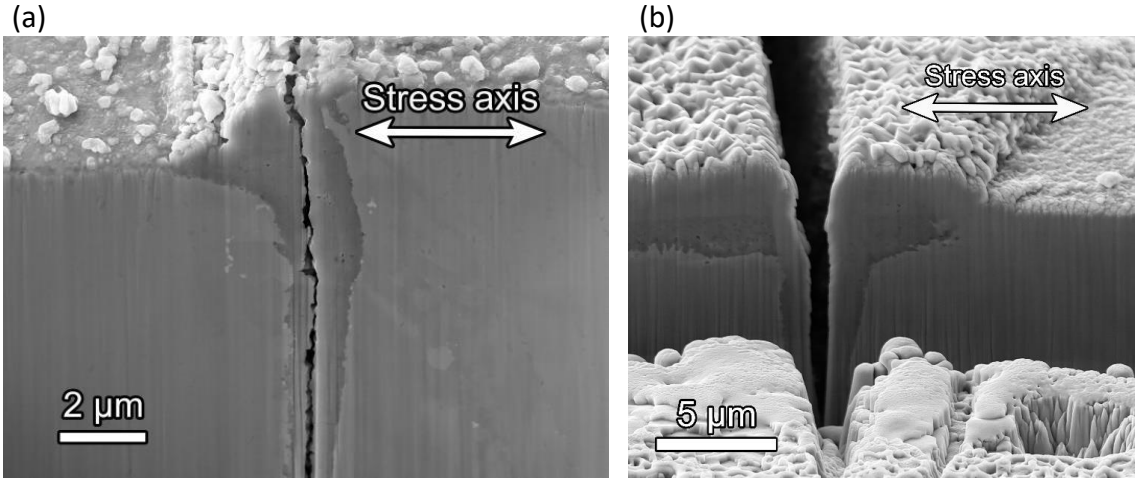

Fig. 85. FIB cuts perpendicular to the surface and to the stress axis in specimen subjected to OPD-TMF cycling; (s) cracking of the oxidized grain boundary; (b) cracking of the uniform oxide layer.

To determine the early crack formation from the uniform oxide layer specimen surface was exposed to the further investigation. Once the eligible crack was found, the FIB trench was produced perpendicularly to the crack to reveal the in-depth profile. FIB cross section of the secondary crack is presented in Fig. 86. The fatigue crack initiated from the thick uniform oxide layer propagated through the oxide to the matrix. Fig. 86a demonstrates the massive oxidation below the interface oxide layer/matrix. The growing crack facilitates the access of the oxidizing atmosphere locally to the metal surface. The situation after further loading is depicted in Fig. 86b. The crack becomes well developed and propagated not only through the oxide layer developed on the specimen surface but also through the oxidized and cracked matrix. The alternation of the oxidation and cracking of the oxide intrusion in the matrix leads to the gradual crack growth.

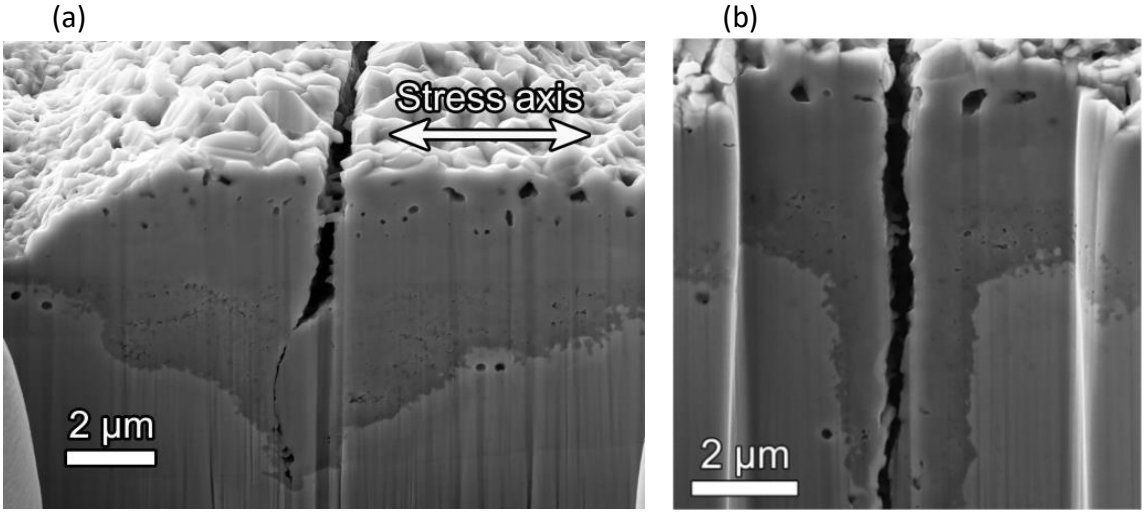

Fig. 86. FIB cuts perpendicular to the surface and to the stress axis (OPD-TMF); (a) massive oxidation of the matrix below layer/matrix interface; (b) well developed oxidized crack propagating in the material volume.

5.6.4 Longitudinal cross section inspection

In addition to the damage developed from the surface of the specimens subjected to the IPD- and OPD-TMF loading conditions; the internal damage was studied as well. For that purpose, the longitudinal cuts were produced from the specimen gauge length. Once machined, the surface of the longitudinal cuts was polished and exposed to the investigation utilizing SEM along with the EBDS analysis and EDS technique to identify the internal deterioration, crack paths and the chemical composition of the oxide layer.

Fig. 87 documents the longitudinal cut of a specimen subjected to IPD-TMF loading with total strain amplitude 6×10^{-3}. SEM image shows the crack developed from the specimen surface propagating through the material volume. The respective EBSD image revealing intergranular crack growth is displayed in Fig. 87b.

Introduction of the tensile dwell to the loading cycle led to the formation of the internal damage referred to as creep deterioration. The internal damage may significantly influence

the growth of the dominant fatigue crack due to interaction of the main crack with the internal cracks developed in its close neighbourhood. Fig. 88 shows the dominant crack on the right side of the image. The dominant crack is accompanied by the dense net of internal cracks. The multiple internal cracks are not distributed regularly along the longitudinal cut, but the vast majority of them are concentrated in close neighbourhood of the dominant crack. The crack paths of the internal crack were analysed by EBSD. Fig. 88 includes the inlet of SEM image of the representative internal crack along with EBSD image. EBSD image documents the development of the internal crack in intergranular manner.

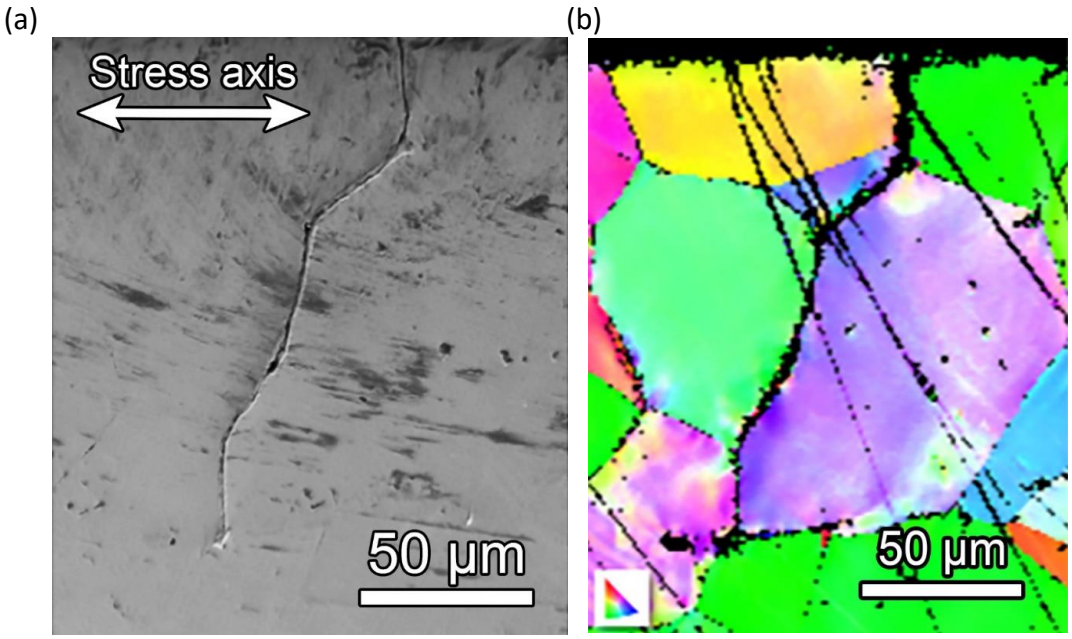

Fig. 87. Longitudinal section of the specimen subjected to IPD-TMF cycling, (a) SEM image, (b) EBSD image.

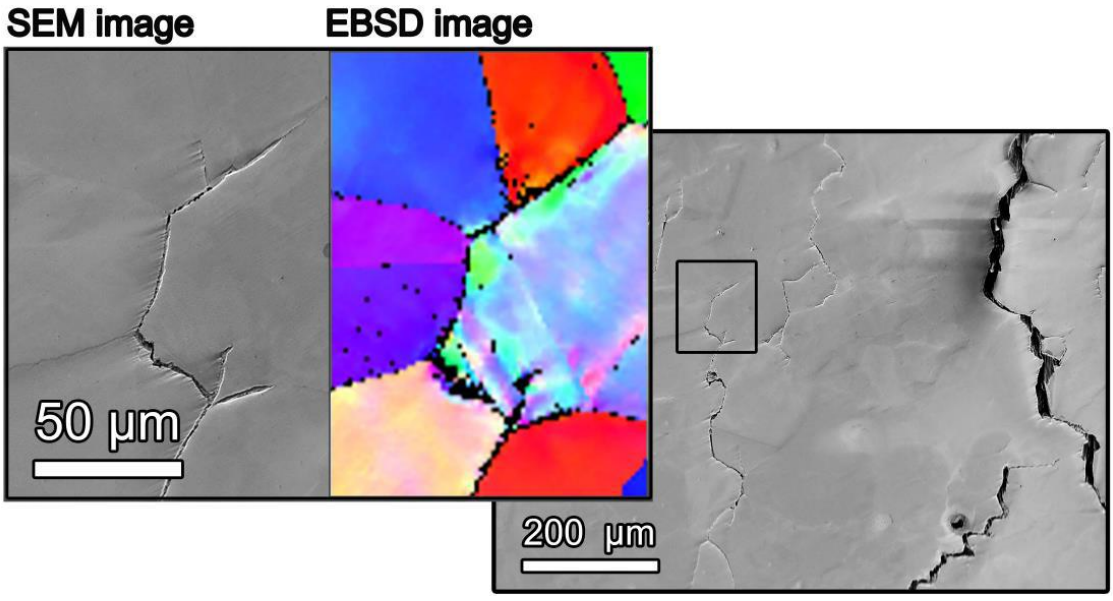

Fig. 88. Longitudinal cross section of specimen subjected to IPD-TMF showing internal damage development.

Fig. 89 shows the image of the two secondary cracks developed from the uniform oxide layer at the end of the fatigue life under OPD-TMF loading conditions with total strain amplitude 6 × 10^{-3}. Transgranular crack propagation is evident from EBSD image, see Fig. 89b.

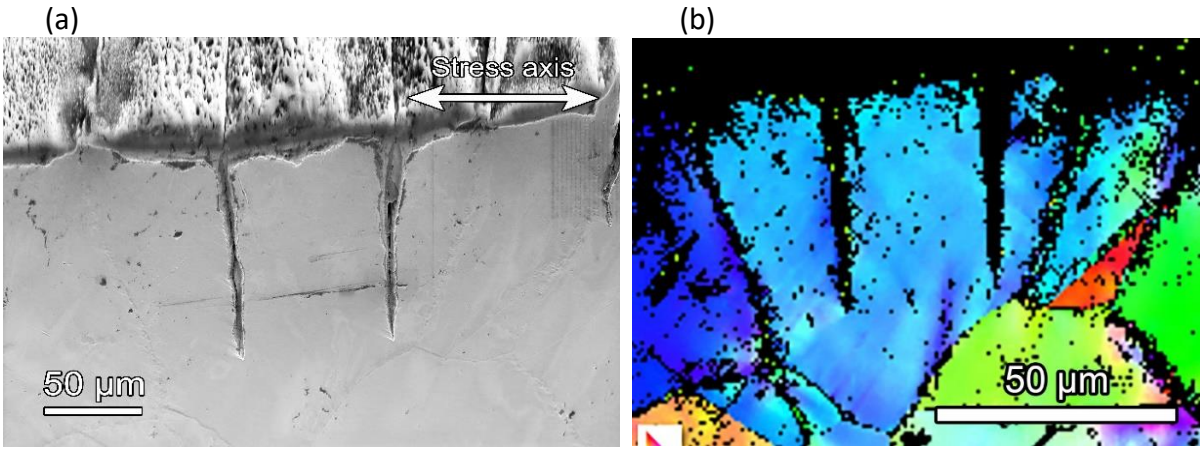

Fig. 89. Longitudinal section of the specimen subjected to OPD-TMF cycling, (a) SEM image, (b) EBSD image.

The chemical composition of the oxide layers was characterized on the longitudinal cuts by means of EDS analysis. Fig. 90 shows the well-developed oxide layer at the specimen surface along with the oxide intrusion penetrating to the material volume. The rectangle marks the area exposed to the EDS analysis and four coloured images included represent the distribution of oxygen, nickel, chromium and iron.

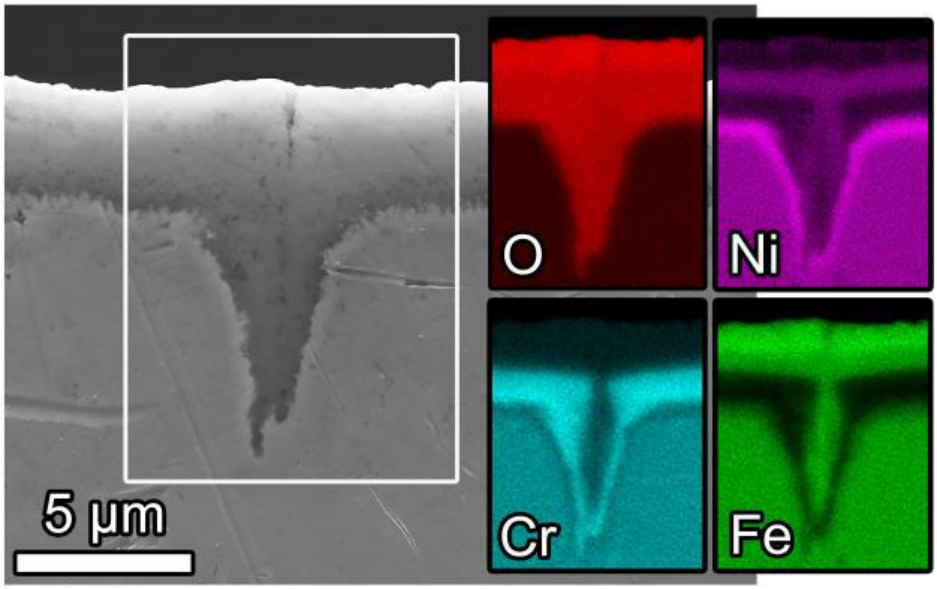

Fig. 90. Chemical composition of developed surface oxide layer under OPD-TMF loading conditions. EDS analysis of respective Fe, Cr, O, Ni content (vivid area corresponds to higher element concentration).

The double layer oxide structure can be identified based on the analyses. The Fe-rich oxide represents the outer layer, while inner layer contains typically Cr-rich oxide. The oxide on the perimeter of the oxide intrusion contains the peak fraction of the Cr and is almost completely depleted of Fe. The centre of the oxide intrusion consists predominantly of iron with minimum fraction of chromium. The interface between the matrix and inner oxide layer enriched by chromium is decorated by a high concentration of nickel. Except of the interface, the distribution of the nickel is rather homogenous in the matrix.

5.6.5 Chapter highlights

- Cyclic hardening is common for all the total strain amplitudes applied.
- In IPD-TMF loading, the accelerated crack growth of the dominant crack is related to interconnection of the dominant crack and the internal damage.
- The transgranular crack growth is driven by alternation of the local oxidation of the crack tip and the subsequent cracking of the oxide in OPD-TMF loading.

5.7 Fatigue life assessment

Fatigue life curves are documented in Fig. 91 and Fig. 92. Individual points represent the specimens strained to the end of the fatigue life. Nevertheless, the values of the plastic strain amplitudes plotted were chosen at the half-life. Plastic strain amplitude was plotted vs. number of the cycles to fracture and the data were fitted by the Manson-Coffin law $\varepsilon_{ap} = \varepsilon'_f \left(2N_f\right)^c$. Parameters ε'_f and *c* were calculated by least square fitting.

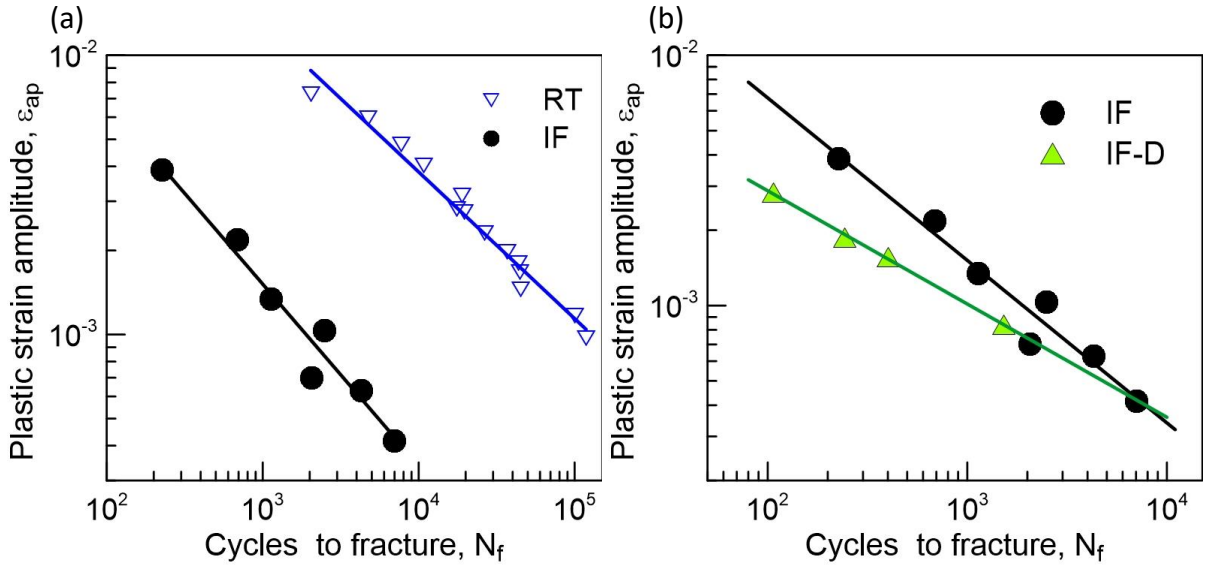

Fig. 91. Manson-Coffin fatigue life curves plotted for; (a) RT fatigue loading and for IF fatigue loading, (b) IF and IF-D fatigue loading at 700 °C.

In order to demonstrate the influence of complex loading conditions on the position and inclination of the fatigue life curves; the fatigue life curves are listed as follows. The basic room

temperature tests representing the reference are plotted along with isothermal fatigue tests conducted at 700 °C (Fig. 91a).

The significant reduction of fatigue life of the specimens subjected to elevated temperatures reflects the temperature-related response of the material in terms of microstructure and damage evolution. Introduction of the tensile dwell at high temperature into the loading cycles resulted in further decrease of the fatigue life. The decrease is important for the high strain amplitudes when compared to isothermal fatigue tests at 700°C (see, Fig. 91b). Fig. 92a documents the change of the fatigue life when the temperature of exposure varies with time. While IP-TMF loading conditions resulted in the reduction of the fatigue life in all range of total strain amplitudes comparing to isothermal loading, OP-TMF tests led to relatively similar life time for the lowest total strain amplitudes. Moreover, the fatigue lives are longer compared to isothermal fatigue especially in the case of the high total strain amplitudes.

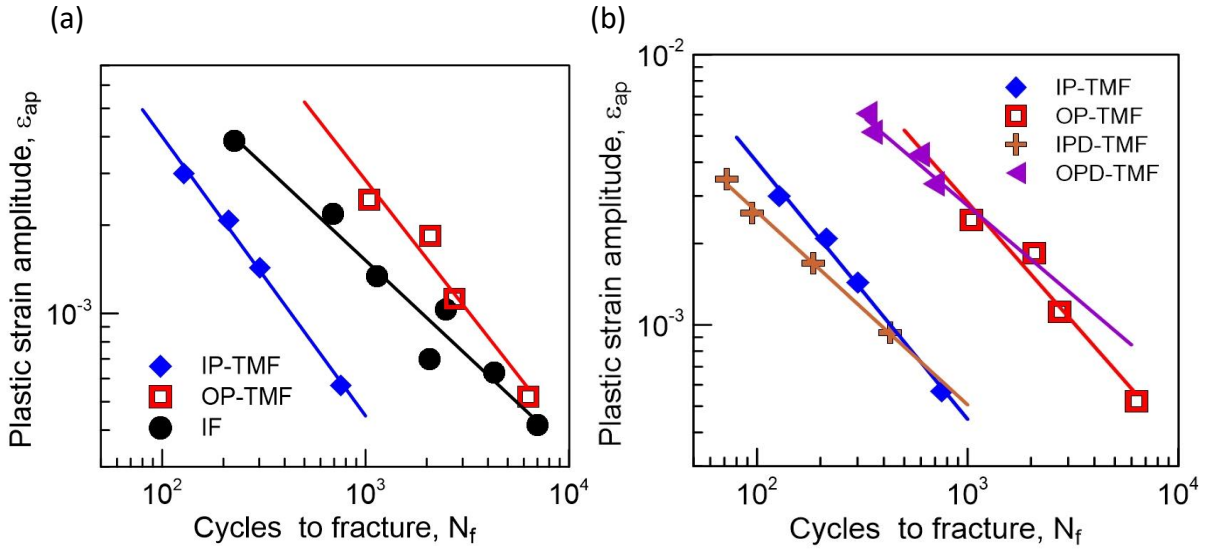

Fig. 92. Manson-Coffin fatigue life curves plotted for; (a) IF, IP- and OP-TMF loading (b) IP-, OP-, IPD- and OPD-TMF loading.

The effect of the dwell time in the loading cycle during thermomechanical cycling is shown in Fig. 92b. In IPD-TMF cycling, the introduction of dwell slightly decreases fatigue life in the domain of high strain amplitudes. The slope and the position of the fatigue live curves for OPD-TMF indicate that for the lower strain amplitudes OPD-TMF loading is less detrimental comparing to OP-TMF loading.

Both parameters of the Manson-Coffin law i.e. fatigue ductility coefficient ε_f' and exponent *c* were evaluated and are listed in Tab. 8.

Test	ε_f'	c
RT	0.694	-0.525
IF	0.211	-0.649
IF-D	0.0316	-0.452
IP-TMF	0.619	-0.952
OP-TMF	2.3996	-0.887
IPD-TMF	0.115	-0.714
OPD-TMF	0.427	-0.663

Tab. 7. Parameters of Manson-Coffin law in Sanicro 25 steel under different loading conditions.

6. Discussion

This chapter is addressed to inclusive analysis of the experimental results. Evolution of the cyclic plastic response and the microstructure is interpreted using the statistical theory of the hysteresis loops recorded during LCF tests at constant room and elevated temperature. Mechanical response as well as the early crack initiation is correlated with the loading conditions applied and assessed in relation to the available literature. Lifetime behaviour for different types of loading procedures is discussed with respect to the effective damage mechanism occurred under specific loading conditions.

6.1 Cyclic response of the material

6.1.1 The analysis of the material response to isothermal cyclic loading

The characteristic attributes of the dislocation structure in as received state in Sanicro 25 steel is planar dislocation arrangement consisting of distinctive dislocations, stacking faults, pile-ups etc. [114]. The high planarity of the slip at room temperature relative to the 316L steel is promoted by the high content of nitrogen [97]. The presence of the other alloying elements affects the yield stress that is considerably higher comparing to 316L steel and even higher than in 316LN steel [97, 103, 116, 117]. Substantially different mechanical response was observed in cyclic straining at room temperature and at 700 °C. The stress response during cyclic straining depends on the material microstructure, internal dislocation arrangement and character of the slip. All these aspects are temperature related and deeper analysis of the material response to the cyclic loading is necessary.

The mechanical response of the material subjected to isothermal fatigue at room temperature depends on the total strain amplitude applied as well. The lowest total strain amplitudes exhibit cyclic softening from the onset of the cyclic loading, alike in the case of 316LN steel [103, 116, 117]. Movement of the dislocations is restricted to planar slip within single slip system in majority of the grains due to the low stacking fault energy. The cross-slip of the dislocation is not activated [114]. It may be expected that continuous cyclic loading led to the localization of the cyclic plastic strain into the PSBs and the dislocation arrangement resembling the ladder-like structure occurred [54, 55, 57]. Nevertheless, the typical configuration of PSBs consisting of distinctive walls along with dislocation free channels has not been observed, but thin localized bands of randomly alternating dislocation rich and poor areas typically developed [118].

The cyclic softening in the low total strain amplitude may be elucidated using the results of the statistical theory of the hysteresis loop. The evolution of the distribution function during cyclic loading reveals additional information concerning the mechanism of the cyclic plastic strain straining corresponding to dislocation arrangement along with the surface relief formation of the cyclically strained materials. General statistical theory elaborated by Polák et al. [30, 31] allows to evaluate the effective stress from the shift of the probability density function. Since the main intention is to correlate the shape of the probability density function during loading with the internal microstructure along with surface relief developed, the effective stress is not discussed in detail. It should be noted that the effective stress changes

only slightly during cyclic straining especially in the initial stage of the fatigue life and the cyclic stress-strain curve along with the cyclic hardening/softening curves are designated mainly by the internal stress component [30]. The presence of the two peaks in the very first segments indicates the parallel deformation of the matrix and the bands of the localized plastic strain, see Fig.36. It can be assumed that the first peak represents the volumes of the localized cyclic plastic strain and the second peak reflects the microvolumes in the matrix where interactions of the dislocations and the developed particles of Z-phase rich on Cr, Nb and N occurred. Continuous cyclic loading leads to diminishing of the second peak and to accumulation of the cyclic plastic strain into the PSBs where all the plastic deformation takes place. The distribution function free of the second peak indicates that the matrix of the material is deformed in further cycles only elastically. The shift of the first peak of the probability density function to lower fictive stresses can be noted. Only the microvolumes having the low values of the fictive stress are effective. The proposed correlation is in good agreement with the surface relief observation of the cyclically strained materials in terms of PSMs formation from the offset of the cyclic loading. Fig. 39 documents the early formation of the PSMs with low strain amplitude early after 74 cycles. Large area of the grain surface exhibits no signs of slip indicating that yield stress in the preponderance of the grain volume is high. Only small number of microvolumes corresponding to slip bands with low yield stress is active. The profile of the PSMs is further modified during cyclic straining and stage I crack may initiate (Fig. 42c, Fig. 45b and Fig. 47c). In accordance to the formation of the one single peak during cycling, the cyclic plastic strain is fully localized in the PSBs and moreover, the initiation of the fatigue crack from the intrusion is anticipated. The different positions of the two peaks can be hypothesized in the relation to the theory of the PSMs formation [59]. The internal stresses developed in PSB lamellas as well as in PSB/matrix interface are relaxed by the motion of the dislocations in the direction of the active Burger vector. The material is extruded from the PSB forming an extrusion and one or two intrusions on the both sides of the PSB lamella [59]. Since there is a different yield stress in the PSB and the matrix, the intrusions occur on the surface with some delay comparing to the extrusion. The different yield stresses for the matrix and the PSBs may be supported by the formation of the two peaks at the different position of the fictive stress in the beginning of the cyclic loading [60, 61].

Pronounced cyclic hardening from the onset of the straining followed by the long-term fatigue softening is the hallmark for cycling at high total strain amplitude. The significant cyclic hardening is associated with the activation of the secondary slip systems leading to rapid increase of the dislocation density during the cycling loading [114]. Once the peak of the stress amplitude is reached, the material exhibits cyclic softening to the end of the fatigue life. Dislocation motion in further cycling leads to the redistribution of the dislocations and the mutual annihilation of the dislocations having opposite signs when interaction occurs. Furthermore, dislocations from the secondary slip systems are not present in developed PSBs comparing to the matrix what may suggest that all systems were effective in the beginning of the cycling, but later only one slip system dominated [114]. Accordingly, the material cyclically softens due to localization of the cyclic plastic strain. The analysis of the hysteresis loop in terms of the statistical theory revealed the formation of two peaks. Comparing to the low strain cyclic loading the second peak is very small and disappears rapidly. Overall probability density function is wider, and the position of the second peak is higher comparing to the low strain amplitude straining. This can be attributed to activation of the several slip systems. It can be assumed that the first peak is associated with the microvolumes where the localization

of the cyclic plastic strain occurs while the second one corresponds to the deformation of the matrix (see Fig.37). The position of the first peak is almost identical with the first peak developed in low amplitude straining. Also the slight shift of the first peak to lower fictive stresses during cyclic loading is similar to that observed in low amplitude straining. The formation of the PSBs reminiscent of ladder-like structure in the volume of the tested specimen strained with high strain amplitude supports the interpretation presented [114]. It seems that the effective stress for low and high amplitude cycling tends to slightly decrease. Unfortunately, there are cases, where the effective stress cannot be determined unequivocally. Initial drop of the probability density function reflects the relaxation of the plastic strain driven by decreasing effective stress in the opposite direction of the loading. Plastic strain relaxation becomes positive until the effective stress is positive and the second derivative reaches zero. However, the identification of the effective stress from the shift of the probability density function is questionable especially for the high amplitude straining. Although, the majority of microvolumes are deformed plastically under action of decreasing effective stress, the other microvolumes having low internal critical stress start to yield in the opposite direction during straining. Thus, the zero value of the probability density function is never reached. Fig. 37a documents such an example.

The cyclic plastic response of the Sanicro 25 subjected to isothermal fatigue is significantly influenced by the elevated temperature. Comparing to the room temperature straining, the intensive cyclic hardening is typical regardless of the total strain amplitude applied. The most pronounced initial cyclic hardening is noticeable for the highest total strain amplitudes. The material response to LCF tests is associated with the temperature related microstructural changes as well as dislocation arrangement. Thermally activated cross-slip significantly influences the dislocation motion that is no longer limited only to the primary slip plane [119]. The localization of the cyclic plastic strain is suppressed as indicates the microstructural investigation of the thin lamellae by means of the TEM [114, 120]. The increase of the stress amplitude during cyclic loading is attributed to the increase of the overall dislocation density. Additionally, the phenomenon of the pronounced cyclic hardening is discussed in relation to formation of the nanoparticles. The mechanism of exceptional cyclic hardening at 700°C was investigated using STEM and reported by Heczko et al. [14]. The study brought a deeper insight into atomic composition of the precipitates and allowed to understand the role of these nanoclusters in relation to the material response. Two distinctive types of nanoparticles were recognized – coherent Cu-rich and incoherent NbC nanoparticles. The rapid precipitation of NbC nanoparticles on dislocations and stacking faults is promoted by elevated temperature along with the extensive high dislocation density. The strain-induced NbC nanoparticles operate as an active barrier to be overcome by dislocation once the interaction occurs. Provided the sufficient stress is not applied, the dislocation remains pinned by these particles, see Fig. 93. Cu-rich nanoparticles are small precipitates coherent with the matrix and homogeneously dispersed with high density. Heczko et al. [121] recently reported that densely dispersed Cu-rich nanoparticles and increased number of incoherent NbC carbides have an essential influence on confinement of dislocation motions. Both types of the nanoclusters as well as the high dislocation density due to enhanced cross-slip at 700 °C significantly contribute to the extraordinarily cyclic hardening.

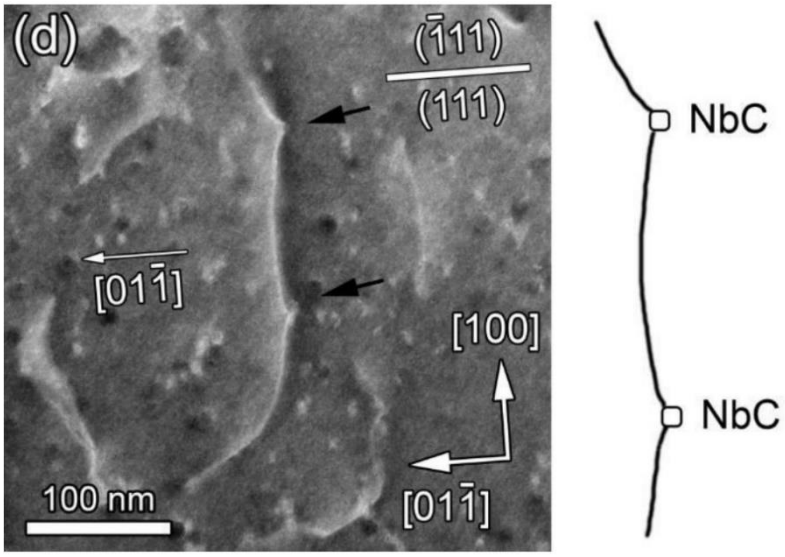

Fig. 93. HAADF-STEM image obtained along [001] zone axis with enhanced strain contrast. The pinning effect; interaction of the two NbC nanoparticles denoted by black arrows and the edge dislocation [14].

In terms of the statistical theory the similar behaviour of the material subjected to LCF at 700 °C in low and high strain amplitude cycling was observed (see Fig.49 and Fig. 50). The distribution function in low amplitude straining resulted in the formation of the thin single peak centred at fictive stress app. 130 MPa. The further loading led to the broadening of the peak and its centre was shifted to the higher fictive stress at app. 320 MPa. Moreover, the shift of the effective stress to the higher values is noticeable. TEM investigations confirmed that the cyclic strain localization is prevented, and rather homogeneous dislocation arrangement typically occurred. Consequently, it can be presumed that the average mobile dislocation density is low. In order to achieve the controlled strain rate during loading test the average dislocation velocity must be high that corresponds to the high effective stress. However, due to the presence of the nanoparticles developed in the matrix the situation is much difficult. Considering matrix and nanoparticles it can be assumed that we are dealing with the two-phase material. Both phases are deformed simultaneously, and effective stress corresponding to matrix and nanoparticles cannot be divided into two peaks and distinguished unequivocally like in the case of IN738LC superalloy [38].

Similar evolution of the distribution function was found also in the case of high amplitude straining. Rather smooth and gradual evolution of the distribution function during high amplitude straining compared to low amplitude straining can be identified and correlated with the cyclic hardening curves (see Fig. 48a and Fig. 50a). Fig. 50a demonstrates the evolution of the distribution function for high amplitude straining. The gradual decrease of the single peak and smooth shift of the peak centre to higher values of the fictive stress can be recognized. Subsequent broadening of this peak and its further shift is evident. The evolution of the probability density function is in good agreement with the rapid cyclic hardening from the onset of the loading, see Fig. 48a. The peak position of the probability density function is relatively stable in low amplitude straining in the onset of the loading and does reflect less pronounced shape evolution in the beginning of the cycling, see Fig. 49a. Fig. 48a shows that the cyclic hardening is moderate in the beginning of the cycling for low amplitude straining.

After about 1000 cycles rapid increase of the stress amplitude follows that is in accord with the evolution of the probability density function.

The probability density function for high temperature cyclic loading is broadened and shifted to higher fictive stresses corresponding to high density of the dislocations due to enhanced cross-slip and interaction of the dislocations with nanoparticles. The range as well as number of microvolumes having high internal critical stresses increases. Consequently, the material cyclically hardens. Cyclic hardening rate increases along with the increase of the dislocation density. The formation of the NbC nanoparticles is significantly influenced by plastic deformation. Increased homogeneous distribution of dislocations with high density at high strain amplitudes may profoundly stimulate the nucleation, growth and coarsening of precipitates within the grains. Since the time for their precipitation is short, the rapid cyclic hardening is expected due to pinning effect of the nanoparticles especially if plastic strain amplitude is high in the beginning of the loading [14]. This suggestion may clarify the higher cyclic hardening rate in the beginning of the cyclic loading for high amplitude straining in comparison to the low amplitude straining [14, 114].

6.1.2 The material response to isothermal cycling loading with dwells

The mechanical response of the material subjected to the isothermal fatigue loading with dwells does not significantly differ from the response to the loading under continuous isothermal fatigue conditions. The rapid increase of the stress amplitude during loading is a characteristic attribute regardless of the total strain amplitude applied. In low amplitude straining, the evolution of the stress amplitude exhibits pronounced saturation regime towards the end of the fatigue life. Moreover, the cyclic hardening rate is much higher in contrast with the isothermal fatigue. Analogous to the isothermal fatigue, the rapid extraordinarily cyclic hardening can be attributed to the increasing dislocation density during cyclic loading as well as to the nanocluster related pinning effect of the dislocations [114]. The formation of two types of temperature and time dependent nanoparticles; coherent Cu-rich and incoherent NbC particles is anticipated. The precipitation of the nanoparticles is enhanced by the introduction of the dwell to the loading cycle due to increase of the plastic strain amplitude and the cyclic hardening rate increases, see Fig. 48a and Fig. 55a. Moreover, the dwell represents additional time for formation of the nanoclusters contributing to the increased density of the particles in the beginning of the cycling. Similar experimental procedure including the experiments with and without dwell were performed in the study of material response in 316 stainless steel [112]. The tests were carried out at 650 °C with and without 450 s tensile dwell. Comparing to Sanicro 25, the cyclic hardening in 316L is much lower and saturation of the stress is reached after very few cycles. Cyclic hardening rate in 316L steel does not differ for these two types of loading. The hardening rate corresponds to the multiplication of dislocations and formation of stabilized dislocation structure without any interaction with nanoclusters [112].

6.1.3 The material response to TMF loading with and without dwells

The material response significantly depends on the loading conditions implemented. The influence of the testing procedure is crucial especially when introducing the extremal loading conditions such as IP-TMF along with OP-TMF in the temperature interval from 250 to 700 °C strained with constant mechanical total strain amplitudes. The trend of the initial cyclic hardening is rather similar for both testing procedures as well as in isothermal fatigue loading conditions at elevated temperature with and without dwells introduced. Moreover, the tendency to cyclic hardening has been observed in other austenitic stainless steels [112, 122, 123, 124, 125, 126, 127]. OP-TMF loading exhibits rapid cyclic hardening followed by the saturation of the stress amplitude, while in IP-TMF loading the premature fracture prevents reaching the saturation. This leads to considerably longer fatigue life under OP-TMF than under IP-TMF loading conditions.

Introduction of the 10 min tensile dwell into the loading cycle does not significantly affect the character of the stress amplitude evolution during cyclic loading compared to continuous TMF tests. It is important to underline that the dwell occurred always when the specimen is exposed to the peak temperature; for IPD-TMF cycle it is in tension at maximum temperature while for OPD-TFM cycle dwell is in compression at maximum temperature. Initial cyclic hardening is typical for IPD- and OPD-TMF testing procedures as observed in TMF loading without dwells. The specimens subjected to IPD-TMF loading resulted in lower fatigue lives comparing to those exposed to OPD-TMF for all the total strain amplitudes applied. The tendency to the stress saturation is pronounced under OPD-TMF testing conditions.

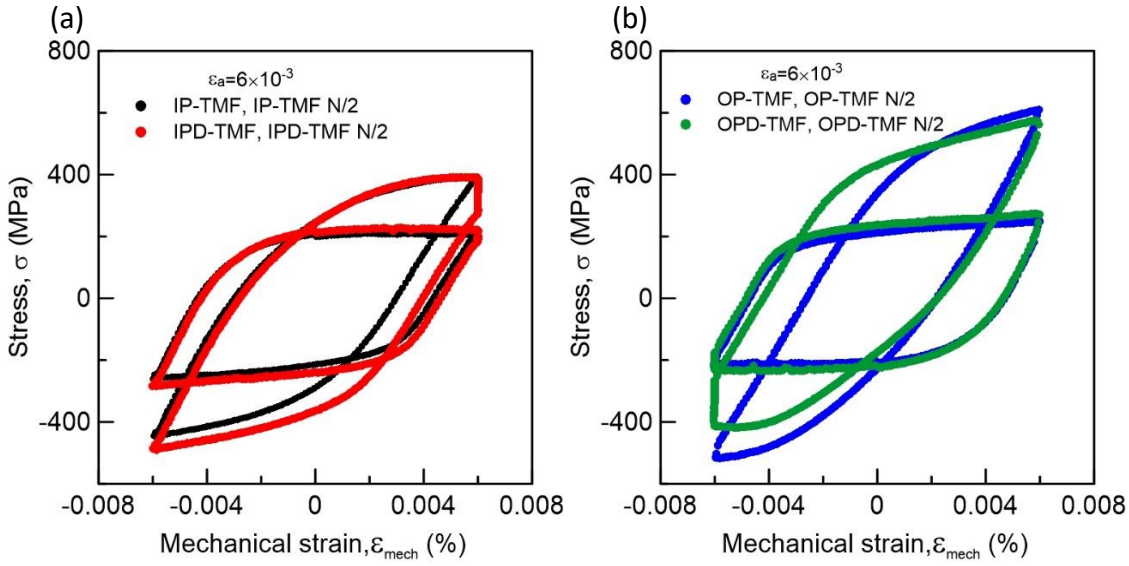

Fig. 94. Stress-strain hysteresis loops for N = 1 and N = N_f/2 in TMF cyclic straining with total strain amplitude 0.6%, (a) IP-TMF and IPD-TMF loading, (b) OP-TMF and OPD-TMF loading.

Fig. 94 illustrates the hysteresis loops shape in the beginning of the cyclic loading and their evolution approximately in the middle of the fatigue life for four tests conducted with total strain amplitude 0.6 %. For all tests, the plastic strain amplitude decreases with increasing number of the cycles indicating cyclic hardening. The introduction of the tensile dwell resulted in the broadening of the hysteresis loop regardless of the loading cycle type. The broadening

of the hysteresis loop is more pronounced for the hysteresis loops plotted approximately at half-life. This phenomenon is related to the larger plastic strain amplitude due to the stress relaxation during the dwell periods. The asymmetry in the stress response can be recognized in all TMF procedures. Generally, there is a negative mean stress in IP- and positive mean stress in OP- TMF cycling associated with the temperature dependence of the elastic modulus. When considering IP loading, the specimen is exposed to the peak temperature while in tension. The variation in the elastic modulus is driven by change of the temperature indicating an increase in the modulus when the temperature reaches its minimum in the loading cycle. This phenomenon produces the negative mean stress. The variation of the mean stress during TMF cyclic loading with dwells was found to be more pronounced when compared to the continuous TMF tests.

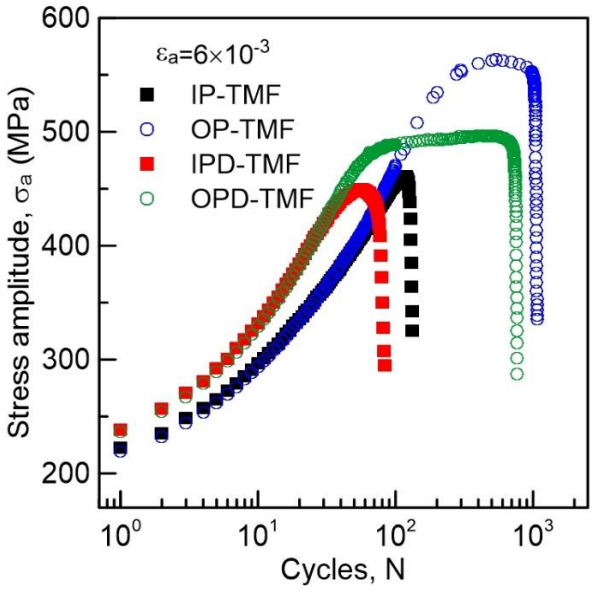

Fig.95. Cyclic hardening/softening curves in TMF along with TMF with dwell loading total strain amplitude 0.6%.

TMF tests with the dwells generally resulted in the lower fatigue lives in contrast to the tests conducted in continuous TMF loading mode. Fig. 95 illustrates the cyclic hardening/softening curves for IP- and OP-TMF along with IPD- and OPD-TMF loading for total strain amplitude 0.6 %. It can be assumed that TMF procedures with the dwells resulted in more rapid cyclic hardening due to enhanced precipitation of the nanoparticles driven by increased plastic strain amplitude. The specimens exposed to IP- and IPD-TMF straining manifest pronounced reduction of the fatigue life comparing to those subjected to OP-TMF and OPD-TMF loading. Moreover, OP-TMF along with OPD-TMF tests exhibit higher stress amplitude response with a tendency to saturation of the stress amplitude. While high stress amplitude response is evident for specimen strained under OP-TMF loading with tendency to saturation after app. 300 cycles, the pronounced saturation of the stress amplitude is notable for OPD-TMF already after app. 70 cycles.

The stress history of the specimens subjected to the distinct TMF procedures is documented in Fig. 96 where the maximum and minimum stresses are plotted vs. the number of the cycles for IP-TMF with and without hold times as well as for OP-TMF for both conditions in Fig. 96a

and Fig. 96b respectively. Asymmetry in the stress response can be observed during cycling; higher stress magnitudes required to reach the maximum strain at the low temperature (250 °C end of the thermal cycle at peak strain in OP- and OPD-TMF). Having plotted the evolution of the stress; rapid cyclic hardening can be recognized from the onset of loading for all TMF procedures. TMF loading generally resulted in gradual increase of the stress possibly due to generation and mutual interaction of the dislocations and developed nanoparticles until the steady state is reached. The initial increase of the stress level is more pronounced for TMF straining with dwells. In the case of IPD-TMF subsequent cyclic softening notable at the end of the fatigue life may be attributed to the rearrangement of the dislocations, cutting of the precipitates or already micro-crack formation. The tendency to saturation of the stress can be found for OP- and OPD-TMF cycling after app. 300 and 70 cycles, respectively. The reduction in the stress level observed for TMF tests with dwells as documented in Fig. 96b is likely due to enhanced recovery of the dislocation structures during the dwell period.

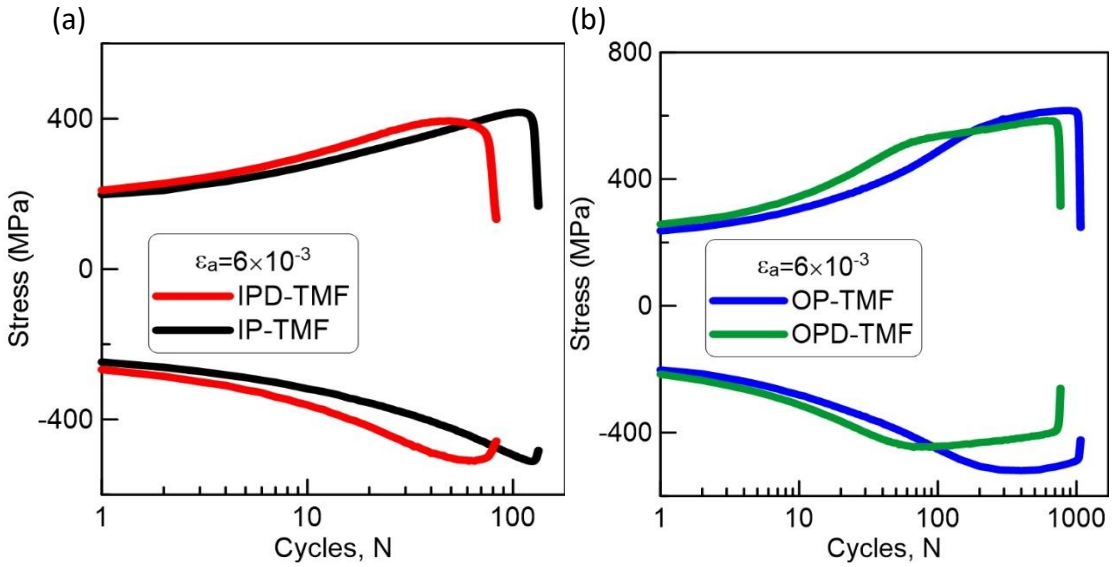

Fig. 96. Cyclic-stress response of TMF test with and without dwell introduced in temperature range from 250 to 700 °C; (a) IP- and IPD-TMF, (b) OP- and OPD-TMF.

6.2 Mechanisms of the damage

6.2.1 Damage evolution in room temperature cyclic loading

An extensive progress in the field of the crack nucleation in crystalline materials at room temperature has been achieved in recent years [56, 128, 129, 130, 131]. Nevertheless, the general agreement on the genuine nucleation site and the respective mechanism has not been reached and represents a lot of controversy. Based on the various experimental observations, the most frequent areas of the crack nucleation are PSMs formed by PSBs emerging from the matrix. PSBs represent the locations of the cyclic plastic strain localization within the material matrix. Two well-known models are frequently considered when discussing the actual source of the fatigue crack initiation at the room temperature. Essmann et al. [132] came up with an idea of the fatigue crack nucleation based on the formation of the static extrusion developed

due to the production and accumulation of the point defect in the PSB, known as EGM model. The fatigue crack initiation stems from the stress concentration given by the presence of extrusion. According to Mughrabi [131], microcrack formed within the PSB represents the stage I- crack. The production and accumulation of the point defects resulting in formation of the extrusion and two intrusions in close neighbourhood represents the concept of the Polák's approach. The assumption of point defect migration from the PSB to the matrix principally modifies the prism on the fatigue crack nucleation [57, 59, 61]. The vacancies are produced by mutual interaction between dislocations in the channels in the PSB ladder-like dislocation arrangement. The redistribution and the transfer of the matter stems from the point defects migration. The edge dislocations distributed in the matrix serve as sinks for migrating vacancies. The formation of the extrusion and intrusions is driven by the stress relaxation in the direction of the Burgers vector. The delayed intrusion formation compared to extrusion is given by the higher yield stress of the matrix than of the PSB [60, 61]. The intrusion represents a crack-like defect and the crack is initiated from its tip. The shape of the extrusion-intrusion pair was predicted for simplified situation by elaboration of the original idea [59, 61].

Despite of the numerous observations using various experimental procedures, the direct experimental evidence of the fatigue crack initiation has been missing. The question whether the fatigue crack is initiated due to the stress concentration caused by the extrusion or by crack-like intrusion remained open. The main intention of this contribution is to provide the experimental evidence of the early crack initiation from the PSM developed on the material surface in austenitic stainless steel at room temperature. FIB technique along with SEM involved in the study enables to reveal the perpendicular profile of the PSM containing suspicious area of crack formation and subsequently to follow the process of the surface relief evolution in further cyclic loading.

The study of the surface relief evolution in Sanicro 25 steel cyclically loaded with constant total strain amplitude at room temperature disclosed early PSMs formation in the onset of the loading. Feebly developed PSMs consisting of extrusions and intrusions are noticeable already at 0.25% of the fatigue life. Later modification of the PSMs profiles is driven by subsequent cyclic loading. Accordingly, the extrusions are becoming more pronounced and may cover the deepening intrusions. The surface of the vast majority of the grains is decorated by well-developed PSMs consisting of extrusions and intrusions (see Fig. 40b as an example). Nevertheless, the early crack initiation cannot be distinguished unequivocally especially when intrusions are covered by pronounced extrusions.

Three distinctive illustrations of the PSMs profile modifications were listed. Fig. 42a documents the profile of the first PSB subjected to the detailed study. Dominant extrusion to the left and parallel intrusion developed nearby is accompanied by several smaller extrusions and intrusions. Additional 444 cycles (Fig. 42b) did not result in significant change of the PSM profile except of the formation of the intrusion to the right. Still larger intrusion was produced in the centre of the PSB after another 444 cycles were applied. Finally, the crack was nucleated from the tip of intrusion developed almost in the centre of the PSM, see Fig. 42c. Here comes the question how to distinguish the intrusion from crack unequivocally. In this study, the early crack was determined by its different geometrical profile. Hunsche el. al [133] recognized two processes during observation of specimen's profile by sectioning technique: (a) the roughening of the surface producing intrusions and (b) stage-I cracks. The idea to distinguish

the intrusion from crack is the crack tip angle at vertex. The value of the crack tip angle α should be used to determine the terms intrusion where α>20°, while α=0 for stage-I crack.

The other two locations show similar surface evolution. The evolution of the two PSMs profiles in one grain was documented in Figs. 43-45. The profile of the No.1 PSM (see Fig. 44) exhibited no significant change in further loading. The formation of the massive extrusion accompanied by the deep intrusion to the right is noticeable in PSM No.2 after 740 cycles (Fig. 45a). Additional cycles resulted in the growth of the extrusion, gradual deepening of the intrusion and nucleation of the early fatigue crack from the tip of the intrusion. Another straightforward illustration of the crack nucleation is given in Fig. 46 and Fig. 47 revealing the deepening of the intrusion. The fatigue crack initiation from the tip of the intrusion is captured in Fig. 47b after 1406 cycles along with Fig. 47c documenting further growth of the crack running along the primary slip plane.

All cases of the surface relief formation in the grains of Sanicro 25 steel provide the evidence of a great variability of the individual PSMs profiles. Typical attributes of the surface relief formation leading to crack initiation are obvious. Localization of the cyclic plastic strain in PSBs within the material manifests as a formation of the characteristic local surface relief emerging from the matrix. Intrusions represent nucleation-sites. Once the intrusion is formed, additional cycling may lead to stage I-crack growth from the very tip of the intrusion. The intensive inquiry of the surface relief profiles revealed that the PSMs do not always consist of single pronounced extrusion accompanied by the intrusion, but the profile is typically highly diverse. Bearing in mind that the localized cyclic plastic strain is not homogeneous along the width of a PSB, the local surface may differ from the adjacent one within a single PSB reflecting the continuous redistribution of the matter. In the location of the initial extrusion an intrusion may develop and vice versa. Nevertheless, in the vast majority of the situations, the extrusion continues to grow while intrusion typically deepens and nucleation of the early crack becomes highly plausible.

Investigation of the PSMs profile evolution supported the idea that the fatigue crack does nucleate from the tip of the intrusion that was formed as a part of the PSM consisting both of extrusions and intrusions. The formation of the extrusion is supposed to be the dominant attribute in terms of the EGM model [134]. The intrusions are believed to be embryonic stage I shear cracks as a result of previously developed static extrusion. In any, observation performed here the crack did not nucleate in the absence of prior formation of the intrusion. Moreover, the situation depicted in Fig. 44 resulted in slightly modification of the PSM profile and further cycles did not lead to the initiation of the crack at all. Apparently not all the intrusions produce crack. The depicted situations of the crack nucleation are not in favour of EGM model of the fatigue crack initiation. Nevertheless, more reasonable correlation can be made when considering Polák's model predicting the crack initiation [57, 59, 61]. Fatigue cracks in all cases started from the tip of the intrusion.

The scrutiny of the PSBs dislocation structure in Sanicro 25 steel disclosed highly complex pattern when comparing to simple metals like copper [135, 136, 137, 138]. Investigation of the surface foil produced by FIB arranged perpendicularly to the surface as well as to the direction of the PSM by means of TEM revealed dislocation arrangement contributing to the formation of the surface relief (see Fig. 97) [118]. Fig. 97 documents the profiles of three PSMs denoted as B, C, D and the respective dislocation structure along with the dislocation

arrangement in the matrix. PSMs consisting of extrusions, several fine intrusions and even short cracks nucleated from the tip of the intrusion can be recognized. Well-known ladder-like arrangement is absent. However, the formation of the dislocation rich areas alternated with areas free of dislocations is apparent. In accord to experimental findings Polák et al. [118] concluded that dislocation arrangement in the PSBs does not considerably differ from the dislocation structure of the matrix. Nevertheless, two essential differences are present: (a) PSBs are free of dislocations from secondary slip systems and (b) low dislocation density is found in certain areas of PSBs.

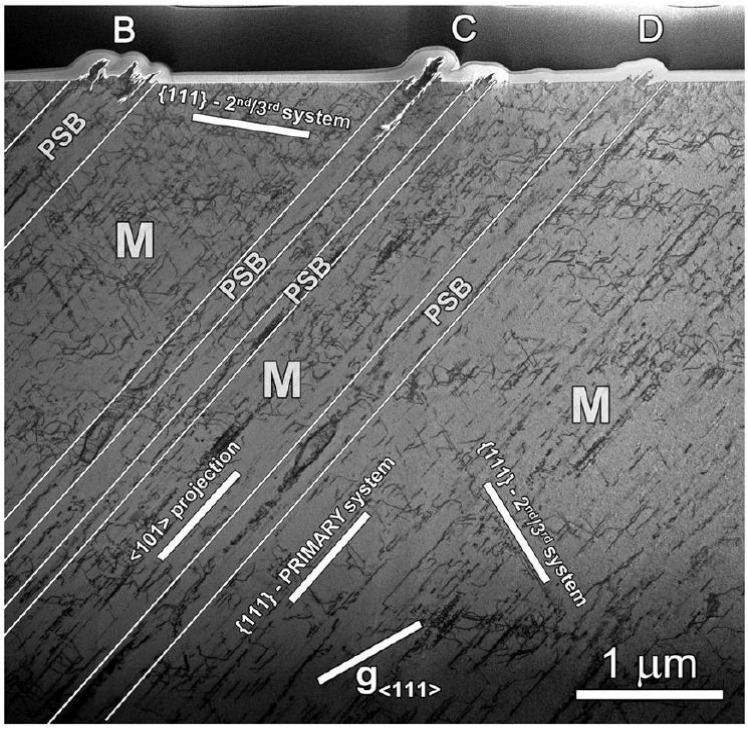

Fig. 97. TEM image of the lamella produced illustrating dislocation arrangement in the PSMs B, C and D denoted by white straight lines; M marks the matrix [118].

Point defects are produced in dislocation poor areas when two edge dislocations on neighbour planes encounter or when a jog on a screw dislocation moves non-conservatively. The non-equilibrium point defects migration to the dislocations in the matrix as well as to the dislocations within the PSB leads to redistribution of the matter. Once the internal compressive and tensile stresses arise, the plastic relaxation takes place in the direction of active Burger vector. The local modification of the relief within a single PSM in form of deepening and heightening of the surface is anticipated accordingly. Keeping in mind complex dislocation arrangement, the concept has been elaborated and not only steady growth of extrusions and deepening of the intrusion is effective but also the local modifications such as reduction of extrusion height or flattening of intrusion were reported [118]. The initiation of the stage I crack from the tip of the intrusion is, however, still the essential hallmark of this concept supported by experimental findings. Once the stage I crack is nucleated, the cyclic plastic strain is subsequently localized to the crack tip resulting in stage II crack growth.

6.2.2 Damage evolution in high temperature cyclic loading

The damage evolution significantly depends on the actual loading conditions implemented. In addition to the operating parameters such as loading waveform, total strain amplitude, strain rate and temperature the damage mechanism is environmentally related as well. Considerable differences in fatigue lives of the specimens subjected to various loading conditions can be attributed to distinctive damage evolution. The operating damage mechanisms were identified from the inspection of the secondary cracks developed on the specimen surface by means of SEM along with FIB cutting technique at the end of the fatigue life. FIB technique has been adopted to gain the profile of the secondary cracks and to clarify the role of the oxidation in the process of crack nucleation. Moreover, the internal damage evolution is anticipated as well. For that reason, the SEM study of the longitudinal cuts produced from the specimen gauge length parallel to the loading axis was engaged. Additionally, EDS and EBSD techniques have been utilized to identify the chemical composition of the oxide layer developed and to determine the relation between the crack and grain orientation respectively.

The exposure of the specimen to the high temperature cyclic loading resulted in the formation of the thin uniform oxide layer within the grains. Thick oxide bands preferentially developed at the grain boundaries occurred as well. This holds true mostly for the grain boundaries arranged perpendicularly to the stress axis. The formation of the enhanced oxide layer is associated with decreased content of the chromium due to precipitation. Mazánová et al. [139] recently reported on $M_{23}C_6$ carbides formation predominantly developed at high angle grain boundaries (HAGBs) during high temperature exposure. Distinctive oxides developed on the specimen surface and in the oxide intrusion proceeding through the material in the direction following the grain boundary. EDS analysis revealed the double layer oxide structure formation on the specimen surface as well as in the oxide intrusion. The inner layer close to the metal surface is protective layer of Cr_2O_3. The outer layer is oxide enriched by iron. The oxide developed in the centre of the oxide intrusion consists of Fe-rich oxide, while the outer oxide is Cr_2O_3. The protective layer serves as a diffusion barrier for oxygen, so the continuous oxidation of the matrix is prevented. The interface between the oxide and the matrix is enriched in Ni. Kim et al. [140] considered that the Ni enrichment of the matrix at matrix/oxide interface could be related to different diffusion rates since lattice diffusion rate of Ni is reported to be low when compared to Fe and Cr in Fe-Cr-Ni alloys [141].However, it could be the result of higher oxidation rate of Cr than that of Ni as well. and due to diffusion of Cr to the oxide the matrix at the matrix/oxide interface is enriched in Ni. The similar oxide structure reminiscent of observations listed was reported by Intiso et al. [142]. The double layer oxide structure has been formed at the specimen surface exposed to static oxidation test at 600 °C in dry and wet O_2 environments on Sanicro 25. Static oxidation test resulted in formation of the protective oxide layer and further oxidation of the matrix was prevented. When applying sufficient tensile stress, the brittle fracture of the oxide developed along the grain boundary is likely to happen. Once cracked, the tensile stress promotes the diffusion of the oxygen locally to the fresh metal surface exposed to elevated temperature resulting in oxidizing processes. The alternating oxidation at the crack tip and subsequent brittle fracture of oxidized layer represent the mechanism of the early crack growth. This mechanism is widely accepted as the stress-assisted grain boundary oxidation (SAGBO) proposed by Kang et al.

[143]. The mechanism reflects an effective process clarifying rapid initiation of the fatigue crack and enhanced initial crack growth rate.

6.2.3 Damage evolution in high temperature cyclic loading with dwells

The high temperature cyclic loading with the 10 min tensile dwell implemented into the loading cycle resulted in rather similar effective damage mechanism in terms of the cracking of the oxidized grain boundaries. However, the cracked oxidized grain boundaries are exposed to the oxidizing atmosphere for longer time under the action of the tensile dwell. The crack growth rate is expected to increase appreciably primarily due to long oxidation time exposure of the crack tip within a loading cycle. The environmental oxygen plays an essential role in the process of dynamic embrittlement. The diffusion of the oxygen from the crack tip into the material along the grain boundaries is promoted by the tensile load, dwell time and temperature. Wagenhuber et al. [144] investigated the fatigue crack propagation behaviour of alloy 718 under different loading conditions with different hold times at 650 °C to illustrate the detrimental role of oxygen. The increase of the hold time resulted in significant reduction of the numbers of cycles to failure and the change of the fracture mode from transgrannular to intergranular was observed due to oxygen diffusion into the highly stressed grain boundaries. An accelerated crack growth attributed to increasing dwell time due to the effect of dynamic embrittlement was also reported by Christ et al. [145].

In addition to the preferential grain boundary oxidation and its cracking, the wedge type crack formation was frequently observed on the specimen surface as well. This contribution to the surface damage is typically formed during the hold time period of the loading cycle driven by creep. The sliding of the favourably oriented grains due to stress concentration leads to the production of wedge-type cracks. Moreover, the formation of wedge-type cracks can be promoted by the cavity accumulation reported to occur during creep [104]. The further microcrack growth along the grain facet is driven by stress concentration at the triple junction due to crack-opening-displacement during cyclic loading [83].

The experimental findings presented here are in good agreement with the extensive investigation conducted by Hormozi el al. [112] on 316 austenitic stainless steel. The material in the study was exposed to continuous low cycle fatigue as well as to low cycle fatigue test with dwells. The fractographic and metallographic inspection disclosed the dependence of the dominant damage mode in relation to the frequency applied. The intergranular time dependent damage mechanism prevails at low frequencies while transgranular failure is typically presented at high frequencies. This phenomenon can be associated with the shorter time of a loading cycle, so the contribution of the oxygen diffusion along the grain boundaries and oxidation processes is thus retarded. Based on the investigation by Zauter et al [104]; the temperature of the exposure is the crucial parameter in terms of the potential cracking mode. If the temperature applied is below the creep regime the transgranular crack initiation and propagation dominates.

Apart from the intergranular crack formation due to the cracking of the oxidized grain boundaries the cracking of the uniform oxide layer developed within the grains was documented as well. It turned out that formation of the thick oxide islands is also

characteristic feature of the specimen relief formation when introducing a dwell period. The profile of the several cracks initiated in the oxide layer was disclosed by FIB cutting. The mechanism of the crack formation is principally similar to the SAGBO deterioration. The cracked protective oxide layer facilitates the access of the oxygen to the metal at the crack tip and local oxidation takes place. The localized oxidation of the material results in the formation of the V shaped grooves at the tip of the oxide cracks. Comparing to the oxidation of the grain boundaries arranged perpendicular to the stress axis; the oxidation rate is believed to be lower since in the vast majority of areas inspected only shallow oxide grooves developed in the material were observed. These notch-like grooves representing the potential nucleation sites were either dimmed or the growth of these cracks was significantly retarded since the macroscopic cracks from the grain boundaries already developed and led to the formation and propagation of a dominant crack. The initiation and the growth of environmentally assisted transgranular cracks have been recently documented by Fournier et al. [146] in a 9Cr-1Mo martensitic steel. It has been suggested that once the cracks are widely open and completely filled with the oxide intrusion, it cannot be stated unequivocally, whether the crack propagation rate is decreased or increased. In accord to the extraordinary cases, the crack could be considered as healed when filled with an oxide and only if the sufficient stress is applied, the oxide fracture may occur. Transgranular cracks commonly propagate as an oxide intrusion in straight manner in the material volume approximately perpendicularly to the stress axis as proposed by Fournier et al. [146], see Fig. 98.

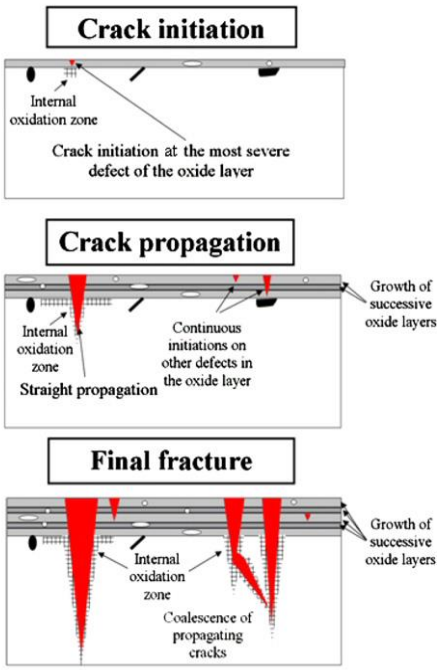

Fig. 98. Proposals of the mechanism of the early crack nucleation [146].

The examination of the electrolytically polished longitudinal cross-sections of the strained specimens subjected to IF and IF-D loading conditions enables to document the internal damage development as well as to identify the crack paths. When comparing the longitudinal cross-section of IF and IFD strained specimens, it was discovered that in the case of IF tests, the interior of the material is free of intergranular cracks while the cavities and cavity-induced

internal crack decorating the grain boundaries were found after IF-D loading. The cavities distributed along the grain boundaries are associated with the early stage of the creep damage. Typically, two types of the cavities turned out to be commonly present in the structural materials [98]: (i) cavities on the grain or lath boundaries and (ii) voids developed due to de-cohesion at the matrix/particle interphase. In low creep ductility material the grain boundary cavities develop in the early stages of the fatigue life whereas voids are formed generally later. The inspection of the longitudinal cross-section of the specimens subjected to IF-D loading revealed the formation of both types of these cavities, see Fig. 62 and Fig. 63.

The cavity formation is driven by the action of the tensile dwell predominantly at the grain boundaries. The cavities decorating the grain boundaries grow continuously by absorption of vacancies generated by mutual interaction of dislocations. Vacancies are produced by the annihilation of two opposite edge dislocations moving on neighbour planes or by non-conservative motion of jogs on screw dislocations. The early generation of the cavities is a precondition for the internal crack development, given that accumulation and coalescence of the cavities along the grain boundaries leads to the formation of the internal cracks (see Fig. 64). The area of the internal damage was found to be intensified primarily in the centre of the strained specimen. An EBSD inspection of the internal cracks developed in the specimen strained during the dwells revealed the intergranular propagation of the internal cracks. Bearing in mind that the specimens were studied at the end of the fatigue life and only intergranular internal cracks were spotted, it can be drawn that the solitary voids developed due to de-cohesion at the matrix/particle interphase do not have significant impact on internal creep damage evolution.

The inspection of well-developed long cracks initiated from the specimen surface revealed distinctive crack paths in the specimens subjected to IF and IF-D loading conditions. The transgranular crack propagation is dominant in specimens exposed to IF loading while IF-D procedures resulted in mixture of transgranular and intergranular crack growth. Nevertheless, based on the extensive investigation it turned out that the intergranular crack propagation prevails. It supports the importance of the essential effect of the time factor in propagation of fatigue cracks as well as the process of the dynamic embrittlement. IF straining resulted in crack initiation at the grain boundaries and the early intergranular crack growth but further propagation often follows crystallographic planes transgranularly, approximately perpendicular to the stress axis. The dwell introduced to the loading cycle at the peak strain stimulated the development of the creep damage. In accord with Zauter et al. [104], the wedge crack formation along with the cavity development needs plastic straining. Significant plastic straining takes place during the dwell period provided the peak temperature lies in the creep regime, especially when the material is exposed to dwell period in tension. The influence of the hold times was discussed in relation to the number of cycles to failure by Argence and Pineau [147] and Wareing [148]. Extension of the hold time generally resulted in the reduction of the fatigue life. Intergranular fracture was found to be more uniformly distributed throughout the volume of the material when increasing tensile hold time. The knowledge of internal damage based on the experimental investigation of the longitudinal cross-sections allowed clarifying the differences in fatigue lives of the specimens exposed to IF and IF-D loading conditions.

6.2.4 Damage evolution in thermomechanical fatigue loading

The dominant damage mechanism does vary with the TMF phase angle. Two extremal loading cycles were involved in the study of the damage evolution in the temperature range from 250 to 700 °C. The preferential grain boundary oxidation was found to be crucial in IP-TMF cyclic loading. The cracking of the oxidized grain boundaries represents the early nucleation sites as has been also observed in the case of the specimens subjected to isothermal fatigue with/without dwell in the loading cycle. In the principle, the potential damage mechanism can be estimated from the wave shape and the relation between the strain and the temperature alternation. The grain boundaries are preferentially oxidized during tensile part of the cycle close to the peak temperature. The oxidation processes are attributed to oxygen diffusion promoted by elevated temperature along with the tensile stress as similarly discussed in the case of the IF and IF-D tests. Once the oxidized grain boundary gets cracked, the crack remains open and exposed to the oxidizing atmosphere when specimen is subjected to tensile load at high temperature. Intensive oxidation takes place and the oxide developed gets cracked either in compression part of the loading cycle at decreasing temperature applied or during repeated tensile loading at increasing temperature. The early crack nucleation is reminiscent of that observed for isothermal fatigue with or without dwell introduced. In regards to TMF cycling, the grain boundary oxidation rate might be enhanced due to lower strain rate applied in TMF cycling comparing to isothermal fatigue. The outcome presented supports the crucial role of the environment along with the creep damage acting simultaneously during loading [112, 123, 149]. The decisive role of the grain boundary oxidation and cracking should be underlined when considering the further growth of the fatigue cracks following the grain boundaries in IP-TMF cycling. The inspection of the longitudinal cuts by means of EBSD technique fully supports the idea that crack paths follow the grain boundaries (see Fig. 77). The intergranular crack propagation was also reported by Kuwabara et al. [102] when performing IP-TMF procedure in the temperature range from 300 to 600 °C. Distinctive crack propagation was documented during IP-TMF in AISI 316L SS [150]. Combination of the intergranular and transgranular crack growth was recorded in the temperature range from 200 to 600 °C. Similarly, the transgranular crack propagation with crack initiation at the grain boundaries was reported by Christ [113] where AISI 304L was subjected to IP-TMF loading in temperature interval from 250 to 500 °C. Nevertheless, the dominant unique cracking mode can be clarified with respect to the peak temperature applied. Zauter et al. [104] discussed the effect of the maximum temperature of the loading cycle in relation to lifetime and crack growth as well. It was found that in relation to the peak temperature, two regimes may be identified, namely Low Temperature (LT) and High Temperature (HT) regime. During the LT regime, creep-fatigue is negligible, while in the HT regime, creep-fatigue is dominant and the transition between regimes is defined by the change in fracture mode from transgranular to intergranular. In addition to creep-fatigue damage, the environment effect is also crucial and cannot be neglected. The cracking of the oxidized grain boundaries observed may differ in IF and IP-TMF loading. There are two facts to be taken account. TMF procedures were conducted with lower strain rate than isothermal loading tests. The process of the grain boundary oxidation can be thus more enhanced in TMF cycling due to longer temperature exposure. Secondly, bearing in mind the temperature interval during TMF loading, the different ductility of the developed oxide due to temperature change needs to be considered as well. Since isothermal fatigue test were conducted at the constant temperature, the mechanical properties of the oxide intrusion

are believed to be the same during loading cycle. Due to the different ductility of the developed oxide layer, more brittle oxide in the low temperature is prone to be cracked when applying the tensile load at increasing temperature in IP-TMF straining. Different fracture behaviour was documented in the extensive study of the fracture mode in relation to the loading conditions imposed by Hormozi et al. on type 316 steel [112]. The specimens were exposed to symmetrical IF and IP-TMF loading conditions in temperature range from 500 to 650 °C. The fractographic and metallographic investigations revealed that in all IF and IP-TMF tests the cracks mostly initiated in transgranular mode and propagated in transgranular mode as well. Moreover, the study also showed the frequency related fracture mode. It was found that transgranular crack mode dominates at high frequencies while intergranular crack propagation is typical for low frequencies.

The process of the crack nucleation in OP-TMF loading is more complex. Since the specimen in compression is exposed to the maximum temperature in the loading cycle, the favoured oxidation of the grain boundaries is mostly suppressed. Even though the small fraction of the cracks developed at the grain boundaries was also observed, in overall, they do not play a significant role in the damage evolution in OP-TMF loading. This is supported by the EBSD imaging, where the well-developed cracks do not follow the grain boundaries, see Fig.78. Thus the oxide cracking along the grain boundaries does not reflect the effective dominant mechanism in terms of damage. In accord to experimental findings, it can be drawn that the principal crack developed in the uniform oxide layer. The following mechanism of the early crack formation has been suggested. The sufficient oxide layer on the material surface must develop in the first place at the peak temperature when the specimen is in compression. The uniform protective oxide layer prevents further oxidation. Since the oxide layer is brittle it gets cracked at minimum temperature, in the tensile part of the loading cycle. The cracks are nucleated randomly on the specimen surface and arranged perpendicularly to the stress axis. The incipient crack developed in the uniform oxide further propagates through the oxide layer and encounters the metal surface. Once the crack arrives to the metal the oxidation processes take place. Ongoing oxidation happens due to local access of the atmosphere to the metal surface when reaching the peak temperature in the OP-TMF cycle until the crack is fully closed during compression. Local oxidation and subsequent formation of the V-shaped oxide grooves is illustrated in Fig. 75. The V-shaped groove gets cracked in the tensile half-cycle at the decreasing temperature and the access of the oxidizing atmosphere is thus further promoted through the crack to the fresh metal surface. The alternation of these steps gives arise to initiation and propagation of the fatigue crack in oxidizing atmosphere driven by cyclic loading. Nevertheless, this damage mechanism is less effective comparing to grain boundary oxidation and cracking under IP-TMF conditions and results in considerable prolongation of the fatigue life. This can be attributed to the low oxidation rate of the crack since the crack is closed when the specimen in compression is exposed to the peak temperature.

The inspection of the crack paths in the interior of the specimens exposed to the IP-TMF along with the OP-TMF loading disclosed distinctive crack propagation. Whereas in the case of IP-TMF loading the intergranular crack propagation was found to be dominant, transgranular crack growth and crack branching is typical for OP-TMF. Intergranular crack propagation documented in specimens strained in IP-TMF loading is in accord with the mechanism of the preferential oxidation of the grain boundary and its subsequent cracking. Rather similar agreement between mechanism of the crack nucleation and crack propagation was

discovered after OP-TMF loading as well. Transgranular crack propagation is in accord to the suggested model of the random cracking of the uniform oxide layer and local preferential oxidation of the crack tip.

In summary four different tests were introduced in the study of the material subjected to TMF. Even more complex damage evolution is anticipated especially in the terms of the internal damage evolution enhanced by the tensile dwell period introduced to the loading cycle. In addition to fatigue damage, preferential grain boundary oxidation and cracking, the creep deterioration as well as creep-fatigue interaction may effectively operate as well. Preferential early grain boundary oxidation and cracking is a dominant feature for IPD-TMF loading similarly, to the previously discussed damage mechanisms identified on the specimens subjected to the IF, IF-D and IP-TMF. The early crack formation related to oxidation processes are promoted by the applied tensile stress. In accord to the SAGBO model, it can be anticipated that IPD-TMF loading might be even more crucial comparing to IP-TMF due to longer grain boundary exposure to the corrosive environment driven by the enhanced diffusion of the oxygen under tensile stress. Once the grain boundary gets cracked, the tensile dwell introduced at the peak strain level at elevated temperature can enhance the oxidation rate since the early developed crack remains open. The idea listed is just hypothetical and further thorough experimental investigation of this phenomenon is needed. The intensity of intergranular oxidation is not only temperature dependant but also changes for different types of grain boundaries [151]. The observation of the longitudinal cuts of the IPD-TMF strained specimens revealed the formation of the internal deterioration. The main damage is not only concentrated in close neighbourhood of the dominant crack but occurs rather uniformly distributed in the bulk of the material. The initial stages of the surface deformation and internal creep cavitation damage in the bulk of the material can exist side by side and evolve independently. Overall study of the specimens surface as well as of the interior indicates the synergic effect of the rapid intergranular surface crack formation driven by fatigue and crack propagation promoted by the enhanced oxidation due to hold time period as well as the creep damage in the form of intergranular internal cracks, see Fig. 88. The similar mechanism of the early grain boundary oxidation and cracking along with the evolution of the internal damage was also identified for isothermal fatigue with dwell in the loading cycle. Accordingly, the crack growth rate of the dominant crack is expected to be much higher comparing to IP-TMF due to linkage of the crack growing from the specimen surface with the internal cracks.

The specimen is exposed to the maximum temperature of the cycle for 10 min while in compression under OPD-TMF loading conditions. The surface of the specimen is mostly covered by the uniform oxide layer within the grains similarly to the specimens subjected to OP-TMF, see Fig.72 and Fig.83. The oxidation of the grain boundaries has been documented as well but in accord to the FIB and longitudinal cross-sections observations it turned out that cracking of the grain boundaries does not play the crucial role in terms of fatigue crack initiation. Once the critical thickness of the uniform surface oxide layer is reached, it gets cracked when the tensile load is applied at decreasing temperature. The cracking of the oxide layer is enhanced due to lower ductility of the developed oxide layer at minimum temperature in the cycle. The process of the early crack initiation is analogous to surface damage of the specimens strained under OP-TMF loading conditions. The crack proceeds through the oxide layer and encounters the material where local oxidation takes place. The process of the V-

shaped grooves formation typically observed during the investigation of the specimens subjected to OP-TMF is effective in the case of the OPD-TMF as well. Since the compressive stress acts during dwells at peak temperature, the cracks are not opened and the oxidation of the crack tip is suppressed. However, after 10 minutes dwell the crack is getting opened under the action of tensile stress and crack tip becomes exposed to the elevated temperature and the oxidation of the fresh material takes place. Moreover, the thickness of the uniform oxide islands within the grains increases in compression at peak temperature that may lead to the initiation of the new cracks when applying the tensile stress at decreasing temperature.

OPD-TMF loading resulted in higher fatigue life comparing to IPD-TMF straining. Dwell introduced into the loading cycle stimulated creep damage exclusively developed under IPD-TMF loading in accord to the SEM investigation. The study of the crack paths on the longitudinal cross-section supported the idea that the transgranular crack initiation and propagation is dominant in the case of OPD-TMF. Intergranular crack propagation documented in specimens strained in IPD-TMF loading is in accord with the mechanism of the preferential oxidation of the grain boundary and its subsequent cracking. Moreover, EBSD technique proved the internal intergranular deterioration in the bulk of the material. The low oxidation rate of the cracks in the case of OPD-TMF due to crack closure resulted in the extension of the fatigue life comparing to IPD-TMF where rapid and enhanced oxide cracking takes place and the crack growth of the dominant crack is accelerated by the internal damage. It can be concluded, that dwell introduced to TMF loading cycle enhanced effective damage mechanisms suggested. Influence of dwell times on the damage mechanism of a directionally solidified Ni-base superalloy was reported by Guth et al. [152]. Microtwin deformation occurred during OP-TMF loading and internal crack formation at carbides and carbide matrix/interfaces was identified in IP-TMF procedure. Dwells implemented enhanced both mechanisms resulting in the reduction of the fatigue life. Hormozi et al. [112] studied the effect of the dwell on the fracture mode. TMF procedures where a symmetrical hold time was introduced resulted in transgranular crack initiation and propagation in mixed mode. The presence of the intergranular cracking was considered as a consequence of the combined creep and oxidation effects. Transgranular crack initiation and propagation of the crack in transgranular mode was observed in IP-TMF without dwell implemented.

6.3 Fatigue life assessment under different types of loading conditions

Fatigue life of the material subjected to various loading conditions can be characterized using Coffin-Manson law. Accordingly, the plastic strain amplitude at half-life is plotted vs. number of cycles to fracture.

The reference tests include the specimens exposed to LCF loading conditions at room temperature as well as at 700 °C. Fig. 91a reveals that cyclic straining under IF conditions at 700 °C resulted in pronounced reduction in fatigue life for all saturated plastic strain amplitudes when compared to RT (around 50 times reduction). The reduction of the fatigue life for IF loading is in accord with the study of LCF behaviour of other materials [148]. The principal reason of this significant decrease in fatigue life is attributed to distinctive mechanisms of the crack development revealed by the study of the surface relief evolution as well as the mechanism of crack growth. The crack nucleation in room temperature cyclic

loading is associated with the pronounced localization of the cyclic plastic strain into PSBs and formation of the PSMs involving the extrusions and intrusions formation [111]. Localization of the cyclic plastic strain into the PSBs and formation of PSMs consisting of extrusions and intrusions has been also reported on 316L in RT cyclic loading [153, 154]. The fatigue cracks are initiated from the tip of the intrusions. Subsequent growth of the cracks developed results in linking with the other cracks till dominant crack occurs. Even though the localization of the cyclic plastic strain takes place in the very beginning of the cyclic loading in the majority of the grains the early crack initiation and propagation is slow process. The fatigue life is determined mostly by the growth rate of the short crack [155, 156]. The crack growth rate of short cracks at the RT cyclic loading is determined by the plastic strain amplitude [157]. Thus for low plastic strain amplitudes the crack growth is slow and leads to the long fatigue lives.

The scrutiny of the surface relief as well as interior of the specimen exposed to cyclic loading at 700 °C revealed no sign of the localization of the cyclic plastic strain into PSBs and the specimen surface was free of PSMs. Nevertheless, the observation of the specimen surface disclosed the dominant role of the environment under IF loading conditions. Preliminary studies suggested the enhanced oxidation of the grain boundaries associated with the decrease of the chromium content close to grain boundaries due to formation of the Cr-rich carbides [135]. Lower resistance to oxidation results in the preferential cracking of the oxidized grain boundaries arranged parallel to the loading axis. The effective SAGBO mechanism driven by cyclic straining plays significant role in the enhanced crack growth rate [139, 140, 141]. Moreover, the early initiation of the grain boundary crack and the enhanced crack growth rate caused by the linkage of the early developed cracks results in pronounced reduction of the fatigue life at elevated temperatures when compared to cyclic loading at room temperature.

Mason-Coffin fatigue life curves measured in IF and IF-D cyclic loading illustrate that introduction of the 10 min tensile dwell to the loading cycle leads to significant reduction of the fatigue life (see Fig. 91b). The reduction is associated with synergic effect of the fatigue damaged developed on the specimen surface and the internal creep damage. The crack initiation as well as crack propagation is believed to be more rapid in the case of IF-D since the SAGBO mechanism is time and temperature related. The internal creep deterioration in the form of gradual cavity condensation along the grain boundaries or already well-developed internal cracks stemmed from their coalescence was observed. The internal damage is stimulated by 10 min tensile dwell introduced to the loading cycle which results in the increase of the plastic strain amplitude. Higher plastic strain amplitude promotes the vacancy generation by interaction of the dislocations during stress relaxation. Moreover, the relaxation of the stress may lead to the early formation of cavities along the grain boundaries due to vacancy condensation or grain boundary sliding enhanced by 10 minutes tensile dwell. Higher rate of internal damage related to the increased plastic strain amplitude is in agreement with the slope divergence of the curves for IF and IF-D. Low plastic strain amplitudes result in rather similar fatigue lives for both loading procedures while the decrease of the fatigue life in IF-D is obvious for high plastic strain amplitudes. The significant difference in fatigue lives is due to higher production of point defects in IF-D cycling and their coagulation into cavities at high plastic strain amplitudes leading to the pronounced formation of the internal damage. When the path of the dominant fatigue crack encounters the creep damage area the mutual interaction leads to the increase of the dominant crack growth rate. The early intergranular

crack initiation and rapid fatigue crack growth results in lower fatigue life of specimens subjected to IF-D cyclic straining.

The thermomechanical loading conditions applied to the specimen significantly influence the fatigue life with respect to the isothermal loading at 700 °C, see Fig. 92a. OP-TMF cyclic loading resulted in prolonged fatigue lives when compared to IP-TMF tests and even to IF tests. The pronounced shift to the higher fatigue lives in OP-TMF cyclic loading can be reasonably discussed in relation to the examination of the surface of the tested specimens by means of SEM along with FIB cutting. Isothermal fatigue loading at 700 °C turned out to be less detrimental than IP-TMF loading and simultaneously more damaging than OP-TMF. Nevertheless, isothermal fatigue at 700 °C and OP-TMF loading led to identical fatigue lives for small saturated plastic strain amplitudes whereas for high saturated plastic strain amplitudes the fatigue lives in isothermal loading tend to approach to those in IP-TMF-cycling. The essential difference in fatigue life is related to the distinctive character of TMF loading cycles implemented. High growth rate of the fatigue crack and lower fatigue life in IP-TMF straining stems from the rapid oxidation of the grain boundaries during tension at the peak temperature. Different fatigue lives for IF and IP-TMF cycling can be also associated with different strain rates. Due to the longer temperature exposure of the specimen subjected to IP-TMF, grain boundary oxidation is assumed to be more pronounced and detrimental. It can also be expected that developed oxide at the grain boundaries is more susceptible to cracking at lower temperature during the temperature variations between 250 °C and 700 °C in IP-TMF loading than at constant temperature exposure like in the case of IF cycling. In OP-TMF cycling the crack initiation is delayed until the oxide layer is thick enough to be cracked. Considerable contribution to the lower fatigue life in IP-TMF straining is the high oxidation rate since the crack is fully opened during the tensile part of the loading cycle at the maximum temperature and the crack tip is exposed to the corrosive environment. Low oxidation rate is expected in OP-TMF cycling since the specimen at high temperature is in compression and cracks developed are closed. The retarded crack growth rate results in significant extension of the fatigue life compared to IP-TMF. In spite of the presence of negative stress in the IP-TMF cycling the fatigue life curves are shifted to the lower number of the cycles to fracture. This can be attributed to the principal differences of the loading conditions resulting in the modification of the damage evolution.

The fatigue life reduction of the specimens exposed to the TMF fatigue due to dwells introduced in maximum tension may be associated with various damage mechanisms, see Fig. 92b. In IPD-TMF cycling the dwell period introduced to the loading cycle at the peak load at maximum temperature enhances grain boundary oxidization and stimulates the internal damage evolution as reported in Fig. 88. The inspection of the surface of the specimen subjected to IPD-TMF supported the early crack development from the oxidized grain boundaries. The higher oxidation rate comparing to IP-TMF test is anticipated because the tensile load opens the crack up and crack tip is thus exposed to the corrosive environment during the tensile dwell for longer time than in IP-TMF cycling. The stress induced grain boundary oxidation and formation of the embrittled zone ahead of the crack tip during the dwells may facilitate crack propagation in the following cycles. Moreover, the study of the longitudinal cuts revealed the formation of the internal crack in the volume of the material in neighbourhood of well-developed surface cracks. The experimental findings from the longitudinal cut studies support the idea of the internal crack formation due to tensile dwell

introduced and moreover it indicates that the surface cracks link up with the internal damage and accelerate their crack growth rate. This holds true mostly for the region of the highest plastic strain amplitudes while for the lower plastic strain amplitudes the fatigue life for IP- and IPD-TMF is similar. The fatigue lives for OPD-TMF are much higher comparing to the fatigue lives under IP- and IPD-TMF loading conditions. Nevertheless, introduction of the dwell into OP-TMF cycle resulted in the increase of the plastic strain amplitude and simultaneously in lower fatigue lives than in OP-TMF loading. It can be anticipated that the uniform oxide layer in OPD-TMF cycling is formed earlier than in the case of OP-TMF since the specimen surface is exposed to the peak temperature for longer time period. The investigation of the surface of the specimens exposed to the OP- and OPD-TMF conditions disclosed principally the same mechanism of the crack initiation. Negative mean stress evolved during IP- and IPD-TMF does not lead to the extension of the fatigue life when compared to OP- and OP-TMF.

The fatigue life can be characterized also by the stress and plastic strain amplitudes at half-life. These values were used for plotting of the stress-strain curves (CSSCs) fitted by the power law. Fatigue hardening coefficient *K'* along with fatigue hardening exponent *n'* were evaluated using least square fitting and are listed in Table. 8. Fig. 99 illustrates cyclic stress-strain curves for all the experiments conducted. CSSC at room temperature is substantially below the curve evaluated for 700 °C loading. The shift of the CSSC at 700 °C to higher values of stress amplitude comparing to room temperature loading is related to the changes of the material microstructure at these temperatures during cycling. While the high density of the dislocations along with the formation of the strain-induced NbC particles as well as Cu-rich particles leads to extraordinary hardening during cyclic loading at 700 °C [14, 112], the localization of the plastic strain into PSBs results in cyclic softening during room temperature straining.

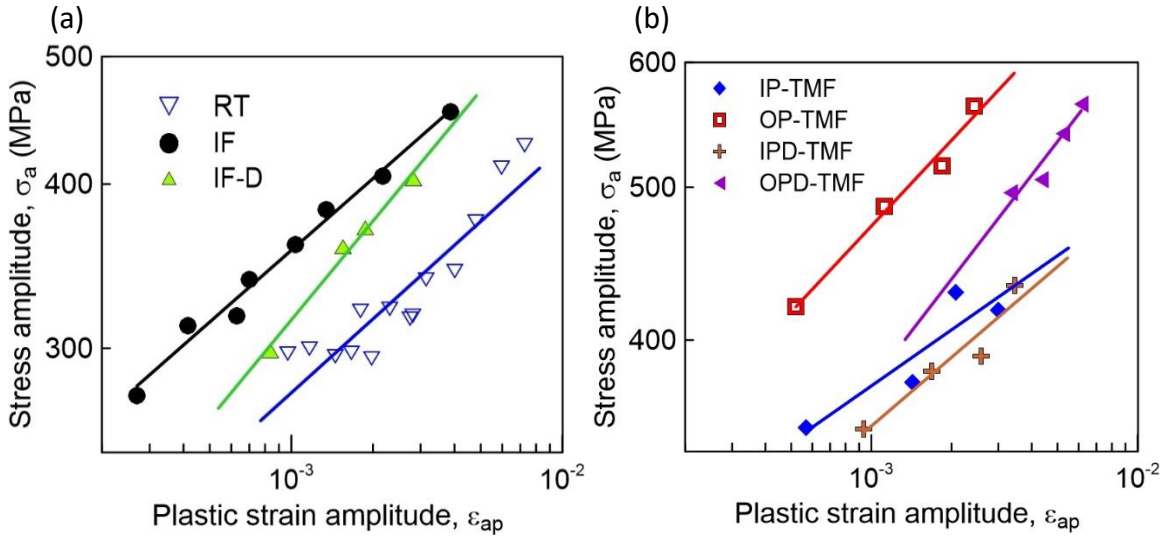

Fig. 99. Cyclic stress–strain curves for all loading conditions.

The introduction of the tensile dwell into the loading cycle results in the shift of the CSSC to the lower stress amplitudes. Introduction of the tensile dwell into the loading cycle results in the broadening of the hysteresis loop i.e in the increase of the plastic strain amplitude. Thus,

for given stress amplitude, the plastic strain amplitude in IF-D the test is higher when compared to the IF corresponding to the shift of the CSSC as documented in Fig. 99a.

Test	K' (MPa)	n'	ε'_f	C
RT	1006	0.186	0.694	-0.525
HT(IF)	1244	0.181	0.211	-0.649
HTD(IF-D)	1768	0.250	0.0316	-0.452
IP-TMF	846	0.118	0.619	-0.952
OP-TMF	1646	0.181	2.3996	-0.887
IPD-TMF	959	0.145	0.115	-0.714
OPD-TMF	2931	0.323	0.427	-0.663

Tab.8. Low cycle fatigue parameters of Sanicro 25 steel under different loading conditions.

Fig. 99b documents the situation for thermomechanical fatigue tests with and without dwells. The CSSC for OP-TMF loading lies well above that for IP-TMF loading. Pronounced saturation of the stress amplitude occurred only in OP-TMF loading, while the premature fracture of the specimens subjected to IP-TMF cycling led to substantially lower fatigue lives and saturation of the stress amplitude is not reached. The stress amplitude at half-life is thus substantially higher in the case of OP-TMF cycling compared to IP-TMF cycling. The tendency of the early stress amplitude saturation is pronounced during OPD-TMF as well. IPD-TMF loading exhibits cyclic hardening and it is followed by cyclic softening at the end of the fatigue life. Similarly to TMF cycling without dwell period the CSSC for OPD-TMF is higher than in the case of IPD-TMF. The shift of the CSSCs for IPD- and OPD-TMF in relation to IP- and OP-TMF can be correlated with the change of the loading cycle when imposing the dwell period. Introduction of the tensile dwell into the loading cycle leads to the increase of the plastic strain amplitude. Given that, for distinctive levels of the stress amplitude, the plastic strain amplitude in cycling without dwell is lower when compared to the procedures with dwell in the loading cycle.

7. Conclusions

The extensive and complex experimental investigation of the mechanical behaviour along with the damage mechanism assessment in relation to various type of the loading cycle was performed. The following conclusions can be drawn.

Room temperature cyclic loading

Cyclic response

- Cyclic softening is typical for room temperature cyclic loading. Nevertheless, for the total strain amplitude higher than 5×10^{-3} the material manifests the cyclic hardening from the onset of the straining followed by cyclic softening.
- The pronounced cyclic softening is given by the localization of the cyclic plastic strain into the PSBs in the interior of the material. PSBs manifest as a PSMs when emerging from the interior and forming the surface traces.

Analysis of the hysteresis loop shape

- The early stages of the fatigue life give a rise to two peaks characterizing the probability density function of the internal critical stresses. The first peak represents the volumes of the localized cyclic plastic strain and the second peak reflects the microvolumes of the matrix.
- The second peak gradually faded during cyclic loading and the first peak was shifted to lower fictive stresses. This behaviour indicates the complete localization of the cyclic plastic strain into PSBs.

Damage mechanism

- Cyclic plastic strain is localized into the individual PSBs resulting in the formation and continuous evolution of the PSMs in the early stages of fatigue life.
- The surface relief exhibits multiple occurrences of the PSMs typically consisting of extrusions and intrusions. PSMs profiles exhibit high variability of the PSMs shapes.
- The extrusions and intrusions develop during cyclic loading. In majority of the cases extrusions grow and intrusions typically deepen. Stage I crack develops from the tip of the deepest intrusion.

Isothermal fatigue loading at 700°C

Cyclic response

- Isothermal fatigue at elevated temperature resulted in pronounced cyclic hardening for all the total strain amplitudes applied. The rate of the cyclic hardening increases with increasing strain amplitude.
- The significant cyclic hardening is associated with rapid growth of dislocation density related to the enhanced cross-slip promoted by elevated temperature and with

formation of the incoherent NbC and Cu-rich particles hindering the dislocation motion.

Statistical theory analysis

- Single peak of the probability density function of the internal critical stresses was found in the beginning of the cyclic loading. During cyclic straining it broadens and shifts to higher fictive stresses.
- The evolution of the distribution function corresponds to material strengthening driven by the growing dislocation density and it is enhanced due to interaction of the dislocations with the incoherent NbC and coherent Cu-rich precipitates.

Damage mechanism

- The environmental effects are crucial in regards to the early surface crack formation under isothermal fatigue loading conditions at 700 °C.
- Preferential oxidation of the grain boundaries and formation of the oxide intrusions play decisive role in the crack nucleation during the cyclic loading at 700°C.
- Tensile dwell in the loading cycle stimulates the oxidation and cracking of the oxidized grain boundaries along with the cavity nucleation in the interior of the material. Cavity nucleation along the grain boundaries leads to internal cracks formation and acceleration of the crack growth.

Thermomechanical fatigue loading in temperature range 250-700°C

Cyclic response

- Cyclic hardening is typical regardless of the loading cycle introduced. Pronounced saturation of the stress amplitude occurred only in OP-TMF and OPD-TMF loading.
- Cyclic stress-strain curves depend on the phase shift between the strain and temperature.

Damage mechanism

- Two basic mechanisms contribute to the cracking in TMF cycling (i) in IP-TMF cycling; the cracking of the oxidized grain boundaries under action of cyclic loading and growth along the grain boundaries, (ii) in OP-TMF cycling; cracking of the thick oxide layer, local oxide attack and transgranular crack growth.
- The environmental effects and time factor are crucial in terms of the damage evolution under TMF loading conditions. Dwell in the cycle increases the intensity of the fatigue damage.

8. References

[1] R. Viswanathan, K. Coleman, U. Rao, Materials for ultra-supercritical coal-fired power plant boilers, International journal of pressure vessels and piping 83, 2006, pp. 778-783

[2] H.C. Furtado, I.L. May, High temperature degradation in power plants and refineries, Materials Research 7, 2004, pp. 103-110

[3] G. Chai, M. Boström, M. Olaison, U. Forsberg, Creep and LCF behaviours of newly developed advanced heat resistant austenitic stainless steel for A-USC, Procedia Engineering 55, 2013, pp. 232-239

[4] https://www.materials.sandvik/en/products/tube-pipe-fittings-and-flanges/high-performance-materials/high-temperature-stainless-steels/sanicro-25/

[5] M.F. McGuire, Stainless steels for design engineers, ASM International, 2008, pgs. 296

[6] F.B. Pickering, Physical mettallurgical developments of stainless steels, Institute of Metals book, Stainless steels 84, 1985, pp. 2-28

[7] K.H. Lo, C.H. Shek, J.K.L. Lai, Recent developments in stainless steels, Materials Science and Engineering: R: Reports 65, 2009, pp. 39-104

[8] T. Sourmail, Precipitation in creep resistant austenitic stainless steels, Materials Science and Technology 17, 2001, pp. 1-14

[9] A.F. Padilha, D.M. Escriba, E. Materna-Morris, M. Rieth, M. Klimenkov, Precipitation in AISI 316L(N) during creep tests at 550 and 600 °C up to 10 years, Journal of Nuclear Materials 362, 2007, pp. 132-138

[10] P. Marshall, Austenitic stainless steels - Microstructure and mechanical properties, Springer Netherlands, 1984, pgs. 432

[11] T.L. Burnett, R. Geurts, H. Jazaeri, S.M. Northover, S.A. McDonald, S.J. Haigh, P.J. Bouchard, P.J. Withers, Multiscale 3D analysis of creep cavities in AISI type 316 stainless steel, Materials Science and Technology 31, 2015, pp. 522-534

[12] M.H. Lewis, B. Hattersley, Precipitation of $M_{23}C_6$ in austenitic steels, Acta Metallurgica 13, 1965, pp. 1159-1168

[13] F.R. Beckitt, B.R. Clark, The shape and mechanism of formation of $M_{23}C_6$ carbide in austenite, Acta Metallurgica 15, 1967, pp. 113-129

[14] M. Heczko, B.D. Esser, T.M. Smith, P. Beran, V. Mazánová, T. Kruml, J. Polák, M.J. Mills, On the origin of extraordinary cyclic strengthening of the austenitic stainless steel Sanicro 25 during fatigue at 700 degrees C, Journal of Materials Research 32, 2017, pp. 4342-4353

[15] D.H. Jack, K.H. Jack, Structure of Z–Phase, NbCrN, Journal of the Iron and Steel Institute 210, 1972, pp. 790-792

[16] P.W. Robinson, D.H. Jack, Precipitation of Z phase in a high-nitrogen stainless steel, Journal of Heat Treating 4, 1985, pp. 69-74

[17] H.K. Danielsen, J. Hald, F.B. Grumsen, M.A.J. Somers, On the crystal structure of Z-Phase Cr(V,Nb)N, Metallurgical and Materials Transactions A 37, 2006, pp. 2633-2640

[18] M. Schwind, J. Källqvist, J.-O. Nilsson, J. Ågren, H.-O. Andrén, σ–Phase precipitation in stabilized austenitic stainless steels, Acta Materialia 48, 2000, pp. 2473-2481

[19] D.J. Li, Y. Gao, J.L. Tan, F.G. Wang, J.S. Zhang, Effect of σ–phase on the creep properties of Cr25Ni20 stainless steel, Scripta Metallurgica 23, 1989, pp. 1319-1321

[20] J.K. Lai, A. Wickens, Microstructural changes and variations in creep ductility of 3 casts of type 316 stainless steel, Acta Metallurgica 27, 1979, pp. 217-230

[21] C.J. McMahon Jr., On the mechanisms of creep damage in type 316 stainless steel, Scripta Metallurgica 19, 1985, pp. 733-737

[22] Y. Minami, H. Kimura, Y. Ihara, Microstructural changes in austenitic stainless steels during long-term aging, Materials Science and Technology 2, 1986, pp. 795-806

[23] H. Semba, H. Okada, M. Igarashi, Creep properties and strengthening mechanisms in 23Cr-45Ni-7W (HR6W) alloy and Ni-base superalloys for 700 °C A-USC boilers, Advances in Materials Technology for Fossil Power Plants: Proceedings from the 5th International Conference, 2008, pp. 168-184

[24] J.M. Wheeldon J.P. Shingledecker, Chapter: Materials for boilers operating under supercritical steam conditions, Book: Ultra-Supercritical Coal Power Plants: Materials, Technologies and Optimisation, Woodhead Publishing, 2013, pp. 81-103

[25] J. Polák, Cyclic plasticity and low cycle fatigue life of metals, Prague/Amsterdam: Academia/Elsevier 63, 1991, pgs. 316

[26] M. Bílý, Cyclic deformation and fatigue of metals, Elsevier Science 78, 1993, pgs. 372

[27] M. Klesnil, P. Lukáš, Fatique of metallic materials, Elsevier Science 71, Prague: Academia, 1992, pgs. 270

[28] S.S. Manson, Behaviour of materials under conditions of thermal stress, NACA Annual Report 40, 1954, pp. 317-350

[29] L.F. Coffin, A study of the effect of cyclic thermal stresses on a ductile metal, Transactions of the American Society of Mechanical Engineers 76, 1954, pp. 931-950

[30] J. Polák, F. Fardoun, S. Degallaix, Effective and internal stresses in cyclic straining of 316 stainless steel, Materials Science and Engineering A 215, 1996, pp. 104-112

[31] J. Polák, M. Klesnil, The hysteresis loop 1. A statistical theory, Fatigue of Engineering Materials and Structures 5, 1982, pp. 19-32

[32] J.L. Chaboche, A review of some plasticity and viscoplasticity constitutive theories, International Journal of Plasticity 24, 2008, pp. 1642-1693

[33] M. Abdel-Karim, A. Khan, Cyclic multiaxial and shear finite deformation responses of OFHC Cu. Part II: An extension to the KHL model and simulations, International Journal of Plasticity 26, 2010, pp. 758-773

[34] P. Evrard, I. Alvarez-Armas, V. Aubin, S. Degallaix, Polycrystalline modelling of the cyclic hardening/softening behavior of an austenitic–ferritic stainless steel, Mechanics of Materials 42, 2010, pp. 395-404

[35] B. Lin, L.G. Zhao, J. Tong, H.-J. Christ, Crystal plasticity modelling of cyclic deformation for a polycrystalline nickel-based superalloy at high temperature, Materials Science and Engineering A 527, 2010, pp. 3581-3587

[36] G. Masing, Zur Heyn'schen Theorie der Verfestigung der Metalle durch verborgene elastische Spannungen, Wissenschaftliche Veroffentlichung aus dem Siemens-Konzern 3, 1923, pp. 231-239

[37] N.N. Afanasjev, Statistical theory of fatigue strength of metals, Academy of Sciences USSR, 1953

[38] M. Petrenec, J. Polák, J. Tobiáš, M. Šmíd, A. Chlupová, R. Petráš, Analysis of cyclic plastic response of nickel based IN738LC superalloy, International Journal of Fatigue 65, 2014, pp. 44-50

[39] D. Kuhlmann-Wilsdorf, C. Laird, Dislocation behavior in fatigue II. Friction stress and back stress as inferred from an analysis of hysteresis loops, Materials Science and Engineering 37, 1979, pp. 111-120

[40] J. Polák, R. Petráš, Chapter: Hysteresis loop analysis in cyclically strained materials, Book: Inelastic Behaviour of Materials and Structures Under Monotonic and Cylic Loading, Springer International Publishing, 2015, pp. 185-205

[41] H.-J. Christ, Is thermomechnical fatigue life predictable?, Procedia Engineering 55, 2013, pp. 181-190

[42] H.-J. Christ, Thermomechanical fatigue - Mechanism-based considerations on the challenge of life assessment, MATEC Web of Conferences 165, 2018

[43] J.A. Ewing, J.C.W. Humfrey, The fracture of metals under repeated alternations of stress, Philosophical Transactions of the Royal Society A 200, 1903, pp. 241-250

[44] W.A. Wood, Formation of fatigue cracks, Philosophical Magazine 3, 1958, pp. 692-699

[45] A.H. Cottrell, D. Hull, Extrusion and intrusion by cyclic slip in copper, Proceedings of the Royal Society of London. Series A, Mathematical and Physical Sciences 242, 1957, pp. 211-213

[46] D.F. Watt, A mechanism for the production of intrusions and extrusions during fatigue, The Philosophical Magazine 14, 1966, pp. 87-92

[47] E.E. Laufer, W.N. Roberts, Dislocation structures in fatigued copper single crystals, The Philosophical Magazine 10, 1964, pp. 883-886

[48] P. Lukáš, M. Klesnil, J. Krejčí, Dislocations and persistent slip bands in copper single crystals fatigued at low strain amplitude, Physica Status Solidi 27, 1968, pp. 545-552

[49] J.G. Antonopulos, L.M. Brown, A.T. Winter, Vacancy dipoles in fatigued copper, The Philosophical Magazine 34, 1976, pp. 549-563

[50] J. Polák, Electrical resistivity of cyclically deformed copper, Czechoslovak Journal of Physics B 19, 1969, pp. 315-322

[51] J. Polák, The effect of intermediate annealing on the electrical resistivity and shear stress of fatigued copper, Scripta Metallurgica 4, 1970, pp. 761-764

[52] J. Polák, Resistivity of fatigued copper single crystals, Materials Science and Engineering 89, 1987, pp. 35-43

[53] Z.S. Basinski, S.J. Basinski, Electrical resistivity of fatigued copper crystals, Acta Metallurgica 37, 1989, pp. 3275-3281

[54] U. Essmann, U. Gösele, H. Mughrabi, A model of extrusions and intrusions in fatigued metals I. Point-defect production and the growth of extrusions, Philosophical Magazine A 44, 1981, pp. 405-426

[55] K. Differt, U. Essmann, H. Mughrabi, A model of extrusions and intrusions in fatigued metals. Part II: surface roughening by random irreversible slip, Philosophical Magazine A 54, 1986, pp. 237-258

[56] H. Mughrabi, Cyclic slip irreversibilities and the evolution of fatigue damage, Metallurgical and Materials Transactions A 40, 2009, pp. 1257-1279

[57] J. Polák, On the role of point defects in fatigue crack initiation, Materials Science and Engineering 92, 1987, pp. 71-80

[58] J. Polák J, Chapter: Cyclic deformation, crack initiation, and low-cycle fatigue, Book: Comprehensive structural integrity, Amsterdam: Elsevier, 2003, pp. 1-39

[59] J. Polák, J. Man, Fatigue crack initiation – The role of point defects, International Journal of Fatigue 65, 2014, pp. 18-27

[60] J. Polák, J. Man, Experimental evidence and physical models of fatigue crack initiation, International Journal of Fatigue 91, 2016, pp. 294-303

[61] J. Polák, J. Man, Mechanisms of extrusion and intrusion formation in fatigued crystalline material, Materials Science and Engineering A 596, 2014, pp. 15-24

[62] J. Polák, M. Sauzay, Growth of extrusions in localized cyclic plastic straining, Materials Science and Engineering A 500, 2009, pp. 122-129

[63] H. Mughrabi, R. Wang, K. Differt, U. Essmann, Chapter: Fatigue crack initiation by cyclic slip irreversibilities in high-cycle fatigue, Book: Fatigue Mechanisms: Advances in Quantitative Measurement of Physical Damage, ASTM International, 1983, pp. 5-45

[64] M. Bayerlein, H. Mughrabi, Chapter: Fatigue crack initiation and early crack growth in copper polycrystals - effects of temperature and environment, Book: Short Fatigue Cracks, Mechanical Engineering Publications, London, 1992, pp. 55–82.

[65] J. Polák, J. Man, T. Vystavěl, M. Petrenec, The shape of extrusions and intrusions and initiation of stage I fatigue crack, Materials Science and Engineering A 517, 2009, pp. 204-211

[66] J. Polák, I. Kuběna, J. Man, The shape of early persistent slip markings in fatigued 316L steel, Materials Science and Engineering A 564, 2013, pp. 8-12

[67] J. Polák, R. Petráš, G. Chai, V. Škorík, Surface profile evolution and fatigue crack initiation in Sanicro 25 steel at room temperature, Materials Science and Engineering A 658, 2016, pp. 221-228

[68] M. Risbet, X. Feaugas, C. Guillemer-Neel, M. Clavel, Use of atomic force microscopy to quantify slip irreversibility in a nickel-base superalloy, Scripta Materialia 49, 2003, pp. 533-538

[69] M. Risbet, X. Feaugas, Some comments about fatigue crack initiation in relation to cyclic slip irreversibility, Engineering Fracture Mechanics 75, 2008, pp. 3511-3519

[70] J. Polák, J. Man, K. Obrtlík K, AFM evidence of surface relief formation and models of fatigue crack nucleation, International Journal of Fatigue 25, 2003, pp. 1027-1036

[71] J. Polák, V. Mazánová, M. Heczko, R. Petráš, I. Kuběna, L. Casalena, J. Man, The role of extrusions and intrusions in fatigue crack initiation, Engineering Fracture Mechanics Volume 185, 2017, pp. 46-60

[72] J. Polák, V. Mazánová, R. Petráš, M. Heczko, Early damage and fatigue crack initiation at ambient and elevated temperatures in heat resistant austenitic steel, MATEC Web of Conferences 165, 2018

[73] P.J.E. Forsyth, A two stage process of fatigue crack growth, Symposium on Crack Propagation, 1961, pp. 76-79

[74] P.J.E. Forsyth, Fatigue damage and crack growth in aluminium alloys, Acta Metallurgica 11, 1963, pp. 703-715

[75] C. Laird, G.C. Smith, Initial stages of damage in high stress fatigue in some pure metals, Philosophical Magazine 8, 1963, pp. 1945-1963

[76] C. Laird, Chapter: The influence of metallurgical structure on the mechanisms of fatigue crack propagation, Book: Fatigue Crack Propagation, ASTM International, 1967, pp. 131-168

[77] A.Ya. Krasovskii, Mechanisms of fatigue crack propagation in metals, Strength of Materials 12, 1980, pp. 1255-1263

[78] C.Q. Bowles, A study of the crack tip geometry resulting from fatigue crack propagation in air and vacuum, Delft University of Technology, Department of Aerospace Engineering, Report LR-261, 1978

[79] A.J. Krasowsky, V.A. Stepanenko, A quantitative stereoscopic fractographic study of the mechanism of fatigue crack propagation in nickel, International Journal of Fracture 15, 1979, pp. 203-215

[80] P. Rodriguez, K. Bhanu Sankara Rao, Nucleation and growth of cracks and cavities under creep-fatigue interaction, Progress in Materials Science 37, 1993, pp. 403-480

[81] A.N. Stroh, The formation of cracks in plastic flow. II, Proceedings of the Royal Society A 232, 1955, pp. 548-560

[82] J.O. Stiegler, K. Farrell, B.T.M. Loh, H.E. McCoy, Nature of creep cavities in tungsten, American Society for Metals Transactions Quarterly 60, 1967, pp. 494-503

[83] S. Baik, R. Raj, Wedge type creep damage in low cycle fatigue, Metallurgical Transactions A 13, 1982, pp. 1207-1214

[84] H.E. Evans, The growth of creep cavities by grain boundary sliding, The Philosophical Magazine 23, 1971, pp. 1101-1112

[85] C.J. McMahon Jr., On the mechanism of premature in-service failure of nickel-base superalloy gas turbine blades, Materials Science and Engineering 13, 1970, pp. 295-297

[86] U. Krupp, W. Kane, J. A. Pfaendtner, X. Liu, C. Laird, C. J. McMahon Jr., Oxygen-induced intergranular fracture of the nickel-base alloy IN718 during mechanical loading at high temperatures, Materials Research 7, 2004, pp. 35-41

[87] J. Pfaendtner, C.J. McMahon Jr., Oxygen-induced intergranular cracking of Ni-base alloy at elevated temperatures - An example of dynamic embrittlement, Acta Materialia 49, 2001, pp. 3369-3377

[88] R.C. Muthiah, J.A. Pfaendtner, S. Ishikawa, C.J. McMahon Jr., Tin-induced dynamic embrittlement of Cu–7% Sn bicrystals with a Σ5 boundary, Acta Materialia 47, 1999, pp. 2797-2808

[89] D. Bika, J.A. Pfaendtner, M. Menyhard, J.C. McMahon Jr., Sulfur-induced dynamic embrittlement in a low-alloy steel, Acta Metallurgica et Materialia 43, 1995, pp. 1895-1908

[90] R. Muthiah, A. Guha, C.J. McMahon Jr., An example of dynamic embrittlement: oxygen-induced cracking of a Cu-Be alloy at 200°C, Materials Science Forum Vols. 207-209, 1996, pp. 585-588

[91] S. Dymek, M. Dollar, M. Wrobel, Environmentally assisted dynamic embrittlement in a long range ordered Ni-Mo-Cr Alloy, Scripta Materialia 43, 2000, pp. 343-348

[92] C.T. Liu, C.L. White, Dynamic embrittlement of boron-doped Ni3Al alloys at 600°C, Acta Metallurgica 35, 1987, pp. 643-649

[93] S. Suresh, R.O. Ritchie, Proc. International Conference on Fracture 5, Cannes, 1981, pp. 1873-1680

[94] M.L. Karasek, Materials engineering-mechanical behavior, Report No. 132, College of Engineering, University of Illinois at Urbana-Champaign, 1986

[95] R. W. Neu, Huseyin Sehitoglu, Thermomechanical fatigue, oxidation, and Creep: Part II. Life prediction, Metallurgical Transactions A 20, 1989, pp. 1769-1783

[96] M. Gerland, R. Alain, B. Ait Saadi, J. Mendez, Low cycle fatigue behaviour in vacuum of a 316L-type austenitic stainless steel between 20 and 600°C Part II: dislocation structure evolution and correlation with cyclic behaviour, Materials Science and Engineering A 229, 1997, pp. 68-86

[97] D.W. Kim, W.-S. Ryu, J. H. Hong, S.-K. Choi, Effect of nitrogen on high temperature low cycle fatigue behaviors in type 316L stainless steel, Journal of Nuclear Materials 254, 1998, pp. 226-233

[98] S. Holdsworth, Creep fatigue failure diagnosis, Materials (Basel) 8, 2015, pp. 7757-7769

[99] R. Hales, A quantitative metallographic assessment of structural degradation of type 316 stainless steel during creep-fatigue, Fatigue & Fracture of Engineering Materials & Structures 3, 1980, pp. 339-356

[100] J.B. Conway, R.H. Stentz, J.T. Berling, Fatigue, tensile, and relaxation behaviour of stainless steels, US Atomic Energy Commission Report TID-26135, 1975

[101] K. Yamaguchi, K. Kanazawa, Effect of strain wave shape on high temperature fatigue life of a type 316 steel and application of the strain range partitioning method, Metallurgical Transactions A 11, 1980, pp. 2019-2027

[102] K. Kuwabara, A. Nitta, Thermal-mechanical low-cycle fatigue under creep-fatigue interaction on type 304 stainless steel, Fatigue & Fracture of Engineering Materials & Structures 2, 1979, pp. 293-304

[103] D.W. Kim, J.H. Chang, W.S. Ryu, Evaluation of the creep–fatigue damage mechanism of type 316L and type 316LN stainless steel, International Journal of Pressure Vessels and Piping 85, 2008, pp. 378-384

[104] R. Zauter, H.-J. Christ, H. Mughrabi, Some aspects of thermomechanical fatigue of AISI 304L stainless steel: Part I. Creep-fatigue damage, Metallurgical and Materials Transactions A 25, 1994, pp. 401-406

[105] R. Raj, M.F. Ashby, Intergranular fracture at elevated temperature, Acta Metallurgica 23, 1975, pp. 653-666

[106] W.D. Nix, Mechanisms and controlling factors in creep fracture, Materials Science and Engineering A 103, 1988, pp. 103-110

[107] H.L. Bernstein, C. Amzallag, N.J. Leis, P. Rabbe, Low-cycle fatigue and life prediction, American Society for Testing and Materials, 1982, pp. 105-134

[108] F. Ellyin, Fatigue damage, crack growth and life prediction, Chapman& Hall, London, 1997

[109] A. Nitta, K. Kuwabara, Thermal-mechanical fatigue failure and life prediction, Current Japanese Materials Research 3, 1988, pp. 203-222

[110] K. Kuwabara, A. Nitta, Effect of strain hold time of high temperature on thermal fatigue of type 304 stainless steel, ASME-MPC symposium on creep–fatigue interaction, American Society of Mechanical Engineers, 1976, pp. 161-177

[111] H.J. Shi, Z.G. Wang, H.H. Su, Thermomechanical fatigue of a 316L austenitic steel at two different temperature intervals, Scripta Materialia 35, 1996, pp. 1107-1113

[112] R. Hormozi, F. Biglari, K. Nikbin, Experimental study of type 316 stainless steel failure under LCF/TMF loading conditions, International Journal of Fatigue 75, 2015, pp. 153-169

[113] H.-J. Christ, Effect of environment on thermomechanical fatigue life, Materials Science and Engineering A 468–470, 2007, pp. 98-108

[114] M. Heczko, J. Polák, T. Kruml, Microstructure and dislocation arrangements in Sanicro 25 steel fatigued at ambient and elevated temperatures, Materials Science & Engineering A 680, 2017, pp. 168-181

[115] P. Hähner, E. Affeldt, T. Beck, H. Klingelhöffer, M. Loveday, C. Rinaldi, Validated code-of-practice for strain-controlled thermo-mechanical fatigue testing, European Communities, 2006

[116] J.-B. Vogt, Fatigue properties of high nitrogen steels, Journal of Materials Processing Technology 117, 2001, pp. 364-369

[117] B. Chang, Z. Zhang, Cyclic deformation behavior in a nitrogen-alloyed austenitic stainless steel in terms of the evolution of internal stress and microstructure, Materials Science and Engineering A 556, 2012, pp. 625-632

[118] J. Polák, V. Mazánová, M. Heczko, I. Kuběna, J. Man, Profiles of persistent slip markings and internal structure of underlying persistent slip bands, Fatigue & Fracture of Engineering Materials & Structures 40, 2017, pp. 1101-1116

[119] D. Caillard, J.L. Martin, Thermally activated mechanisms in crystal plasticity, Elsevier, Oxford, 2003

[120] J. Polák, R. Petráš, M. Heczko, I. Kuběna, T. Kruml,G. Chai, Low cycle fatigue behavior of Sanicro25 steel at room and at elevated temperature, Materials Science and Engineering A 615, 2014, pp. 175-182

[121] M. Heczko, B.D. Esser, T.M. Smith, P. Beran, V. Mazánová, D.W. McComb, T. Kruml, J. Polák, M.J. Mills, Atomic resolution characterization of strengthening nanoparticles in a new high-temperature-capable 43Fe-25Ni-22.5Cr austenitic stainless steel, Materials Science and Engineering A 719, 2018, pp. 49-60

[122] K. Rau, T. Beck, D. Lohe, Isothermal, thermal/mechanical and complex thermal/mechanical fatigue tests on AISI 316L steel—a critical evaluation, Materials Science and Engineering A 345, 2003, pp. 309-318

[123] A. Nagesha, M. Valsan, R. Kannan, K. Bhanu Sankara Rao, V. Bauer, H.-J. Christ, V. Singh, Thermomechanical fatigue evaluation and life prediction of 316L(N) stainless steel, International Journal of Fatigue 31, 2009, pp. 636-643

[124] A. Nagesha, R. Kannan, P. Parameswaran, R. Sandhya, K. Rao, V. Singh, A comparative study of isothermal and thermomechanical fatigue on type 316L(N) austenitic stainless steel Materials Science and Engineering A 527, 2010, pp. 5969-5975

[125] M. Ramesh, H.J. Leber, K.G.F. Jenssens, M. Diener, R. Spolenak, Thermomechanical and isothermal fatigue behavior of 347 and 316L austenitic stainlees steel tube and pipe steels International Journal of Fatigue 33, 2011, pp. 683-691

[126] R. Kolmorgen, H. Biermann, Thermo-mechanical fatigue behaviour of a duplex stainless steel, International Journal of Fatigue 37, 2012, pp. 86-91

[127] R. Kolmorgen, H. Biermann, Thermo-mechanical fatigue behaviour of a duplex stainless steel in the range 350–600 °C, International Journal of Fatigue 65, 2014, pp. 2-8

[128] J. Man, K. Obrtlík, J. Polák, Extrusions and intrusions in fatigued metals. Part 1. State of the art and history, Philosophical Magazine A 89, 2009, pp. 1295-1336

[129] M.D. Sangid, The physics of fatigue crack initiation, International Journal of Fatigue 57, 2013, pp. 58-72

[130] D. Antolovich, R.W. Armstrong, Plastic strain localization in metals: origins and consequences, Progress in Materials Science 59, 2014, pp. 1-160

[131] H. Mughrabi, Microstructural mechanisms of cyclic deformation, fatigue crack initiation and early crack growth, Philosophical Transactions of the Royal Society A 373, 2015

[132] U. Essmann, U. Gosele, H. Mughrabi, A model of extrusions and intrusions in fatigued metals I. Point-defect production and the growth of extrusions, Philosophical Magazine A 44, 1981, pp. 405-426

[133] A. Hunsche, P. Neumann, Quantitative measurement of persistent slip band profiles and crack initiation, Acta Metallurgica 34, 1986, pp. 207-217

[134] H. Mughrabi, Damage mechanisms and fatigue lives: from the low to the very high cycle regime, Procedia Engineering 55, 2013, pp. 636-644

[135] A.T. Winter, O.R. Pedersen, K.V. Rasmussen, Dislocation microstructures in fatigued copper polycrystals, Acta Metallurgica 29, 1981, pp. 735-748

[136] F. Ackermann, L.P. Kubin, J. Lepinoux, H. Mughrabi, The dependence of dislocation microstructure on plastic strain amplitude in cyclically strained copper single crystals, Acta Metallurgica 32, 1984, pp. 715-725

[137] J. Polák, M. Klesnil, Cyclic stress-strain response and dislocation structures in polycrystalline copper, Materials Science and Engineering 63, 1984, pp. 189-196

[138] J. Polák, K. Obrtlík, J. Helešic, Cyclic strain localization in polycrystalline copper at room temperature and low temperatures, Materials Science and Engineering A 132, 1991, pp. 67-76

[139] V. Mazánová, M. Heczko, J. Polák, Fatigue crack initiation and growth in 43Fe-25Ni-22.5Cr austenitic steel at a temperature of 700 °C, International Journal of Fatigue 114, 2018, pp. 11-21

[140] J.H. Kim, B.K. Kim, D.I. Kim, P.P. Choi, D. Raabe, K.W. Yi, The role of grain boundaries in the initial oxidation behaviour of austenitic stainless steel containing alloyed Cu at 700 °C for advanced thermal power plant applications, Corrosion Science 96, 2015, pp. 52-66

[141] S.J. Rothman, L.J. Nowicki, G.E. Murch, Self-diffusion in austenitic Fe–Cr–Ni alloys Journal of Physics F: Metal Physics 10, 1980, pp. 383-398

[142] L. Intiso, L.G. Johansson, S. Canovic, S. Bellini, J.E. Svensson, M. Halvarsson, Oxidation behaviour of Sanicro 25 (42Fe22Cr25NiWCuNbN) in O2/H2O mixture at 600°C, Oxidation of Metals 77, 2012, pp. 209-235

[143] B.S.-J. Kang, P.L. Zhang, M. Ellathur, Chapter: Stress accelerated grain boundary oxygen embrittlement on creep crack growth of nickel-base superalloys, Book: Fatigue and fracture at elevated temperatures, American Society of Mechanical Engineers AD50, 1995, pp. 225-254.

[144] P. Wagenhuber, V.B. Trindade, U. Krupp, The role of oxygen-grain boundary diffusion during intercrystalline oxidation and intergranular fatigue crack propagation in Alloy718, in: Proc. Of 6th International Symposium on Superalloys 718, 625, 706 and Various Derivatives, 2005, pp. 591-600

[145] H.-J. Christ, K. Wackerman, U. Krupp, On the mechanism of dynamic embrittlement and its effect on fatigue crack propagation in IN718 at 650°C, Procedia Structural Integrity 2, 2016, pp. 557-564

[146] B. Fournier, M. Sauzay, C. Caes, M. Noblecourt, M. Mottot, A. Bougault, V. Rabeau, A. Pineau, Creep-fatigue-oxidation interactions in a 9Cr-1Mo martensitic steel. Part 1: effect of tensile holding period on fatigue lifetime, International Journal of Fatigue 30, 2008, pp. 649-662

[147] D. Argence, A. Pineau, Predictive metallurgy applied to creep-fatigue damage of austenitic stainless steels, in: Proc. Of the Donald McLean Symposium, Structural Materials, The Institute of Materials, 1995, pp. 229-257

[148] J. Wareing, Creep–fatigue behaviour of four casts of type 316 stainless steel, Fatigue & Fracture of Engineering Materials & Structures 4, 1981, pp. 131-145

[149] B. Michel, Formulation of a new intergranular creep damage model for austenitic stainless steel, Nuclear Engineering and Design 227, 2004, pp. 161-174

[150] V. Škorík, I. Šulák, K. Obrtlík, J. Polák, Thermo-mechanical and isothermal fatigue behavior of austenitic stainless steel AISI 316L, Metal Conference Proceedings 85, 2015

[151] S. Yamaura, Y. Igarashi, S. Tsurekawa, T. Watanabe, Structure-dependent intergranular oxidation in Ni-Fe polycrystalline alloy, Acta Materialia 47, 1998, pp. 1163-1174

[152] S. Guth, R. Petráš, V. Škorík, T. Kruml, J. Man, K. Lang K, J. Polák, Influence of dwell times on the thermomechanical fatigue behavior of a directionally solidified Ni-base superalloy, International Journal of Fatigue 80, 2015, pp. 426-433

[153] J. Man, K. Obrtlík, J. Polák, Study of surface relief evolution in fatigued 316L austenitic stainless steel by AFM, Materials Science and Engineering A351, 2003, pp. 123-132

[154] J. Man, P. Klapetek, O. Man, A. Weidner, K. Obrtlík, J. Polák, Extrusions and intrusions in fatigued metals. Part 2. AFM and EBSD study of the early growth of extrusions and intrusions in 316L steel fatigued at room temperature, Philosophical Magazine 89, 2009, pp. 1337-1372

[155] K. Obrtlík, J. Polák, A. Vašek, Short fatigue crack behaviour in 316L stainless steel, International Journal of Fatigue 19, 1997, pp. 471-475

[156] J. Polák, P. Zezulka, Short crack growth and fatigue life in austenitic-ferritic duplex stainless steel, Fatigue & Fracture of Engineering Materials & Structures 28, 2005, pp. 923-935

[157] V. Mazánová, J. Polák, Initiation and growth of short fatigue cracks in austenitic Sanicro 25 steel, Fatigue & Fracture of Engineering Materials & Structures 41, 2018, pp. 1529 - 1545

9. List of abbreviations and symbols

Abbreviations

A-USC - advanced-ultra supercritical

ASST - austenitic stainless steel

FCC - face-centred cubic

STEM - scanning transmission electron microscopy

SC - supercritical

USC - ultra-supercritical

SH - superheat

RH - reheat

PDF - probability density function

KWL - Kuhlmann-Wilsdorf and Laird

PSB - persistent slip band

PSM - persistent slip marking

SAGBO - stress assisted grain boundary oxidation

TEM - transmission electron microscopy

EGM - Essmann, Gösele and Mughrabi

SEM - scanning electron microscopy

FIB - focused ion beam

AFM - atomic force microscopy

LCF - low cycle fatigue

CF - creep-fatigue

TMF - thermomechanical fatigue

IP-TMF - in-phase thermomechanical fatigue

OP-TMF - out-of-phase thermomechanical fatigue

RT - room temperature

HT - high temperature

EDS - energy dispersive spectroscopy

IF - isothermal fatigue

IF-D - isothermal fatigue with dwell

IPD-TMF - in-phase thermomechanical fatigue with dwell

OPD-TMF - out-of-phase thermomechanical fatigue with dwell

EBSD - electron back scatter electron diffraction

Symbols

a, b, c - lattice parameters

σ_a - stress amplitude

ε_a - strain amplitude

ε_{ap} - plastic strain amplitude

ε_{ae} - elastic strain amplitude

ε'_f - fatigue ductility coefficient

c - fatigue ductility exponent

N - number of cycles

N_f - numbers of cycles to fracture

σ'_f - fatigue strength coefficient

b - fatigue strength exponent

E - Young's modulus

σ_{mT} - maximum stress in tension

σ_{mC} - maximum stress in compression

σ_{eT} - effective stress in tension

σ_{eC} - effective stress in compression

σ_{iT} - internal stress in tension

σ_{iC} - internal stress in compression

σ_{pC} - stress level at which plastic strain starts in tension

σ_{pT} - stress level at which plastic strain starts in compression

$f(\sigma_{ic})$ - probability density function, function of the internal critical stress

σ_i - internal stress component

σ_ε - effective stress component

σ_r - relative stress

ε_r - relative strain

E_{eff} - effective elastic modulus

σ_{es} - saturated effective stress

ρ_e - density of the edge dislocation

l - depth of PSB under the surface

w - width of the PSB

T - cycle period

D_v - vacancy diffusion coefficient

c_v - vacancy concentration

x - distance from the PSB centre

A - athermal annihilation coefficient

p - production rate of point defect

r_{Ec} - growth rate of the extrusion height

h_E - extrusion height

r_{lm} - growth rate of the intrusion depth

d_l - intrusion depth

d_c - parameter characterizing the delay between the extrusion formation and intrusion growth

b - Burgers vector

$R_{p0,2}$ - yield stress defined at engineering strain equal to 0.2%

R_m - tensile strength

$\dot{\varepsilon}$ - strain rate

$\varepsilon_r E_{eff}/2$ - fictive stress

10. Curriculum Vitae

Surname, first name:	Petráš, Roman
Contact address:	Makovického 32/74, 03601 Martin, Slovakia
Telephone:	+420 532 290 345
Mobil:	+420 774 629 732
Date of birth:	09/14/1988
Place of birth:	Martin, Slovakia
Marital status:	single
Email:	petras@ipm.cz

Academic Qualification

Masaryk University, Faculty of Science, Bachelor's degree programme, 2011 (completed)

Field of Study:	Physics
Thesis:	Pyrometric Measurements of Substrate Temperature during Plasmachemical Deposition
Supervisor:	doc. Mgr. Lenka Zajíčková, Ph.D.

Masaryk University, Faculty of Science, Master's degree programme, 2014 (completed)

Field of Study:	Plasma Physics
Thesis:	Fabrication of sensors based on carbon nanotubes
Supervisor:	doc. Mgr. Lenka Zajíčková, Ph.D.

Central European Institute of Technology BUT, Doctor's degree programme, 2014-2020

Field of Study:	Advanced materials
Thesis:	Fatigue resistance and mechanisms of the fatigue damage in materials for high temperatures
Institute:	Institute of Physics of Materials Academy of Sciences of the Czech Republic
Supervisor:	prof. RNDr. Jaroslav Polák, DrSc., dr. h. c

Work Experience

Institute of Physics of Materials of the Academy of Sciences of the Czech Republic, v. v. i.

Group:	Low Cycle Fatigue Group (2011-2014)
Position:	part-time job at the laboratory staff position
Group:	Brittle Fracture Group (2013-2014)
Position:	part-time job at the laboratory staff position
Group:	Low Cycle Fatigue Group (2014-presence)
Position:	PhD student - Advanced Metallic Materials and Metal Based Composites

Internship Experience

Internship in Leoben (Austria)

Institute:	The Erich Schmid Institute of Materials Science (ESI)
Supervisor:	Prof. Dr. Reinhard Pippan
Duration:	2 months (7.10.2015 – 4.12.2015)
Purpose:	The improvement of abilities in terms of the scanning electron microscopy.

Internship in Siegen (Germany)

Institute:	University of Siegen, Department of Mechanical Engineering
Supervisor:	Prof. Dr.-Ing. H-J. Christ
Duration:	3 months (5.3.2018 – 30.5.2018)
Purpose:	The effect of environment on the damage mechanism as well as mechanical response was addressed during the stay. LCF tests conducted in the vacuum chamber.

11. Publications

2018

- R. Petráš, J. Polák, Damage mechanism in austenitic steel during high temperature cyclic loading with dwells, International Journal of Fatigue 113, 2018, pp. 335-344
- J. Polák, V. Mazánová, R. Petráš, M. Heczko, Early damage and fatigue crack initiation at ambient and elevated temperatures in heat resistant austenitic steel, MATEC Web of Conferences 165, 2018, pgs. 6
- H. Wärner, M. Calmunger, G. Chai, J. Polák, R. Petráš, M. Heczko, T. Kruml, S. Johansson, J. Moverare, Fracture and damage behavior in an advanced heat resistant austenitic stainless steel during LCF, TMF and CF, Procedia Structural Integrity 13, 2018, pp. 843-848

2017

- J. Polák, V. Mazánová, M. Heczko, R. Petráš, I. Kuběna, L. Casalena, J. Man J, The role of extrusions and intrusions in fatigue crack initiation, Engineering Fracture Mechanics 185, 2017, pp.46-60

2016

- J. Polák, R. Petráš, V. Mazánová, Basic mechanisms leading to fatigue failure of structural materials, Transactions of the Indian Institute of Metals 69, 2016, pp. 289-294
- R. Petráš, V. Škorík, J.Polák, Thermomechanical fatigue and damage mechanisms in Sanicro 25 steel, Materials Science and Engineering A 650, 2016, pp. 52-62
- R. Petráš, V. Škorík, J. Polák, Damage evolution in thermomechanical loading of stainless steel, Procedia Structural Integrity 2, 2016, pp. 3407-3414
- J. Polák, R. Petráš, M. Heczko, T. Kruml, G. Chai G, Evolution of the cyclic plastic response of Sanicro 25 steel cycled at ambient and elevated temperatures, International Journal of Fatigue 83, 2016, pp. 75-83
- J. Polák, R. Petráš, G. Chai, V. Škorík, Surface profile evolution and fatigue crack initiation in Sanicro 25 steel at room temperature, Materials Science and Engineering A 658, 2016, pp. 221-228

2015

- J. Polák, R. Petráš, V. Mazánová, Basic mechanisms leading to fatigue failure of structural materials, Transactions of the Indian Institute of Metals 1, 2015, pp. 1-6
- S. Guth, R. Petráš, V. Škorík, T. Kruml, J. Man, K. Lang, J. Polák , Influence of dwell times on the thermomechanical fatigue behavior of a directionally solidified Ni-base superalloy, International Journal of Fatigue 80, 2015, pp. 426-433
- J. Polák, M. Petrenec, A. Chlupová, J. Tobiáš, R. Petráš, Cyclic plastic response of nickel-based superalloy at room and at elevated temperatures, Materials Testing 57, 2015, pp. 119-125

- J. Polák, R. Petráš, Hysteresis loop analysis in cyclically strained materials, Advanced Structured Materials 57, 2015, pp. 185-205

2014

- J. Polák, R. Petráš, M. Heczko, T. Kruml, G. Chai, Analysis of cyclic plastic response of heat resistant Sanicro 25 steel at ambient and elevated temperatures, Procedia Engineering 74, 2014, pp. 68-73
- M. Petrenec, J. Polák, J. Tobiáš, M. Šmíd, A. Chlupová, R. Petráš, Analysis of cyclic plastic response of nickel based IN738LC superalloy, International Journal of Fatigue 65, 2014, pp. 44-50
- J. Polák, R. Petráš, M. Heczko, I. Kuběna, T. Kruml, G. Chai G, Low cycle fatigue behavior of Sanicro 25 steel at room and at elevated temperature, Materials Science and Engineering A 615, 2014, pp. 175-182